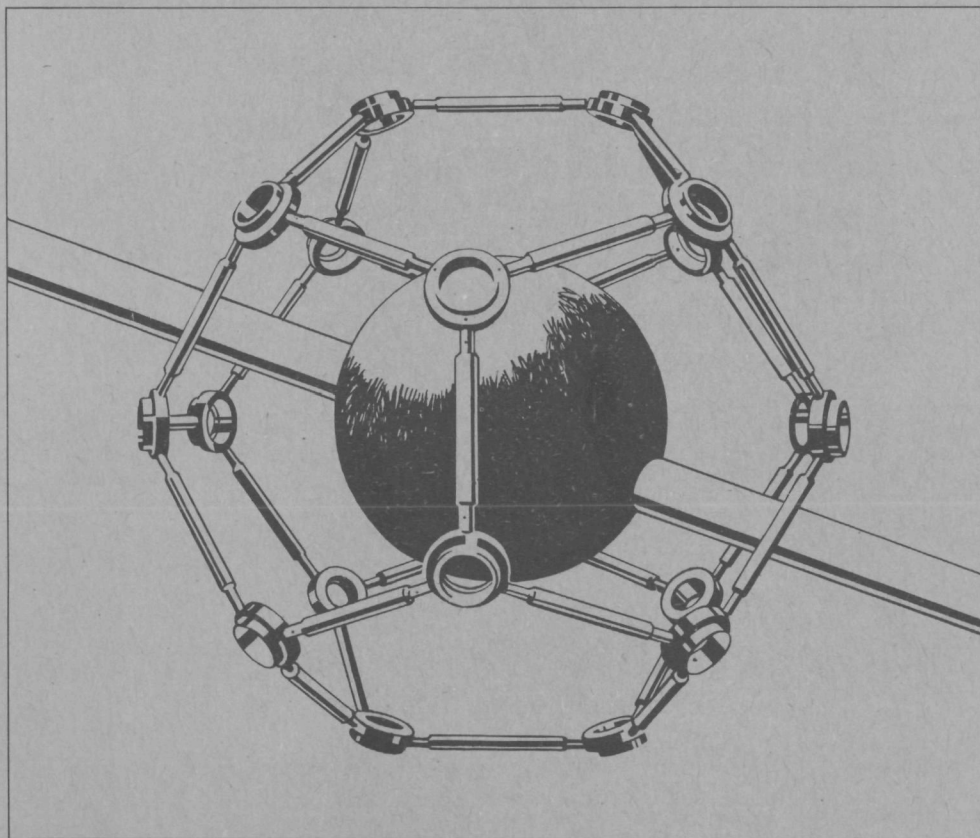


# The graphite ball detector

A new device for the measurement of the nuclear  
Doppler effect and integral neutron absorption  
cross - sections in intermediate and fast neutron spectra



P.W. Renaud

1026 2252

P1826  
2252



C10055  
98865

BIBLIOTHEEK TU Delft  
P 1826 2252



C

559886

erratum

p. 111 The first line has unfortunately been omitted. The first two lines should read :

individual neutron track from the target to the source is equal to the probability density of selecting the same neutron track from

# The graphite ball detector

A new device for the measurement of the nuclear  
Doppler effect and integral neutron absorption  
cross - sections in intermediate and fast neutron spectra

PROEFSCHRIFT

TER VERKRIJGING VAN DE GRAAD VAN DOCTOR IN DE TECHNISCHE  
WETENSCHAPPEN AAN DE TECHNISCHE HOGESCHOOL DELFT, OP GEZAG  
VAN DE RECTOR MAGNIFICUS DR. IR. H. VAN BEKKUM, HOGLERAAR  
IN DE AFDELING DER SCHEIKUNDIGE TECHNOLOGIE, VOOR EEN COM-  
MISSIE AANGEWEEZEN DOOR HET COLLEGE VAN DEKANEN TE VERDE-  
DIGEN OP WOENSDAG 1 OKTOBER 1975 TE 16.00 UUR

DOOR

1826 2252

PETER WILHELMUS RENAUD

NATUURKUNDIG INGENIEUR  
GEBOREN TE 's-GRAVENHAGE



© 1975 by P.W. Renaud, Eindhoven, Netherlands

DRUK WIBRO HELMOND

DIT PROEFSCHRIFT IS GOEDGEKEURD DOOR DE PROMOTOREN

DR. IR. H. VAN DAM en PROF. DR. J.J. WENT

de uitvoering van dit werk is mogelijk gemaakt door  
samenwerking tussen het Interuniversitair Reactor  
Instituut te Delft en de Technische Hogeschool Eindhoven

*aan hilda, christa en ons sjefke*

## CONTENTS

### 1. GENERAL INTRODUCTION

ΔΔ 1.1. Motivation and scope of the work	1
1.2. Outline of the following chapters	6

### 2. CHOICE AND DESIGN OF THE MEASURING SYSTEM

2.1. Choice of the system	
2.1.1. Introduction	7
2.1.2. Phenomena giving rise to measurements	7
ΔΔ 2.1.3. Principles of the graphite ball detector	9
2.2. Design of the dimensions of the detector and other system components	
2.2.1. The sample diameter	12
2.2.2. The graphite ball	14

### 3. THE PRACTICAL PERFORMANCE OF THE GRAPHITE BALL DETECTOR

ΔΔ 3.1. Introduction	21
3.2. Description of the experimental facilities and their main properties	23
3.3. Maximizing the signal to background ratio	
3.3.1. The neutron beam	
3.3.1.1. The neutron scatterer	28
3.3.1.2. The neutron beam profile	29
3.3.1.3. The neutron filters	30
3.3.2. Improvements of the detector	31
3.3.3. The background signal	31
3.4. The insensitive time of the detector	32
3.5. The position of the dodecahedron and the slowing down effect of neutrons in the target sample	

---

ΔΔ The marked sections can be used as a brief survey of the work

3.5.1. Introduction	34
3.5.2. The position of the dodecahedron	35
3.5.3. The scattered fraction	39
3.5.4. An experimental determination of the correction for the slowing down effect in the sample and for the position of the dodecahedron ( <i>mod.c12</i> ) by means of sample substitution	42
3.5.5. A mixed experimental and calculatory determination of <i>mod.c12</i>	44
3.6. The reference factor	
3.6.1. General	47
3.6.2. Measurement of the temperature dependent reference factor	49
3.7. Secondary neutron absorption	
3.7.1. General	53
3.7.2. Measurement of the secondary neutron absorption	53
3.8. The thermal expansion of the target sample	56
3.9. The sample temperature distribution and position	59
$\Delta\Delta$ 3.10. Review of the applied correction factors, definitions and relations	61
4. THE CALCULATION PROGRAMS	
$\Delta\Delta$ 4.1. Introduction	64
4.2. The detector efficiency	66
4.3. The neutron spectra	
4.3.1. Introduction	70
4.3.2. The neutron spectrum in the ATHENE 2-core system	72
4.3.3. MCREVERSE. A backward Monte Carlo program for the calculation of the filtered neutron beam spectra	73
4.4. MCTRANS. Calculations of the sample properties	75

5. EXPERIMENTAL RESULTS AND COMPARISON WITH CALCULATIONS

5.1. The neutron spectrum	78
ΔΔ 5.2. UO <sub>2</sub> and ThO <sub>2</sub> Doppler measurements	81
5.3. Error discussion	
5.3.1. Experimental uncertainties	91
5.3.2. Calculation errors	98
ΔΔ 5.3.3. Conclusions	101
APPENDIX (The backward Monte Carlo routine)	104
REFERENCES	124
LIST OF SYMBOLS	130
SUMMARY	134
SAMENVATTING	137
ACKNOWLEDGEMENTS	140

## 1. GENERAL INTRODUCTION

### 1.1. *Motivation and scope of the work*

Although many problems of the fast breeder reactor have to be solved yet, it is generally accepted that this type of reactor has the best possibilities for the future. The approx. 30 times more economical use the reactor makes of the natural uranium resources enables the poor ores and the uranium contents of the sea to be exploited at a price which would be unacceptable in the case of using these in the present thermal nuclear reactors. The economically applicable nuclear energy deposits may increase by a factor 1000 or more by the use of fast and thermal breeder reactors.

Among the problems of the fast breeder reactor the requirement of inherent safety of the nuclear system is probably the most obvious. Not only the fast breeder reactor but any nuclear reactor must have a negative temperature coefficient of reactivity.

In a thermal reactor the contribution to the negative temperature coefficient of the change of the moderator/fuel ratio and the neutron leakage due to the thermal expansion of the fuel elements is considerable, even at rather fast temperature changes. However, in a fast reactor, in view of the extremely short generation time ( $10^{-6}$  to  $10^{-7}$  s) between the fission events, the nuclear Doppler effect is the only physical phenomenon to furnish the necessarily prompt decrease in reactivity at a sudden temperature rise.

The nuclear Doppler effect is caused by the complicated resonance structure of the cross-sections of the heavy isotopes in the energy range of 1 eV to 50 keV (Fig. 1.1). An apparent change in the peaks of these cross-sections is induced by the change of the atom vibrations at a temperature change. The resulting change in selfshielding of the heavy materials causes a change in the reaction rates. A rising temperature causes an increase in the reaction rates of neutron capture and of scattering but also of fission of the fissile isotopes. The balance between the increase in neutron capture and neutron induced

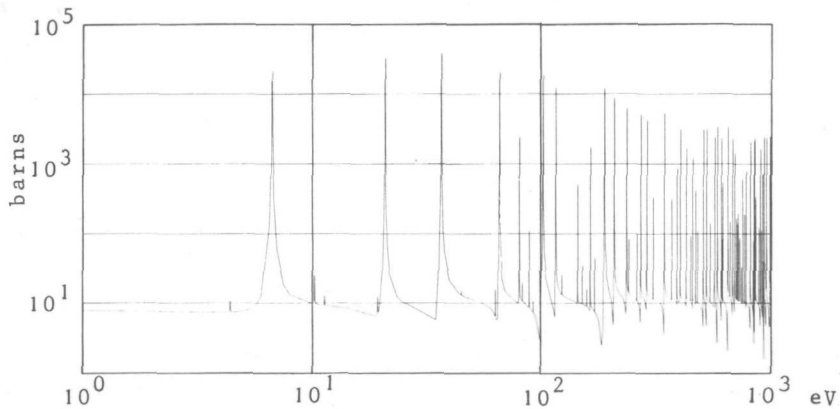


Fig. 1.1 Total cross-section of  $^{238}\text{U}$

fission at a temperature rise determines the prompt temperature behaviour of the fast reactor.

Considering the neutron spectra of some possible fast reactor types (Fig. 1.2) with different reactor coolant or core construction, it appears that the major differences are in the lower energy range ( $< 100 \text{ keV}$ ), which defines the Doppler effect. For the reasons mentioned above a detailed knowledge of the nuclear Doppler effect as a function of the neutron spectrum gradient in the various fissile and fertile materials will be of great advantage when designing an inherently safe reactor system.

Research institutions all over the world have paid attention to the study of the nuclear Doppler effect both in theory and by experiment (1,2,3,4,5,6,7,8,9,10). A common point in the main Doppler programs of the most prominent institutions is that practically all the observations have been made in low power critical assemblies by measuring the reactivity change resulting from the heating of a measurement sample. Intercomparison of the experimental results is often very difficult owing to variations in the neutron spectrum, the core construction and other experimental facilities. Therefore, it is necessary to compare the experimental results of each author with

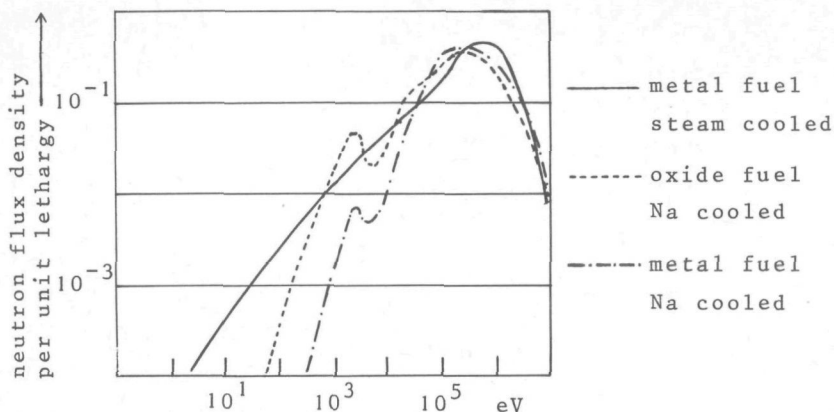


Fig. 1.2 Examples of fast reactor neutron spectra

his own calculations. The interpretation of the reactivity measurements is often very complicated. Probably the major difficulty in the theoretical treatment of such an experiment is (8) that the flux dips due to the resonances are different in the sample from those in the core, because their temperatures differ. At and near the boundary (very often the sample diameter is less than one mean free path, so that all of the sample volume is near the boundary) these fluxes overlap, and for the calculation of reaction rates in both regions one has to take account of this overlap.

Although this type of Doppler measurements is now looked upon as a standard technique and the uncertainties associated with its use are felt to be not different from those for other types of reactivity measurement (11), discrepancies of 10 to 50% between measurement and calculation are still quite normal (12,13,14,15,16,17).

For this reason it seems very useful to investigate other methods of Doppler measurement with perhaps a less sensitive detecting system, but with an easier interpretation.

A good second seems to be the Doppler activation measurement method used in thermal and fast reactor spectra. Sher (18,19), Pflasterer (19,20), Tirén (21), Davey (22), and others mentioned by Hellstrand (23) have performed activation Doppler measurements, comparing the activation of warm and cold irradiated foils of several materials.

Foell (24) utilizes a pulsed reactor to heat the enriched activation sample by fission. Measurements up to 2560 K have been performed (25). The inaccuracy of the activation method is reported to be less than 10% (26). Discrepancies between measurement and calculation of 10 to 100% are reported.

Only few investigators make mention of other Doppler measurement methods.

Seufert and Stegemann (27) make use of the "slowing down time spectrometer technique". Pulsed 14 MeV neutrons are produced in a block of lead. The comparatively well-known relation between slowing down time and mean neutron energy in the block of lead makes it possible to measure the hot-to-cold neutron capture ratio of a sample, positioned in the block of lead, as a function of the neutron energy ( $< 30$  keV). Thin samples of various materials were heated and the capture  $\gamma$ -rays were detected by proportional counters. The advantage of the method is the energy dependence of the information. The accuracy of the method is rather poor.

Beller and Heneveld (28) are using essentially the reactivity method. However, by cycling the sample temperature, the temperature derivative of the resonance integral is measured directly. The precision of the method is comparable to that obtained by standard reactivity methods.

Schoenig (29) determines separately the numbers of neutron induced captures and fissions in  $^{235}\text{UO}_2$  samples, using mass spectrometry for the  $^{236}\text{U}$  contents and  $\gamma$ -ray spectrometry for the  $^{235}\text{U}$  fission products.

Banharnsupavat (30) mentions a new technique, comprising the use of a piezo-electric transducer coupled to a target foil to induce motion in the target atoms.

Dekker (31,32) measures the direct flux depression with an annular ionisation chamber around the heated sample in a  $\frac{1}{E}$  flux. Using a dynamic oscillation technique, the measurement uncertainty is 10 to 20%. The discrepancy between calculation and measurement is within the error margin, as has also been found by other investigators in a  $\frac{1}{E}$  flux. Making a conclusion about the state of affairs at the moment, it may be said that the reactivity method is the most sensitive.

Very complicated problems about the interpretation of the reactivity

signal reduce the reliability of the comparison between measurement and calculation. Other methods are less sensitive, but the easier interpretation of the observations often makes possible a better comparison with calculation results. The discrepancy between Doppler measurement and calculation of the most important isotope,  $^{238}\text{U}$ , in the case of a  $\frac{1}{E}$  spectrum, is within experimental error. In the case of fast neutron spectra most discrepancies reported are in the range of 10 to 50%. In the case of other isotopes such as  $^{239}\text{Pu}$ , larger discrepancies are no exception.

This work presents the design and the practical testing of a comparatively cheap measuring system for the nuclear Doppler effect in an easily variable neutron spectrum. Samples of any kind of material can be measured and even a very simple thermal nuclear reactor with irradiation facilities will be a good neutron source, the gradient of the spectrum of which can be adapted by filtering techniques. Without experiments to confirm this, it may be stated, however, that the system can also be applied when a fast reactor system or other powerful neutron source (e.g. a strong Am-Be source) is used.

When starting the design, the two points of departure were:

- The system has to be cheap and flexible.
- Only simple geometries and neutron-physically well-known materials are to be applied to make the qualitative and quantitative calculations of the system sufficiently reliable even without very precise verifying measurements.

The system was tested by measuring a series of natural  $\text{UO}_2$  samples and a smaller series of  $\text{ThO}_2$  samples at temperatures of up to 1400 K. Three different neutron spectra were used: a pure thermal reactor spectrum, a moderately fast spectrum, and a fast spectrum resembling that of a steam-cooled fast reactor.

In addition to the results in the thermal spectrum, those in the faster spectra have also been compared with their corresponding calculations.

This Doppler measurement method, which can also be used for integral neutron absorption cross-section measurements, is presented because of the great importance of the nuclear Doppler effect and it is meant to contribute to a greater trust in the cross-sections to be used in reactor design.

### *1.2. Outline of the following chapters*

Chapter 2 gives the motivation of the choice of the method in comparison with other possibilities and the determination of the dimensions of the detector system. Section 2.1.3. describes the principles of the chosen system.

Chapter 3 fills up the gap between theory and practice. Besides a description of the experimental equipment, all troubling qualities and adventitious properties of the system pass in review.

Chapter 4 contains the models of the computer codes applied and gives the results of the calculations of the detector efficiency and the neutron spectra needed for the calculations and measurements of chapter 5. Chapter 5 compares the measurements and the calculations of the detector integrals of a series of natural  $\text{UO}_2$  samples and  $\text{ThO}_2$  samples. Some conclusions are made.

## 2. CHOICE AND DESIGN OF THE MEASURING SYSTEM

### 2.1. *Choice of the system*

#### 2.1.1. *Introduction*

The chief fissile and fertile reactor materials to be considered in studying the nuclear Doppler effect are  $^{232}\text{Th}$ ,  $^{233}\text{U}$ ,  $^{234}\text{U}$ ,  $^{235}\text{U}$ ,  $^{238}\text{U}$ ,  $^{239}\text{Pu}$  and the heavier Pu-isotopes. With  $^{232}\text{Th}$ ,  $^{234}\text{U}$  and  $^{238}\text{U}$  only resonance capture of the neutrons is important. With  $^{233}\text{U}$ ,  $^{235}\text{U}$  and  $^{239}\text{Pu}$  resonance fission is also a phenomenon of interest. The influence of resonance scattering upon the reactivity of the reactor core is negligible and will not be studied in this work. The possible phenomena to be measured are quite different in the case of resonance capture and resonance fission. Because of the important part played by the fertile materials  $^{232}\text{Th}$  and  $^{238}\text{U}$ , attention has been focussed on the measurable phenomena of resonance capture.

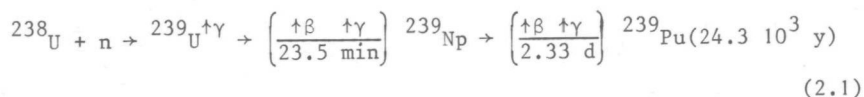
As already stated in the general introduction of chapter 1, there were two points of departure when choosing and starting the design of the system, which are repeated here for convenience :

- The system has to be cheap and flexible.
- Only simple geometries and neutron-physically well-known materials are to be applied to make the quantitative and qualitative calculations of the system sufficiently reliable, even without very precise verifying measurements.

For a clear insight into the possibilities of a Doppler measurement method, the measurable phenomena are presented in the following section (33).

#### 2.1.2. *Phenomena giving rise to measurements*

The neutron capture reaction in  $^{238}\text{U}$  may serve as an example to enable a list of the measurable phenomena to be offered.



The reasonably measurable phenomena are

- (a) the decrease in the neutron flux by the neutron capture reaction;
- (b) the prompt  $\gamma$ -ray associated with the neutron capture reaction;
- (c) the delayed  $\beta$  or  $\gamma$ -radiation of the daughter products;
- (d) the growth of the Pu content of the sample.

(a) The decrease in the neutron flux in consequence of the neutron capture reactions in a  ${}^{238}\text{U}$  sample can be measured in different ways:

- Direct measurement of the changes in the neutron flux.

This method was adopted for the present work because possibilities of this direct flux depression measurement seem reasonable. Thus far only Dekker (31,32) has used it.

- Indirect measurement of the changes in the neutron flux.

The reactivity method relies on it. Not being consistent with the second point of departure, it will not be discussed here.

(b) The neutron capture reaction in a  ${}^{238}\text{U}$  nucleus causes the binding energy of the neutron to be released by emission of one or more  $\gamma$ -rays with a joint energy of about 8 MeV. The greatest problem in measuring the phenomenon lies in separating these  $\gamma$ -rays from background  $\gamma$  radiation. A pulsed neutron source and a time-of-flight system are indispensable. Only Seufert (27) utilized the phenomenon. The accuracy of the measurements was rather poor.

(c) The  ${}^{239}\text{Np}$  contents of an irradiated sample can be measured by its delayed  $\beta$  or  $\gamma$  radiation. Because of the space dependence of the Np concentration and the strong self-shielding properties of the heavy materials, particularly for the  $\beta$  radiation, only very thin slices or foils of the irradiated sample may be examined, unless the whole sample is dissolved. A contingent difficulty is the activity of the  ${}^{238}\text{U}$  fission products. When irradiated in a reactor core, the problems of resonance overlap are essentially the same as in the case of the reactivity method. Several investigators have (18 to 24) used the system. Accuracy is reasonable within certain

limits. The half life of  $^{239}\text{Pu}$  is  $24.3 \cdot 10^3$  y. So it may be considered a stable isotope in this kind of experiment. The  $^{239}\text{Pu}$  contents of an irradiated sample can be examined by chemical analysis or, better still, by mass spectrography. Both methods have the disadvantage of the necessarily intensive irradiation of the sample to generate a measurable Pu concentration. Nevertheless Schoenig (29) reports the use of mass spectrography to measure  $^{236}\text{U}$  contents in a  $^{235}\text{UO}_2$  sample.

### 2.1.3. Principles of the graphite ball detector

As stated in sec. 2.1.2., the principle of the graphite ball detector is based on measurement of the absorption rate by the direct change of the neutron flux caused by the sample.

The idea is to measure the transmission of neutrons through a target sample. Comparison of the absorption rates of a target sample at various temperatures gives the required information about the nuclear Doppler effect in the sample.

To avoid the influence of scattered neutrons and of changes in the scattering properties of the sample, a  $4\pi$  neutron detection system around the sample may be constructed, the so called graphite ball detector. Using  $\text{BF}_3$  tubes, the detection efficiency of the neutrons of the fast spectrum will be very poor and a shell of moderating material between the sample and the detectors will be of advantage to the detection efficiency. To combine a minimum direction dependence in the detection efficiency of a limited number of detector tubes and a maximum signal to background ratio (see sec. 2.2.2.), a hollow graphite ball appears to be the best solution.

For a description of the detecting system, see Fig. 2.1.

A beam of neutrons with a proper energy spectrum hits the target sample  $S_1$  at the centre of the graphite ball. To minimize the influence of fluctuations in the neutron source and other physical circumstances, the sample  $S_1$  is periodically compared with the reference sample  $S_2$ . Coming from the sample, the neutrons are slowed down and dispersed by

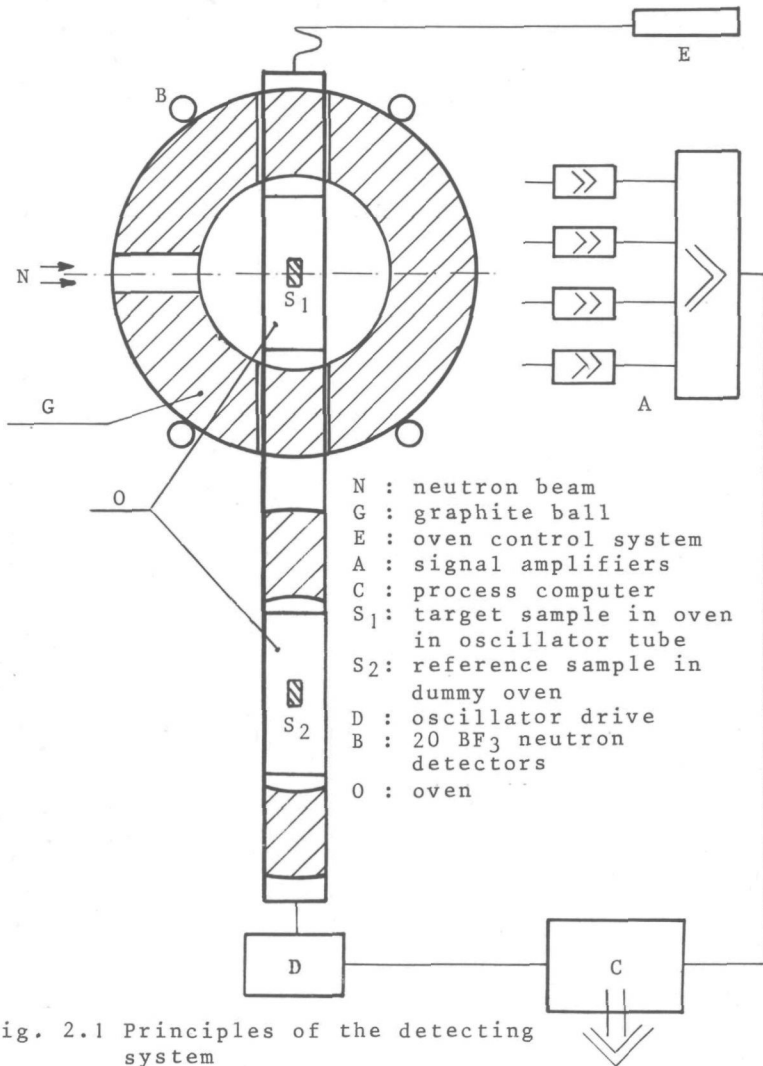


Fig. 2.1 Principles of the detecting system

the graphite ball before causing a signal in the twenty BF<sub>3</sub> neutron detectors. The amplified signal of the BF<sub>3</sub> tubes is analysed and recorded by the process computer, which produces the data for comparing the accumulated results of S<sub>1</sub> and S<sub>2</sub>, and controls the pneumatic oscillator drive. If either the oven temperature or the sample changes, the reaction rates in the sample and hence the signal of the BF<sub>3</sub> detectors, also change. Because of the wavy character of the efficiency

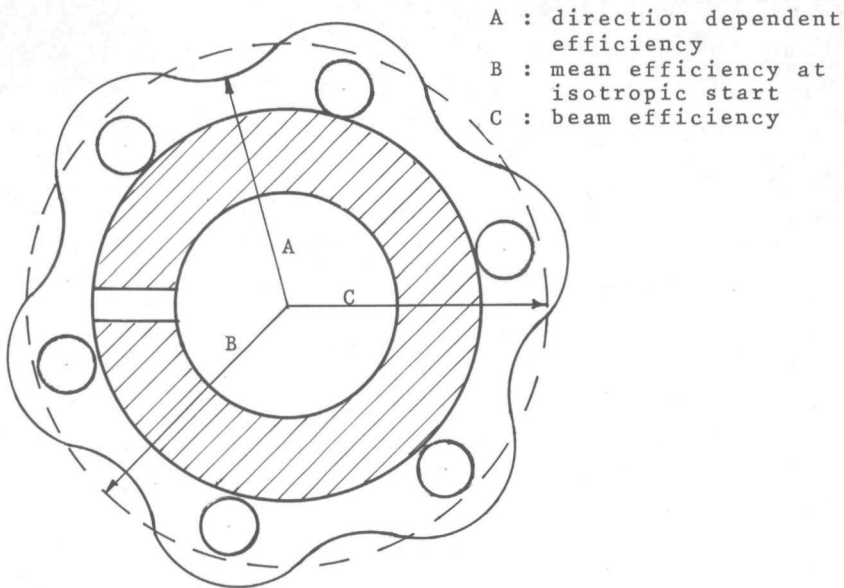


Fig. 2.2 Schematic detecting efficiency diagram of the graphite ball detector

diagram (Fig. 2.2) the twenty  $\text{BF}_3$  tubes are mounted at the twenty angular points of a regular dodecahedron. The latter is so positioned with respect to the neutron beam that the neutrons scattered by the target sample are detected with an efficiency equal to that of the neutrons passing through it in the beam direction without any interaction.

To understand the way of choosing the right position of the  $\text{BF}_3$  detectors, see Fig. 2.2. In this efficiency diagram the relative detection efficiency of the neutrons coming from the centre of the ball is represented by the distance from the centre of the ball as a function of the direction of departure of the neutrons. Presuming that the scattering of neutrons in the sample is isotropic, it is easily seen that the right position of the tubes is found when the efficiency of the neutrons in the beam direction is equal to the overall mean efficiency of the neutrons scattered isotropically from the centre of the ball.

Now changing the direction of the neutrons in the sample does not change their mean detection efficiency. So changes in the scattering properties of the sample do not affect the detector signal. Only changes in the number of neutrons leaving the sample do change the signal.

## 2.2. Design of the dimensions of the detector and other system components

### 2.2.1. The sample diameter

Before being able to determine the detector dimensions some of the boundary conditions of the experiment have to be considered. It appears that a criterion of the diameter of the disk-shaped target samples can be found from the boundary conditions. Starting from the sample diameter, the inner radius of the ball can be chosen and finally the outer radius of the ball can be determined.

The relevant conditions are given below:

- (a) The neutron source in the experiment is the thermal ATHENE reactor of the Eindhoven University of Technology. See Fig. 2.3. The

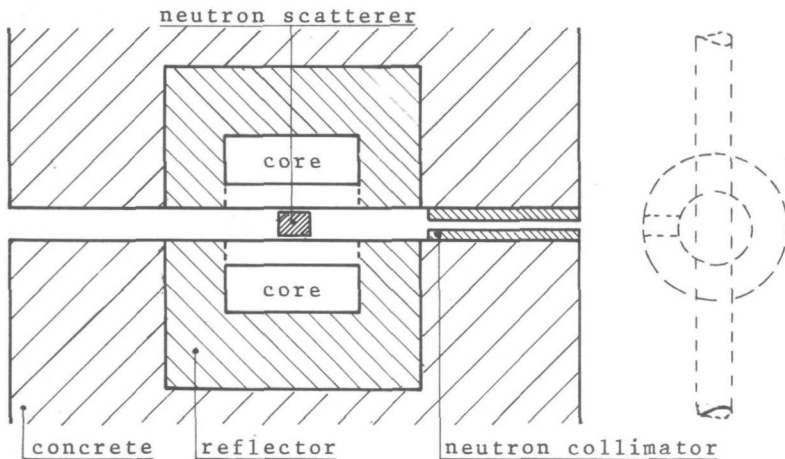


Fig.2.3 Configuration of the ATHENE reactor (top view)

neutrons are generated in the two core boxes containing water and fuel elements. A neutron scatterer of lead is mounted in an empty space between the two core boxes. The maximum integrated neutron flux density at the Pb scatterer is about  $2.10^{11}$  n/cm<sup>2</sup>s.

- (b) Knowing the thickness of the concrete shield of the reactor and keeping the boron carbide of the neutron collimator far enough away from the reactor core for criticality reasons, a reasonable length of the neutron collimator is 170 cm. The opening of the collimator is positioned at 60 cm from the centre of the reactor core.
- (c) To keep the background-to-signal ratio as low as possible, the diameter of the target sample has to be greater than that of the neutron beam where this hits the sample.
- (d) The changes in the detector signal induced by the nuclear Doppler effect may be expected to lie in the range of 0 to 1%. To prevent unacceptable measuring times, the counting rate of the measurements should be of the order of thousands per second.

From *a* and *b* it follows that the neutron flux density at the end of the collimator tube  $\phi_{coll}$  can be expected to be:

$$\phi_{coll} \approx 3.10^5 \text{ n/cm}^2\text{s}$$

The maximum acceptable counting rate of the detector, allowing for an insensitive time of more than 30  $\mu$ s per pulse, is of the order of 5000 c/s (see sec. 3.4.). To achieve this counting rate at a mean detector efficiency (i.e. counts per neutron entering the detector) of about 0.5 % (see Fig. 2.6), the diameter of the collimator opening should be about 2 cm.

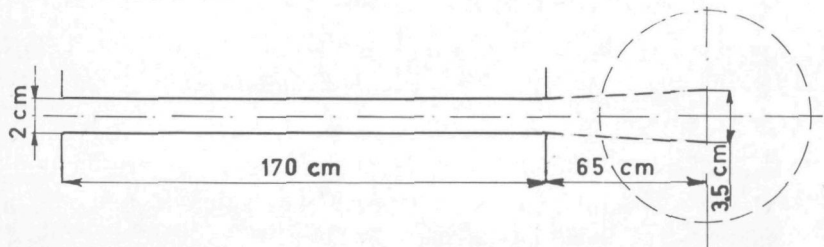


Fig. 2.4 The dimensions of the neutron beam  
(not to scale)

Starting from a collimator opening of 2 cm and a distance of 65 cm between the collimator opening and the centre of the graphite ball, it easily follows that the diameter of the neutron beam at the centre of the ball is about 3.5 cm. See Fig. 2.4. To satisfy  $c$  and to have some play to frame the sample in the oven, a suitable sample diameter is 4 cm.

### 2.2.2. *The graphite ball*

Starting from the 4-cm sample diameter, the material and the dimensions of the neutron moderating shell between the sample and the  $\text{BF}_3$  detectors can be determined.

The demands to be made on the shell are the following:

- (a) Without having the disposal of a set of well-known mono-energetic neutron sources, it is very difficult to measure the energy-dependent detector efficiency with any degree of precision. Therefore, the material of the shell should have neutron-physically well-known properties in order that the results of the calculations of the detector efficiency as a function of neutron energy, may be relied upon.
- (b) To keep small the influence of deviations from the correct position of the  $\text{BF}_3$  tubes with regard to the direction of the neutron beam, the amplitude of the efficiency wave in the efficiency diagram (see Fig. 2.2) should be as small as possible.
- (c) The slowing down of the neutrons has to be such that the uncertainty of the absorption measurement is minimal.
- (d) The outer dimensions of the ball should be as small as possible to combine maximum efficiency with a minimum number of  $\text{BF}_3$  detectors.
- (e) The inner diameter of the shell should be as large as possible to keep small the influence of secondary absorption of neutrons reentering the sample from the shell.

In order to provide for enough space for housing the oven and the oscillator tube, given the sample diameter of 4 cm, the inner diameter of the shell was established at 20 cm. The probability that secondary neutrons isotropically starting from the inner wall of the shell will hit the sample is now as small as 1%.

*N.B.* The influence upon the absorption signal of the secondary neutron absorption, however, can be considerably greater than 1% owing to the slowing down of fast neutrons and the long residence time of thermalized neutrons in the ball. See sec. 3.7.

When choosing the material for the shell, the demands  $a$ ,  $c$  and  $d$  have led to calculations for polyethylene, deuteriumoxide and graphite. In Table 2.1 are compared the efficiency waves concerning the three materials when 12 and 20  $\text{BF}_3$  detectors, respectively, are used around the ball. The ratio min/max indicates the quotient of the minimum and maximum of the detector efficiency at one configuration and can be used as a measure of the amplitude of the efficiency wave. The inner radius of the ball has been fixed at 10 cm, while the outer radii of the ball were so chosen as to satisfy demand  $c$  reasonably well.

Because of the great difference of the efficiency waves in the case of graphite on the one hand and  $\text{D}_2\text{O}$  and  $\text{CH}_2$  on the other, the combination of graphite and 20  $\text{BF}_3$  detectors seemed the best choice.

Table 2.1  
Comparison of the efficiency waves of the ball detector consisting of different slowing down materials

mat.	$r_i$ cm	$r_o$ cm	min/max	
			12 det.	20 det.
C	10	23	0.82	0.88
$\text{D}_2\text{O}$	10	14 <sup>†</sup>	0.23	0.33
$\text{CH}_2$	10	11	0.26	0.37

<sup>†</sup>It is to be noticed that in the case of  $\text{D}_2\text{O}$  the outer radius should have been 17 cm for the sake of the comparison. This, however, would not have affected the conclusion.

With graphite as slowing down material, the inner radius of the ball  $r_i = 10$  cm, and demand  $c$ , the outer radius  $r_o$  of the ball can now be determined.

Let the signal of the ball detector in the presence of the non-absorbing reference sample  $S_2$  (see Fig. 2.1) be  $R$ , and in the presence of the unknown sample  $S_1$  be  $W$ . Now  $R - W$  is a measure of the neutron absorption in sample  $S_1$ . Let  $f(R-W)$  be the standard deviation of  $(R-W)$ . Demand  $c$  can now be written as:

$$\frac{d}{dr_o} \left( \frac{f(R-W)}{R-W} \right) = 0 \quad (2.2)$$

When measuring, an estimate of the standard deviation of  $R$  and  $W$  can be made by taking the square root of the total number of counted detector pulses:  $\sqrt{R}$  and  $\sqrt{W}$  respectively, (34). And for  $f(R-W)$  can be written:

$$\frac{f(R-W)}{R-W} = \frac{\sqrt{(R+W)}}{R-W} \quad (2.3)$$

With

$$abs = \frac{R-W}{R} \quad (2.4)$$

follows

$$\frac{f(R-W)}{R-W} = \frac{1}{abs} \sqrt{\frac{2-abs}{R}} \quad (2.5)$$

With the boundary condition of sec. 2.2.1. of a fixed, maximum supply of neutrons  $\Phi(E)$ , limited by the maximum permissible power of the ATHENE reactor,  $R$  and  $W$  can be written as:

$$R = \int \Phi(E) \cdot B(E) \cdot eff(r_o, E) dE \quad (2.6)$$

and

$$W = \int \Phi(E) \cdot B(E) \cdot (1-abs(E)) \cdot eff(r_o, E) dE \quad (2.7)$$

$B(E)$  is the energy-dependent transmission function of the neutron filter between the reactor core and the collimator opening used to shape the neutron spectrum;

$eff(r_o, E)$  is the energy-dependent detector efficiency for an outer radius  $r_o$  of the ball;

$abs(E)$  is the energy-dependent neutron absorption in sample  $S_1$ .

With (2.4) follows:

$$abs = \frac{\int \Phi(E) \cdot B(E) \cdot abs(E) \cdot eff(r_o, E) dE}{\int \Phi(E) \cdot B(E) \cdot eff(r_o, E) dE} \quad (2.8)$$

The expressions (2.6) and (2.8) for  $R$  and  $abs$  cannot easily be solved analytically. For this reason a 26-group approach of the integrals has been made.

The neutron spectrum  $\Phi(E)$  in the centre of the reactor core has been calculated with the computer code FAST ZOOM DELFT (see sec. 4.3.2.). Knowing  $\Phi(E)$ , the transmission spectra  $\Phi(E) \cdot B(E)$  of the three neutron filters used in the measurements of chapter 5 have been calculated by the computer code MCREVERSE (see sec. 4.3.3.). The efficiency of the ball detector at five different values of  $r_o$  has been calculated using the computer codes MCLAAG, TREFKANS and MCBUIS (see sec. 4.2.). In Fig. 2.5 and Fig. 2.6 smooth curves have been drawn through the 26 calculated points of the neutron spectra and the detector efficiencies, respectively.

Finally, knowing the neutron spectra and the detector efficiencies,  $R$  and  $abs$  of formulae (2.6) and (2.8) have been calculated using the computer code MCTRANS (see sec. 4.4.), and the associated values of  $\frac{f(R-W)}{R-W}$  have been determined for a 5-mm  $UO_2$  sample. The results of the calculations are listed in Table 2.2.

It appears from this table that the minimum uncertainty in the measurements can be expected at  $r_o = 21$  cm for each of the neutron spectra. With samples of other thicknesses the optimum of the outer radius of the ball  $r_o$  also turns out to be 21 cm.

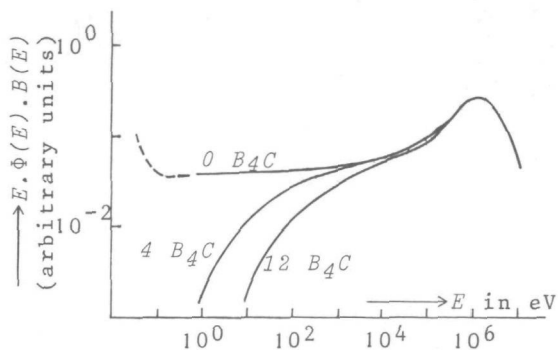


Fig. 2.5 The neutron spectra behind the filters

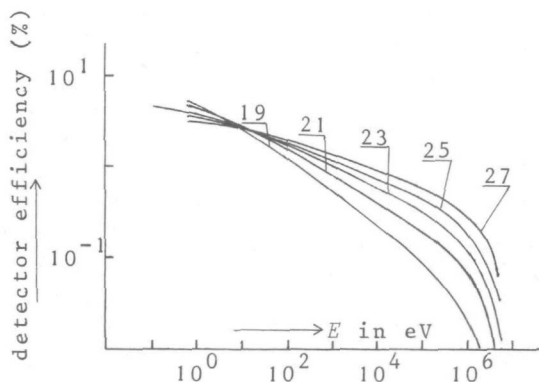


Fig. 2.6 Detector efficiency for various outer radii (cm) of the graphite ball

As discussed in sec. 3.5.2., the influence of the beam and of the oscillator passages through the graphite shell is considerably stronger upon fast-neutron than slow-neutron detection efficiency. As the detector efficiency calculations have not been corrected for the influence of the passages, the absolute values of the gradient of the curves of Fig. 2.6 are consequently somewhat too small.

Table 2.2

A comparison of the expected uncertainties in the measurements at various outer radii of the graphite ball

$r_o$ cm	<i>abs</i>	$R$ counts/s	$\frac{f(R-W)}{R-W}$
19	0.0454	4416	0.0463
21	0.0425	5436	0.0446
23	0.0385	6358	0.0456
25	0.0352	7147	0.0470
27	0.0315	8045	0.0496

(a) filter 0  $B_4C$

$r_o$ cm	<i>abs</i>	$R$ counts/s	$\frac{f(R-W)}{R-W}$
19	0.0441	2370	0.0651
21	0.0376	3340	0.0644
23	0.0314	4350	0.0676
25	0.0272	5310	0.0708
27	0.0233	6360	0.0756

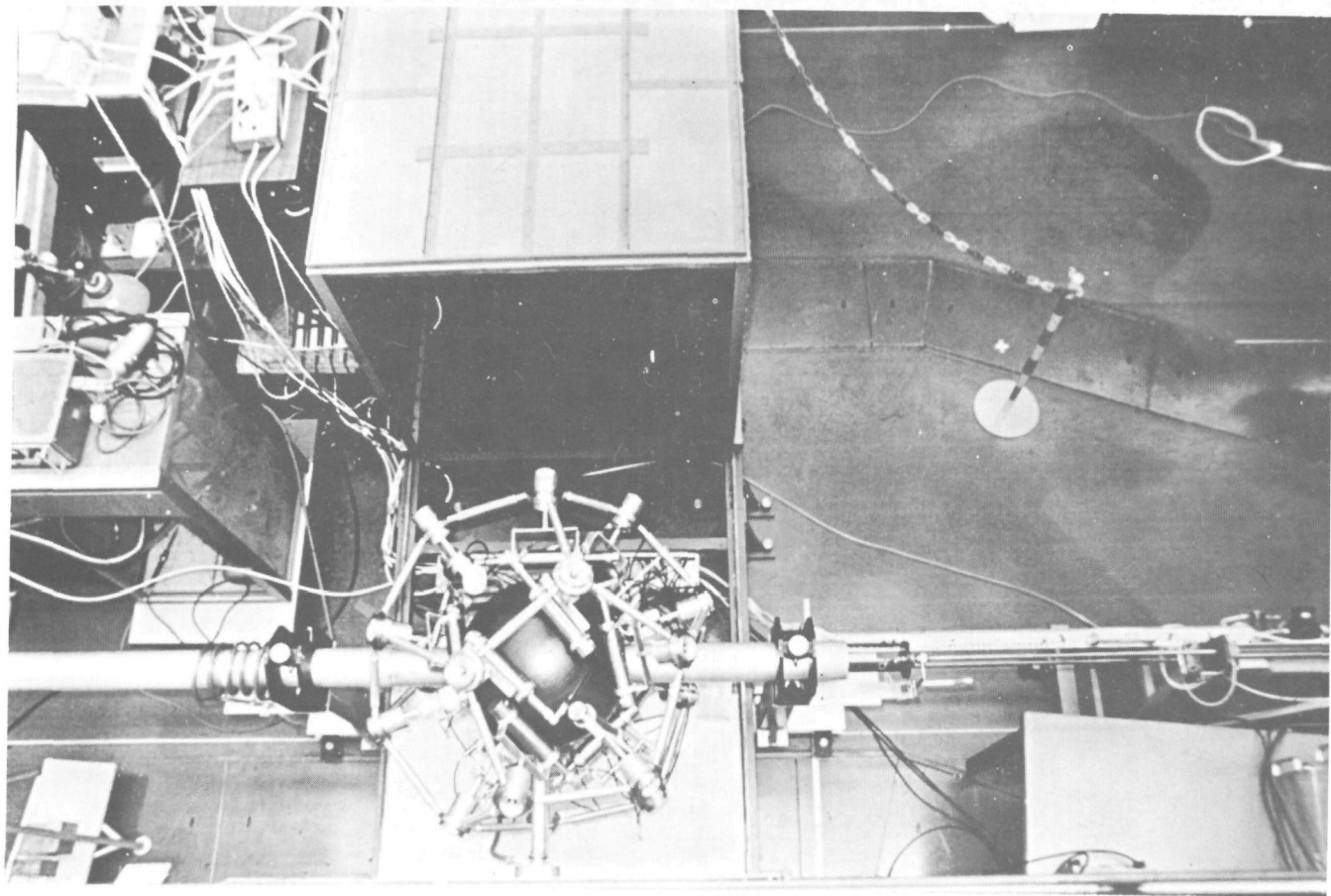
(b) filter 4  $B_4C$

$r_o$ cm	<i>abs</i>	$R$ counts/s	$\frac{f(R-W)}{R-W}$
19	0.0256	1280	0.154
21	0.0206	2080	0.150
23	0.0163	3030	0.156
25	0.0139	3970	0.161
27	0.0117	5060	0.170

(c) filter 12  $B_4C$

The outer radius of the ball has been fixed at 23 cm, which seems to be a fair choice.

*N.B.* If the reactor power is not given as a boundary condition, the counting rate in each measurement should be raised to the highest level that is permissible from the electronic standpoint. When optimizing  $r_o$ , the value of  $R$  can now be kept constant. The optimum value of  $r_o$  will be smaller in this case.



Top view of the graphite ball detector

### 3. THE PRACTICAL PERFORMANCE OF THE GRAPHITE BALL DETECTOR

#### 3.1. *Introduction*

Between the principles of the design and the effectuation of the measuring system there is the difference of practice.

To be able to produce reliable measurements, numerous problems had to be solved and various components had to be optimized.

Especially the required accuracy of the measurements makes it inevitable to study even the rather small disturbing effects. This chapter gives a review of the practical problems of the graphite ball detector.

The corrections to be applied can be divided into a temperature independent group and a temperature dependent group.

The temperature independent corrections are : the background signal (sec. 3.3.), the insensitive time of the electronic equipment (sec. 3.4.), the slowing down of the neutrons in the sample in combination with the deviation from the correct position of the dodecahedron with the  $\text{BF}_3$  tubes (sec. 3.5.).

The temperature dependent corrections are: the reference factor (sec. 3.6.), the secondary neutron absorption (sec. 3.7.), and the thermal expansion of the sample (sec. 3.8.).

It is evident that to determine the temperature induced nuclear Doppler effect, the temperature dependent group of corrections is essential. To determine the resonance integral of the samples with the different neutron spectra, however, the temperature independent corrections are likewise indispensable.

The chapter starts with a review of the equipment used in the experiments.

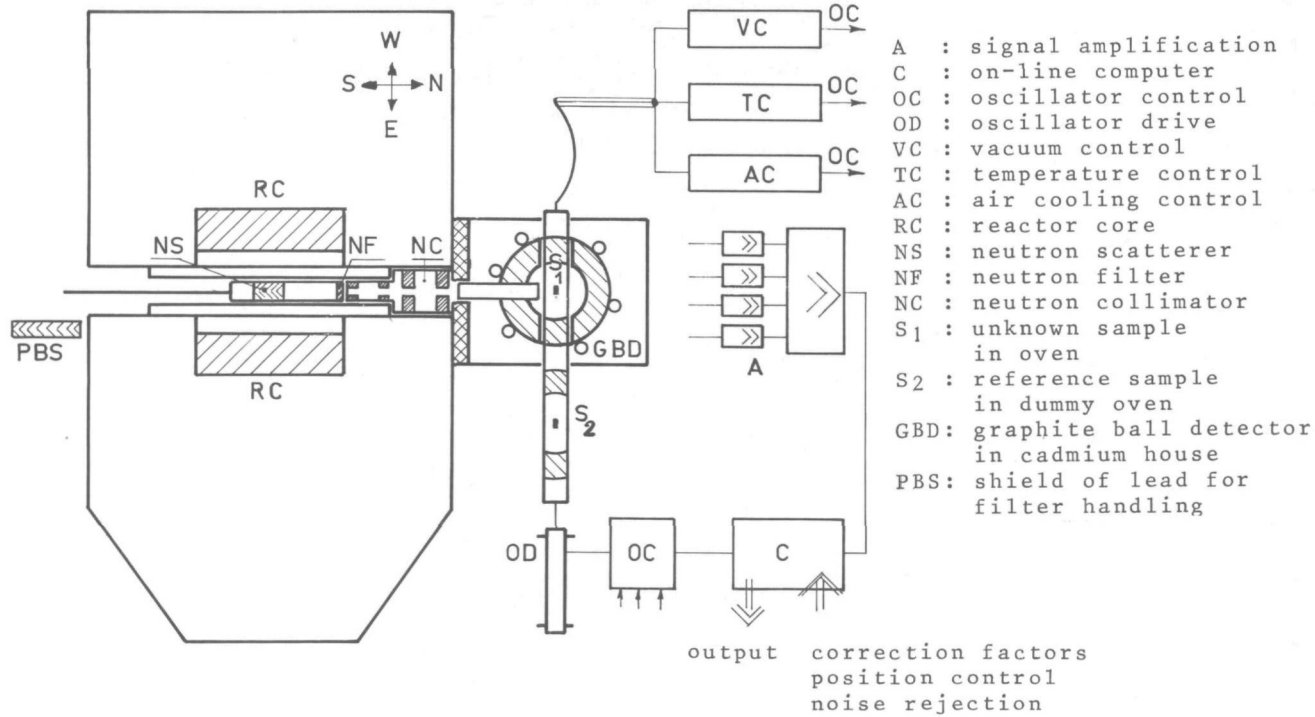


Fig. 3.1 Schematic top view of the experimental facilities

### 3.2. Description of the experimental facilities and their main properties

Fig. 3.1 is a schematic view of the experimental facilities. In the following the main components are described and briefly discussed.

Optimizing the position of the neutron scatterer of lead, fixes at the same time the distance between the scatterer and the neutron filter in front of the collimator opening. The Pb scatterer is held in a tubular holder part of which has been removed to receive the neutron filter (see Fig. 3.2). The holder can be pulled out of the reactor core at the south side to change the neutron filter, which operation takes only a few seconds.

To generate a well-defined neutron beam, a neutron collimator has been designed with several annular disks of boron carbide and conical cylinders of polyethylene between the disks (see Fig. 3.3). It has been so constructed that from the detector side of the collimator only the boron carbide disks and the Pb scatterer in the centre of the reactor can be seen.

The graphite ball is positioned in front of the collimator opening. To give the neutron beam access to the ball there is a cylindrical beam hole in the graphite shell. See Fig. 3.4. An aluminium vacuum tube to reduce the background neutron scattering by the air is mounted in the beam hole. At the back of the graphite shell another

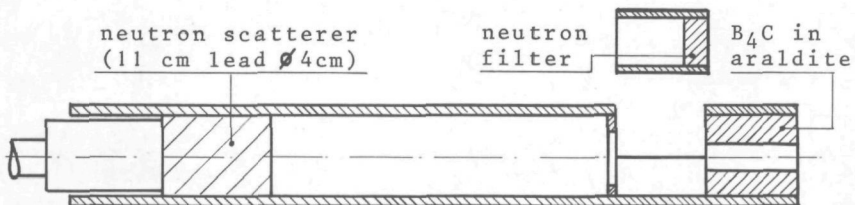


Fig. 3.2 Holder with neutron scatterer and neutron filter (not to scale)

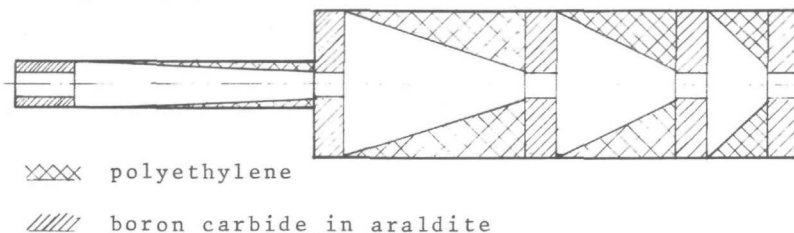


Fig. 3.3 The neutron collimator (not to scale)

opening has been provided to make possible the measurement of only the neutrons scattered in the sample (See also sec. 3.5.).

Neutrons not having interacted with the target sample just leave the ball. A graphite cylinder can be put into the hole at the back. On one end of the graphite cylinder a bismuth cylinder has been provided to reduce the influence of the deviation from the correct position of the  $\text{BF}_3$  tubes (Henceforth the Bi and C cylinders together will be referred to as the *Bi-C* scatterer). Some relevant properties of the graphite have been measured:

density :  $1.813 \text{ g/cm}^3 \pm < 0.5\%$

water content and volatile impurities :  $< 400 \text{ ppm}$  by weight  
 (normal hydrogen content of nuclear graphites is about  $300 \text{ ppm}$  by weight (35))

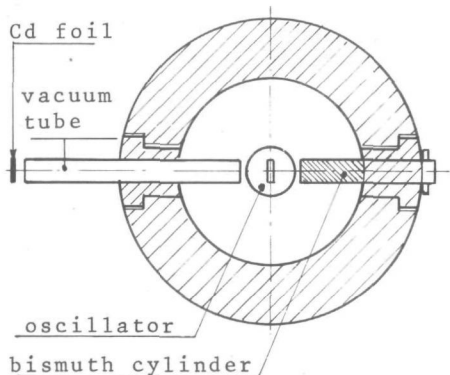


Fig. 3.4 The graphite ball (not to scale)

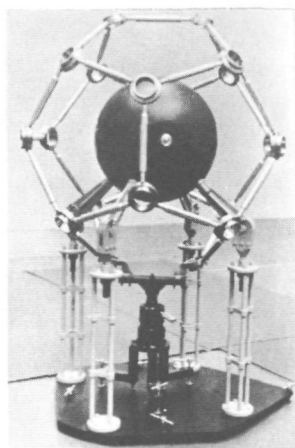


Fig. 3.5 The dodecahedron around the ball

Impurity data as obtained from manufacturer (Anglo Great Lakes Corporation Ltd., Newburn Haugh, England):

graphite : nuclear grade A, type im2

impurities :

ash 300 ppm

iron 50 ppm

titanium 25 ppm

vanadium 10 ppm

boron 0.8 ppm

thermal neutron absorption cross-section 4.15 mbarn

Other properties of graphite have been extensively studied especially in the English literature. See for example (36,37).

Around the ball a regular dodecahedron has been constructed to hold the 20  $\text{BF}_3$  tubes. See Fig. 3.5. The dodecahedron can be rotated about a vertical axis to give the correct position to the  $\text{BF}_3$  tubes in relation to the beam direction. When the oscillator tube is put through the ball, the free turn of the dodecahedron is rather small. To ensure controlling of the detector efficiency, it is also possible to vary the distance from each of the  $\text{BF}_3$  tubes to the surface of the ball. For a better signal/background ratio the  $\text{BF}_3$  tubes have been mounted tangentially to the ball. See sec. 3.3.2.

To reduce the background signal, the ball detector has been surrounded by a wheelable cadmium box. Holes at the sides of the box permit passage of the oscillator tube, while a hole at the back makes possible easy handling of the  $B^2-C$  scatterer.

The sample oscillator has been made of aluminium to reduce its influence upon the neutron beam. See Fig. 3.6. The oscillator tube consists of two sample ovens (or open sample holders) and several aluminium tubes with screw connections. The stroke of the pneumatic oscillator drive is about 80 cm. The oscillator drive has been fixed to the ground and the distance between it and the first oven as well as that between the two ovens can be controlled.

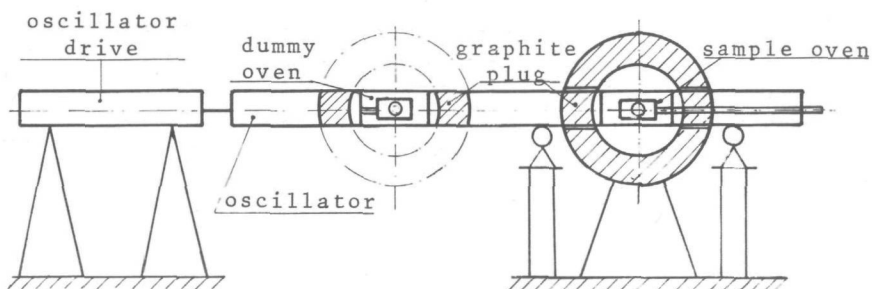


Fig. 3.6 The sample oscillator

To reduce the neutron leakage through the oscillator holes in the graphite ball, graphite plugs have been mounted at both sides of the sample ovens in the oscillator tube.

The construction of the sample ovens can be seen in Fig. 3.7. A cylindrical aluminium oxide sample holder has been fixed to the lid of the oven. The sample is heated electrically by means of a niobium wire wound around the sample holder. The oven is kept at a vacuum of  $10^{-3}$  to  $10^{-2}$  Torr to reduce heat transport by convection and to prevent oxidation of the samples. Between the sample and the aluminium wall of the oven tube four heat shields are provided to reduce heat transport by radiation. The sample temperature can be raised easily and rather fast up to  $1200^{\circ}\text{C}$  ( $10^{\circ}\text{C}/\text{min}$ ), while the temperature at the

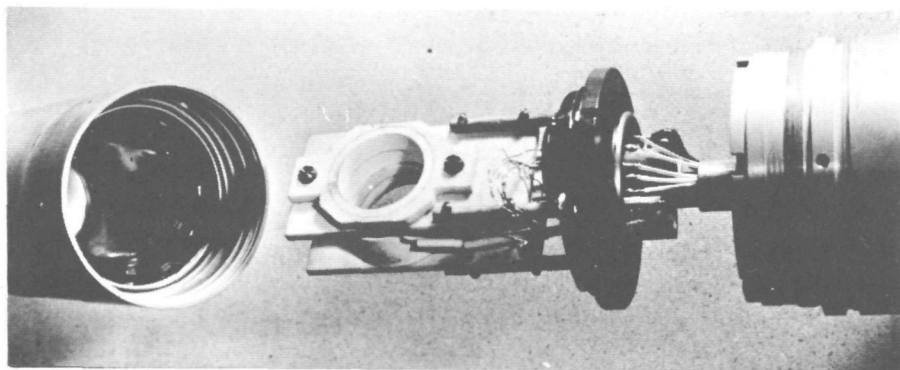


Fig. 3.7 The sample oven

outer wall of the oven does not exceed about  $150^{\circ}\text{C}$ . To prevent damage from thermal stress at the thermocouple and current leads through the oven lid, air cooling can be applied. Local perforations have been made in the oscillator wall for ventilation purposes, thus providing air cooling of the graphite ball as well.

Some disadvantages of the ovens should be mentioned.

The niobium wire becomes very brittle through heating and evaporates rather rapidly at elevated temperatures ( $> 900^{\circ}\text{C}$ ), which reduces the useful life of the ovens considerably (10-40 hours).

At a breakdown of the heating current at temperatures over  $800^{\circ}\text{C}$  the temperature of the sample and the  $\text{Al}_2\text{O}_3$  holder decreases so rapidly that holder or sample or both often break.

The 20  $\text{BF}_3$  tubes (L.M.T. 15 Ne 14/ 5) are divided into four groups of five detectors, each group being connected to one of four pre-amplifiers. After passing through the main amplifier and the threshold discriminator of the  $\gamma$  pulses, the neutron signal is recorded by a PDP-9 (DEC) computer, which is programmed to eliminate most of the electronic noise pulses, to control the oscillator position, and to apply the corrections and formulae of sec. 3.10.

### 3.3. *Maximizing the signal/background ratio*

To maximize the signal/background ratio, the signal should be maximized and the background should be minimized.

To maximize the signal, the material and the position of the scatterer in the centre of the reactor have been optimized.

To minimize the background, several measures have been taken to reduce the influence of the reactor hall background and the influence of neutrons from the beam not hitting the sample.

### 3.3.1. The neutron beam

#### 3.3.1.1. The neutron scatterer

To maximize the intensity of the neutron beam at a constant reactor power, a neutron scatterer has been put in the centre of the reactor core. See Fig. 3.1.

A good neutron scatterer should consist of a material with:

- large  $\Sigma_s$
- $\Sigma_s(E)$  constant  $1 \text{ eV} < E < 50 \text{ keV}$
- small  $\Sigma_a$
- heavy nuclei

Nickel, iron and lead have been compared as scattering materials. See Fig. 3.8.

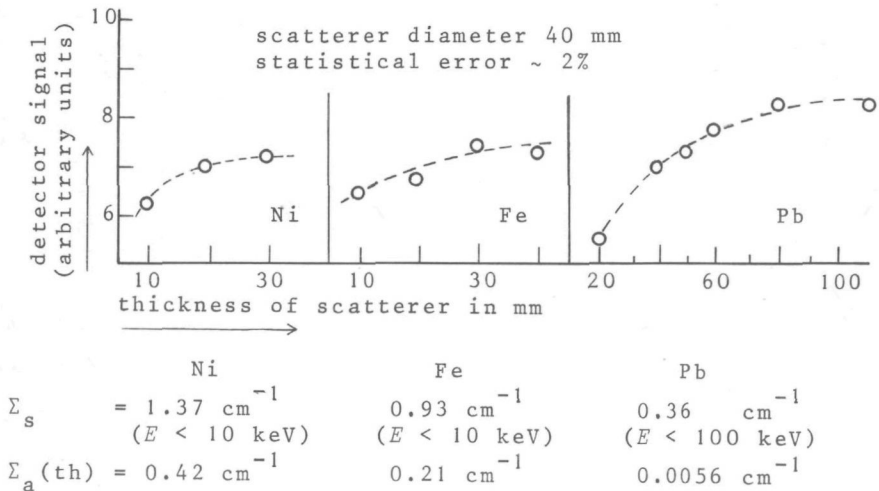


Fig. 3.8 Several scatterer materials in the centre of the reactor

Lead giving at least as much detector signal as iron or nickel, the other properties indicated it as being the best choice of scattering material.

The position of the lead scatterer has been optimized by a series of measurements with the scatterer in different positions in the

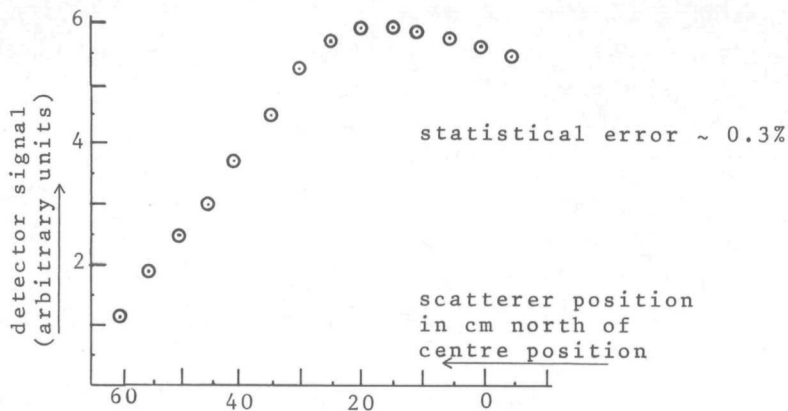


Fig. 3.9 Choice of the position of the neutron scatterer irradiation tube. From Fig. 3.9 it appears that the optimum position is found between 5-20 cm north of the centre position.

The neutron scatterer used in all detector measurements is a cylinder of lead: diameter 40 mm; length 110 mm; position 9-20 cm north of the centre position.

### 3.3.1.2. The neutron beam profile

To be sure that all neutrons coming from the collimator do hit the sample, a check has been made on the beam profile.

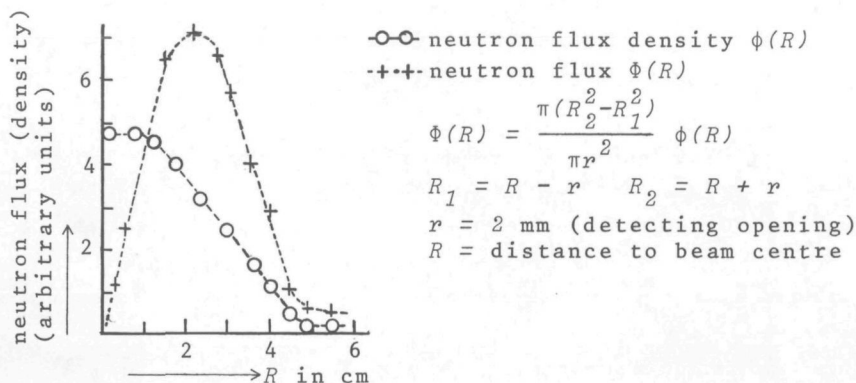


Fig. 3.10 The neutron beam profile

The effective length of the neutron collimator is 1690 mm. At 3380 mm behind the collimator a scan of the beam profile has been carried out with a detecting opening of 4 mm diameter. See Fig. 3.10.

No significant deviation from the expected beam profile has been observed.

### 3.3.1.3. *The neutron filters*

The position of the neutron filters has been chosen right in front of the collimator opening at the reactor side (see Fig. 3.1) to prevent as much as possible that the neutrons scattered by the air between the filter and the detector, should disturb the filtered neutron spectrum. To generate fast neutron spectra with a low energy tail as shown in Fig. 1.2, a pure  $\frac{1}{v}$  absorber (or better  $\Sigma_t \sim \frac{1}{v}$ ) seems a good possibility. Three spectra have been used in the neutron absorption measurements of chapter 5. See Fig. 2.5.

$0 B_4C$ : No filter has been applied. The thermal reactor spectrum scattered from the lead scatterer hits the sample. The cadmium foil at the detector side of the collimator (see Fig. 3.4) absorbs the thermal neutrons.

$4 B_4C$ : A boron carbide disk of 4 mm in thickness generates an intermediate neutron spectrum. The cadmium foil at the detector side of the collimator absorbs the thermal neutrons that have passed the  $B_4C$  filter and the thermal neutrons generated by scattering by the air inside the collimator.

$12 B_4C$ : A boron carbide disk of 12 mm in thickness generates a fast neutron spectrum resembling the steam cooled fast reactor spectrum of Fig. 1.2. The cadmium foil at the detector side of the collimator absorbs the few thermal neutrons scattered by the air inside the collimator.

In view of the maximization of the signal/background ratio, pure  $^{10}B$  filters would have been a better choice.

### 3.3.2. *Improvements of the detector*

To maximize the signal/background ratio some improvements at the detector side have been made.

To reduce the background neutrons from the reactor hall, a wheelable cadmium box has been constructed around the detector.

The signal of the reactor hall background has been reduced by a factor 35 by using the cadmium box.

To stabilize the influence of neutrons scattering from the beam before hitting the sample, an aluminium vacuum tube has been fitted between the collimator opening and the centre of the graphite ball. See Fig. 3.4. It appears that the influence of the neutrons scattered by the aluminium front and end plates (thickness 0.5 mm) is about the same as that exercised by the neutrons scattered by the replaced air column.

Changing the position of the  $\text{BF}_3$  tubes with respect to the graphite ball from radial to tangential raised the detector signal by a factor 2.4, while the background signal remained about the same. The main cause of this improvement is found to be the neutron absorption by the heads of the  $\text{BF}_3$  tubes.

### 3.3.3. *The background signal*

Measurements of the background signal have shown the linearity of the dependence of the background on the reactor power.

As a consequence it is possible to express the background signal as a constant fraction of the total reference detector signal, which makes it easy to correct for it by means of the computer.

The results of the background measurements for the three different neutron spectra are listed in Table 3.1.

$bg$  is the cumulative background fraction of the reference signal

Table 3.1

The measured background fractions of the reference signal

	$0 B_4C$	$4 B_4C$	$12 B_4C$
$bg$	0.0872 $\pm 0.0008$	0.1134 $\pm 0.0010$	0.1562 $\pm 0.0012$
$bg(\text{without } Bi-C \text{ scatterer})$	0.0857 $\pm 0.0008$	0.1117 $\pm 0.0010$	0.1530 $\pm 0.0012$
$wac$	0.0534 $\pm 0.0006$	0.0537 $\pm 0.0008$	0.0578 $\pm 0.0010$

$R_{abs}^0$  (see sec. 3.10.), caused by the reactor hall background and by the neutron scattering from the aluminium vacuum tube and the oven wall in front of the target sample.

$bg$  (without  $Bi-C$  scatterer) has the same origin as  $bg$  but is slightly smaller than  $bg$  because of the absence of the  $Bi-C$  scatterer. It is used when measuring the fraction of the detector signal due to neutron scattering in the sample (see sec. 3.5. and sec. 3.10.). In the computer corrections of the measurements of ch. 5,  $bg$  (without  $Bi-C$  scatterer) has been replaced by  $bg$  because of the very slight importance of the difference.

$wac$  is the background signal expressed as a fraction of the reference signal  $R_{abs}$  (see sec. 3.10.), caused by the neutron scattering from the oven wall behind the sample and the air column behind the oven wall.  $wac$  is also used in the determination of the scattered fraction of the detector signal.

#### 3.4. The insensitive time of the detector

Owing to the coupling of five  $BF_3$  tubes to one preamplifier, a rather long insensitive time of the detector after the recording of a pulse can be expected. This will lead to considerable counting loss, even at

moderate counting rates. So a correction for the insensitive time of the detector will be necessary.

Let  $R_t$  ( $R_m$ ) and  $W_t$  ( $W_m$ ) be the true (measured) pulse rates of the detector using the oscillator with a non-absorbing reference sample and an absorbing sample with about  $0.5 \times$  the reference signal, respectively. As the neutron spectrum does not change, the quotient  $\frac{R_t}{W_t}$  is independent of the reactor power.

The counting rates  $R_m$  and  $W_m$  have been determined in a series of 11 measurements at 11 different reactor power levels.

The true pulses having a Poisson distribution, the relation between the measured and the true pulse rates is known (38):

$$\begin{aligned} R_t &= R_m e^{R_t \tau} \\ W_t &= W_m e^{W_t \tau} \end{aligned} \quad (3.1)$$

The insensitive time  $\tau$  of the detector which occurs after a pulse, has been determined with a least-squares fit:

$$\frac{d}{d\tau} \sum_i (q_i - \bar{q})^2 = 0 \quad (3.2)$$

with

$$q_i = \left( \frac{R_t}{W_t} \right)_i \quad (3.3)$$

and

$$\bar{q} = \frac{1}{N} \sum_{i=1}^N \left( \frac{R_t}{W_t} \right)_i \quad (N = 11) \quad (3.4)$$

At  $\bar{q} = 2.0595 \pm 0.0022$  the insensitive time is found to be  $\tau = 33.4 \mu\text{s}$ .

The uncertainty in  $\tau$ , corresponding to the uncertainty in  $\bar{q}$  depends on the counting rate of the detector and varies from  $1 \mu\text{s}$  at 1000 p/s to  $0.2 \mu\text{s}$  at 5000 p/s.

In all the detector measurements in the following chapters the counting rates to be mentioned have been corrected for the insensitive time.

### 3.5. *The position of the dodecahedron and the slowing down effect of neutrons in the target sample*

#### 3.5.1. *Introduction*

In the explanation of the principles of the graphite ball detector in sec. 2.1.3. some simplifications and omissions have been accepted implicitly. The main points are:

- (a) The amplitude of the efficiency wave diminishes with increasing neutron energy, so the correct position of the dodecahedron depends on the energy.
- (b) Neutrons scattered in a target sample do not only change their direction, but are also slowed down in their energy, which increases their detection efficiency.

As the independence of neutron scattering in the sample is essential to the accuracy of the detector principle, the gradient of the efficiency wave in the beam direction and hence the energy dependence of the correct position of the dodecahedron should be minimal. For practical reasons described in sec. 3.5.2., a roughly correct position of the dodecahedron and the  $\text{BF}_3$  tubes is chosen, so that a correction factor,  $c_{12}$ , has to be determined for each neutron spectrum.

To obtain a good interpretation of the detector signal with a target sample in the ball, the fraction of the signal caused by the scattered neutrons must be corrected by the factor  $c_{12}$  and by a factor  $c_{mod}$  for the increase in efficiency due to the slowing down of the neutrons in the sample.

The required accuracy of the corrections depends on the purpose of the measurements.

If the detector is used to determine the nuclear Doppler effect of a

target sample, the quantity of interest  $D$  is the relative change of the absorption signal (for a more accurate definition of  $D$ , see sec. 3.10).

$$D = \frac{abs_w - abs_c}{abs_c} \quad (3.5)$$

$abs_w$  ( $abs_c$ ) is the change of the detector signal caused by the neutron absorption of the warm (cold) sample. Both corrections do not depend on the sample temperature.

Because  $abs_w - abs_c$  is a rather small quantity, the accuracy of  $D$  is of the order of 10% (see sec. 5.3.). So an absolute error of 1-5% of  $abs_c$  due to the temperature independent corrections can be accepted and a simple estimate of both corrections will be sufficient. If, however, the detector is used to determine the absolute value of the absorption signal  $abs_c$ , the corrections should be as accurate as possible.

In the following sections two distinct ways to determine the corrections are described. The rather obvious experimental determination by means of sample substitution of sec. 3.5.4. gives a coarse approach of the combined corrections, which may, however, easily, lead to unacceptable errors. The mixed experimental and calculated determination of sec. 3.5.5. gives a more accurate estimate of  $mod$  and  $c12$ .

Both methods require the determination of the scattered fraction of the detector signal described in sec. 3.5.3.

### 3.5.2. *The position of the dodecahedron*

Before fixing the position of the dodecahedron the influence of the holes at the beam entrance and at the oscillator passage on both sides of the ball has to be considered.

Measurements have been performed regarding the influence of a hole 42 mm in dia. at the east side of the ball (Fig. 3.11), which can be

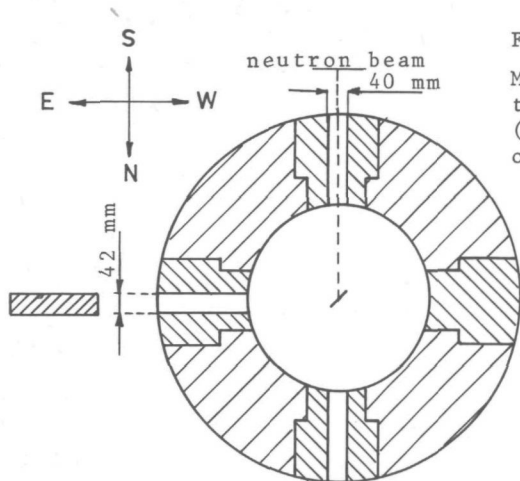


Fig. 3.11

Measurement of the influence of a hole (dia. 42 mm) in the wall of the graphite ball

compared with the hole of the beam entrance (dia. 40 mm). Assuming the scattering of the neutrons in a rather thin (3 mm) sample of lead is isotropic from the centre of the ball, the quotients of the detector signals (without hole)/(with hole) have been determined in the three standard spectra. See Table 3.2.

Measurements carried out with an isotropic americium-beryllium neutron source in various polyethylene balls with diameters up to 13.6 cm in the centre of the graphite ball, have confirmed the energy dependence as well as the order of magnitude of the influence of the hole.

On the basis of these measurements the influence of the oscillator

Table 3.2

The quotients of the detector signals (without hole)/(with hole) in different neutron spectra

spectrum	<u>without hole</u> with hole	statistical error (%)
$0 B_4C$	1.016	0.2
$4 B_4C$	1.017	0.3
$12 B_4C$	1.030	0.4

passage hole has been estimated at about 2-4% depending on the energy. Therefore, the influence of the beam entrance hole and the two oscillator passage holes together upon the overall mean detector efficiency of isotropically scattered neutrons varies from about 5 to 10% depending on the energy spectrum.

The majority of the neutrons in beam direction hitting the (closed) north side of the ball are detected at this side where there are no holes, and where, consequently, the influence is less than the above mentioned 5-10%.

To reduce the difference between the influence of the holes upon the isotropically scattered neutrons and upon the neutrons flying in the beam direction, the bismuth cylinder (dia. 40 mm; thickness 40 mm) mentioned in sec. 3.2., has been mounted on top of the graphite plug (see Fig. 3.4). Part of the neutrons in the beam direction is now scattered in the bismuth cylinder, which has a more central position and which hardly changes the neutron energy.

Fig. 3.12 shows the detection pattern around the ball, obtained from

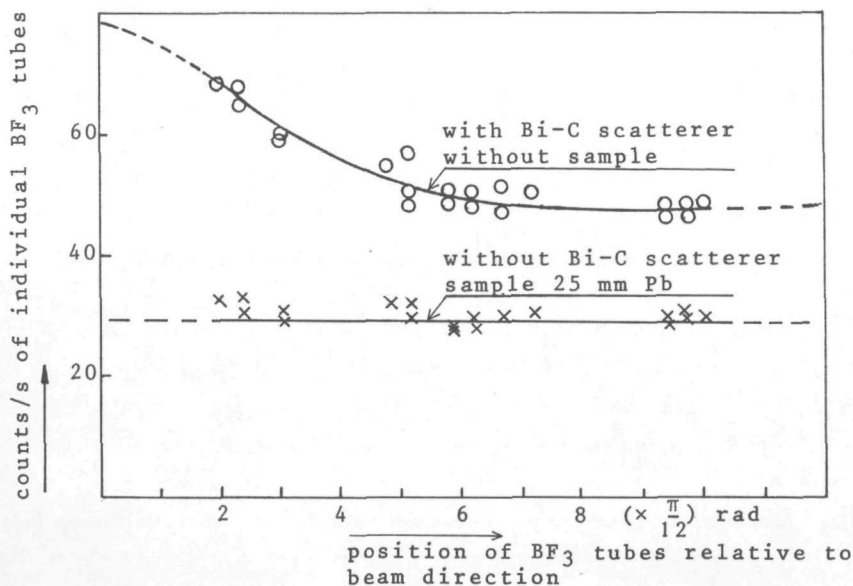


Fig. 3.12 Detection pattern of the  $\text{BF}_3$  tubes around the ball in the  $^{12}\text{B}_4\text{C}$  spectrum

successive measurements of the several  $\text{BF}_3$  tubes in the case of the  $12 B_4C$  spectrum.

From this pattern an estimate can be made of the maximum and the minimum counting rates that are capable of being obtained as a function of the position of the dodecahedron (i.e. the amplitude of the efficiency wave in the beam direction). The maximum counting rate is found when a  $\text{BF}_3$  tube is positioned just in the centre of the beam direction. The minimum is found when the beam points to the centre of a pentagon of the dodecahedron. With  $\text{resp}(\alpha)$  as the response of a  $\text{BF}_3$  tube in direction  $\alpha$ , relative to the beam direction, the maximum counting rate, with an estimate of  $\text{resp}(0) = 75$  (85) c/s, is:

$$\begin{aligned} \text{resp}(0) + 3 \text{resp}\left(2.795\frac{\pi}{12}\right) + 6 \text{resp}\left(4.70\frac{\pi}{12}\right) + 6 \text{resp}\left(7.30\frac{\pi}{12}\right) + \\ + 3 \text{resp}\left(9.21\frac{\pi}{12}\right) + \text{resp}(\pi) = 1056 \text{ (1066) c/s} \end{aligned}$$

and the minimum counting rate is:

$$\begin{aligned} 5 \text{resp}\left(2.49\frac{\pi}{12}\right) + 5 \text{resp}\left(5.29\frac{\pi}{12}\right) + 5 \text{resp}\left(6.71\frac{\pi}{12}\right) + \\ + 5 \text{resp}\left(9.51\frac{\pi}{12}\right) = 1055 \text{ c/s} \end{aligned}$$

So the order of magnitude of the amplitude is 1% or less in the  $12 B_4C$  spectrum and with the  $Bi-C$  scatterer in the ball.

As the difference between the influence of the holes upon the isotropically scattered neutrons and upon the neutrons flying in the beam direction is still more than about 1%, the  $\text{BF}_3$  tubes in the positions closest to the neutron beam at the north side of the ball have to be lifted up some centimeters from the ball in order to reduce the efficiency in the beam direction and to compensate the stronger influence of the holes at the other sides of the ball.

Assuming the absorption and moderation by a 25-mm lead (trade quality) sample can be neglected, the correct position of the dodecahedron and the  $\text{BF}_3$  tubes is found when the detector signal is not changed by the presence of the sample.

As the accurate experimental determination of the correct position takes a great deal of time, it is practical to choose a reasonable position by using the lead sample and to determine a correction factor  $c_{12}$  afterwards for each energy spectrum.

### 3.5.3. The scattered fraction

Let  $W_{abs,o}$  be the detector signal, corrected for the background, without a target sample:

$$W_{abs,o} = \int_0^{\infty} \Phi_o(E) \cdot eff_b(E) dE \quad (3.6)$$

$\Phi_o(E)$  is the quantity of neutrons per second at energy  $E$  incident to the sample holder.

$eff_b(E)$  is the detector efficiency of neutrons with energy  $E$  in the beam direction.

Now put a sample into the sample holder. Let  $W_{abs}$  be the detector signal, corrected for the background:

$$W_{abs} = \int_0^{\infty} \Phi_o(E) \cdot t(E) \cdot eff_b(E) dE + \int_0^{\infty} \Phi_o(E) \left[ 1 - t(E) - abs(E) \right] \left[ \int_0^{\infty} \int_0^{4\pi} mod(E \rightarrow E', \Omega) \cdot eff(E', \Omega) d\Omega dE' \right] dE \quad (3.7)$$

$t(E)$  is the fraction of  $\Phi_o(E)$  passing through the sample without any interaction.

$abs(E)$  is the fraction of  $\Phi_o(E)$  absorbed in the sample.

$mod(E \rightarrow E', \Omega)$  is the probability density of neutrons with energy  $E$  of changing their energy to  $E'$  in the direction  $\Omega$  at the interaction in the sample.

$eff(E', \Omega)$  is the detector efficiency of neutrons with energy  $E'$  flying in the direction  $\Omega$  from the sample.

With the definition

$$mod(E) = \frac{\int_0^{\infty} \int_0^{4\pi} mod(E \rightarrow E', \Omega) \cdot eff_b(E', \Omega) \, d\Omega dE'}{eff_b(E)} \quad (3.8)$$

(3.7) becomes:

$$W_{abs} = \int_0^{\infty} \Phi_o(E) \cdot t(E) \cdot eff_b(E) \, dE + \int_0^{\infty} \Phi_o(E) \left[ 1 - t(E) - abs(E) \right] \cdot mod(E) \cdot eff_b(E) \, dE \quad (3.9)$$

$mod(E)$  can be seen as an apparent change in the number of neutrons leaving the sample after a scattering event.

Now the scattered fraction  $scfr$  can be defined:

$$scfr = \frac{\int_0^{\infty} \Phi_o(E) \left[ 1 - t(E) - abs(E) \right] \cdot mod(E) \cdot eff_b(E) \, dE}{W_{abs,o}} \quad (3.10)$$

and  $W_{abs}$  can be expressed as:

$$W_{abs} = \int_0^{\infty} \Phi_o(E) \cdot t(E) \cdot eff_b(E) \, dE + scfr \cdot W_{abs,o} \quad (3.11)$$

The quantity of interest in the Doppler or absorption measurements is the integral neutron absorption signal  $abs$ :

$$abs = \frac{\int_0^{\infty} \Phi_o(E) \cdot abs(E) \cdot eff_b(E) \, dE}{W_{abs,o}} \quad (3.12)$$

To be able to determine  $abs$  from the detector signals  $W_{abs,o}$  and  $W_{abs}$ , the part of the signal from the scattered neutrons,  $scfr \cdot W_{abs,o}$ , must be corrected for the apparent change in the number of neutrons, due to the change in energy and the change in detection efficiency in other directions than that of the beam.

With the combined correction factors  $emod.c12$ :

$$emod.c12 = \frac{\int_0^{\infty} \Phi_o(E) \left[ 1-t(E)-abs(E) \right] . eff_b(E) dE}{\int_0^{\infty} \Phi_o(E) \left[ 1-t(E)-abs(E) \right] . mod(E) . eff_b(E) dE} \quad (3.13)$$

and with (3.6), (3.11) and (3.12) follows:

$$W_{abs} = W_{abs,o} \cdot \{1-abs+(1-emod.c12) . scfr\} \quad (3.14)$$

or:

$$abs = 1 - \frac{W_{abs}}{W_{abs,o}} + (1-emod.c12) . scfr \quad (3.15)$$

Neglecting the influence of the new hole in the ball and neglecting the signal from the neutrons scattered in the back wall of the oven and in the air column behind the sample,  $scfr$  can be measured by removing the  $Bi-C$  scatterer from the ball. The detector signal  $W_{sc}$ , after correction for the background, is now:

$$W_{sc} = \int_0^{\infty} \Phi_o(E) \left[ 1-t(E)-abs(E) \right] . mod(E) . eff_b(E) dE \quad (3.16)$$

and  $scfr$  can be found from:

$$scfr = \frac{W_{sc}}{W_{abs,o}} \quad (3.17)$$

After determination of  $emod.c12$ , equation (3.15) can be solved.

3.5.4. *An experimental determination of the correction for the slowing down effect in the sample and for the position of the dodecahedron (cmod.c12) by means of sample substitution*

In the absorption measurements of chapter 5 the nuclear Doppler effect of  $UO_2$  and  $ThO_2$  has been examined.

Knowing that the temperature independent error of the absolute absorption may be several per cent (see sec. 3.5.1.), it is rather obvious to replace the  $UO_2$  and  $ThO_2$  samples by the non-absorbing  $PbO_2$  to determine the combined correction *cmod.c12*, neglecting the differences in the cross-sections and the molecule densities. As the neutron absorption cross-section of  $PbO_2$  is very small, the absorption signal *abs* may be taken zero. After measuring  $W_{abs,o}$ ,  $W_{sc}$  and  $W_{abs}$ , the scattered fraction *scfr* and *cmod.c12* can be determined from (3.17) and (3.14).

To get an impression of the accuracy of this substitution method, the values of *cmod* for a series of  $PbO_2$  samples and the  $UO_2$  and  $ThO_2$  samples of chapter 5 have been calculated with the Monte Carlo computer program MCTRANS (see sec. 4.4.).

The results of these calculations are shown in Fig. 3.13.

Now *cmod* for  $UO_2$  and  $ThO_2$  turns out to be 1-4% smaller than *cmod* for  $PbO_2$ , or, what is more relevant to formula (3.14),  $(1 - cmod)$  for  $UO_2$  and  $ThO_2$  is 1.5 to almost 3 times as large as for  $PbO_2$ .

In the calculations of MCTRANS the mean lethargy step of the elastically scattered neutrons has been recorded as well. Using the relations (4.8) and (4.9) it is easy to calculate *cmod* in the case of elastic scattering only. Table 3.3 gives the results of the thin and the thick samples and shows the small differences due to elastic scattering. The great difference between the curves of Fig. 3.13 is apparently due to the difference in the inelastic scattering cross-sections.

The influence of this great difference on *abs* of formula (3.15) varies from about 3% in the case of the thin  $UO_2$  and  $ThO_2$  samples, using the  $O B_4 C$  spectrum, to about 40% in the case of the thick samples and the fast  $12 B_4 C$  spectrum.

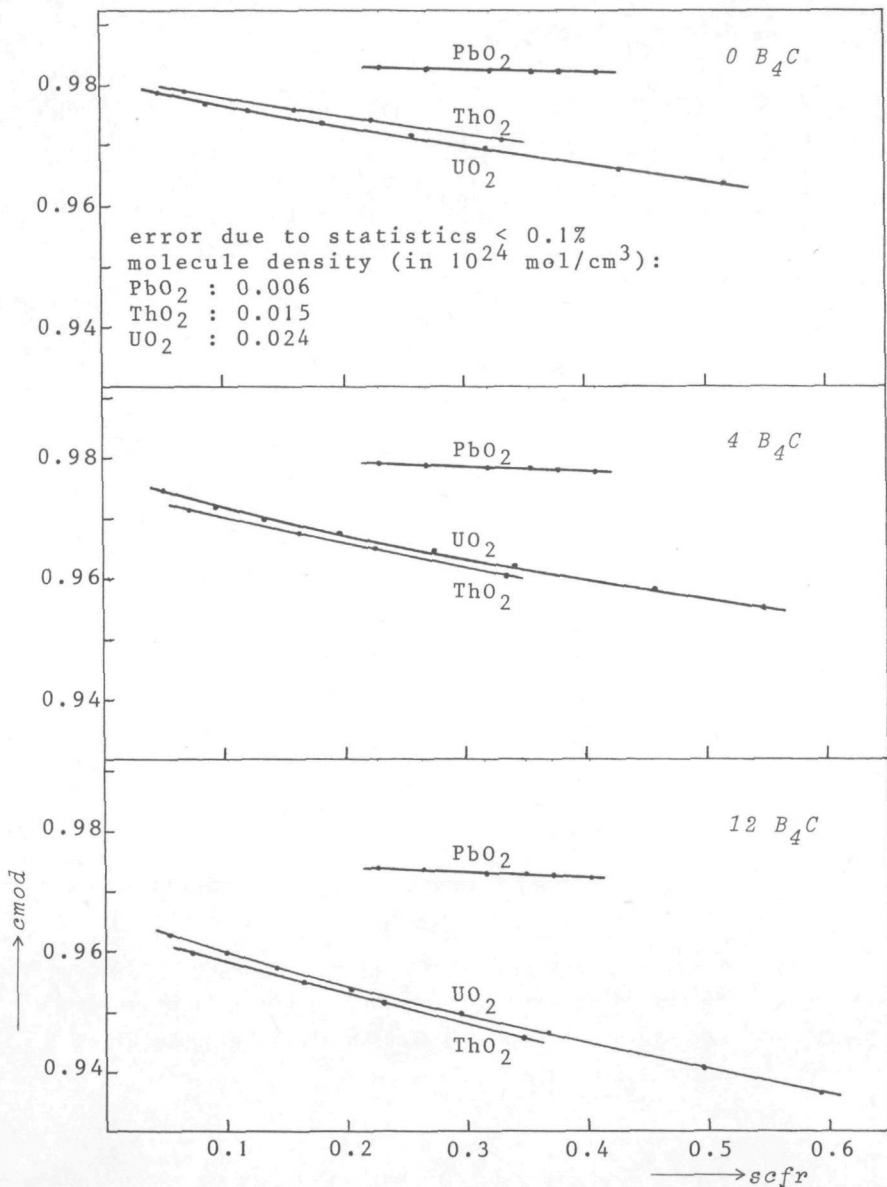


Fig. 3.13 Intercomparison of the calculated slowing-down corrections  $cmod$  for  $PbO_2$ ,  $ThO_2$  and  $UO_2$

Table 3.3

Calculations of  $\epsilon_{mod}$  in the case of elastic scattering only

sample	leth.step $-\overline{\Delta \ln E}$	$\epsilon_{mod}$ (elastic sc.)
PbO <sub>2</sub> (thin)	0.0653	0.9855
PbO <sub>2</sub> (thick)	0.0679	0.9849
UO <sub>2</sub> (thin)	0.0533	0.9882
UO <sub>2</sub> (thick)	0.0926	0.9795
ThO <sub>2</sub> (thin)	0.0516	0.9886
ThO <sub>2</sub> (thick)	0.0681	0.9849

The conclusion of this rather obvious substitution method must be that when testing heavy material samples, the differences in the influence of the slowing down due to inelastic scattering may easily become unacceptable and will not be used in the measurements of chapter 5.

### 3.5.5. A mixed experimental and calculatory determination of $\epsilon_{mod}$ .c12.

A more accurate way to determine  $\epsilon_{mod}$  separately has already been indicated in sec. 3.5.4.

If only the inelastic scattering cross-section of a sample material and its chemical composition and density are rather well known, the slowing down correction  $\epsilon_{mod}$  can be calculated by the Monte Carlo computer code MCTTRANS. The way in which  $\epsilon_{mod}$  is calculated by MCTTRANS will be described in sec. 4.4.

$\epsilon_{mod}$  has been calculated for the UO<sub>2</sub> samples used in the measurements of chapter 5. The results are shown in Fig. 3.13. The accuracy of the

calculations is mainly determined by the accuracy of the inelastic scattering cross-sections.

Schmidt (39) gives an extensive comparison of the inelastic scattering cross-section measurements carried out by several authors and referring to different materials; a typical value of the inaccuracy  $\Delta\sigma_{inel}/\sigma_{inel}$  appears to be 10-20%.

To get an idea of the influence of this inaccuracy, the calculations of  $c_{mod}$  for  $\text{ThO}_2$  (thin and thick samples) have been repeated, supposing a reduction of the inelastic scattering cross-sections by 10% and 20% respectively. Table 3.4 gives the comparison of these calculations.

Table 3.4

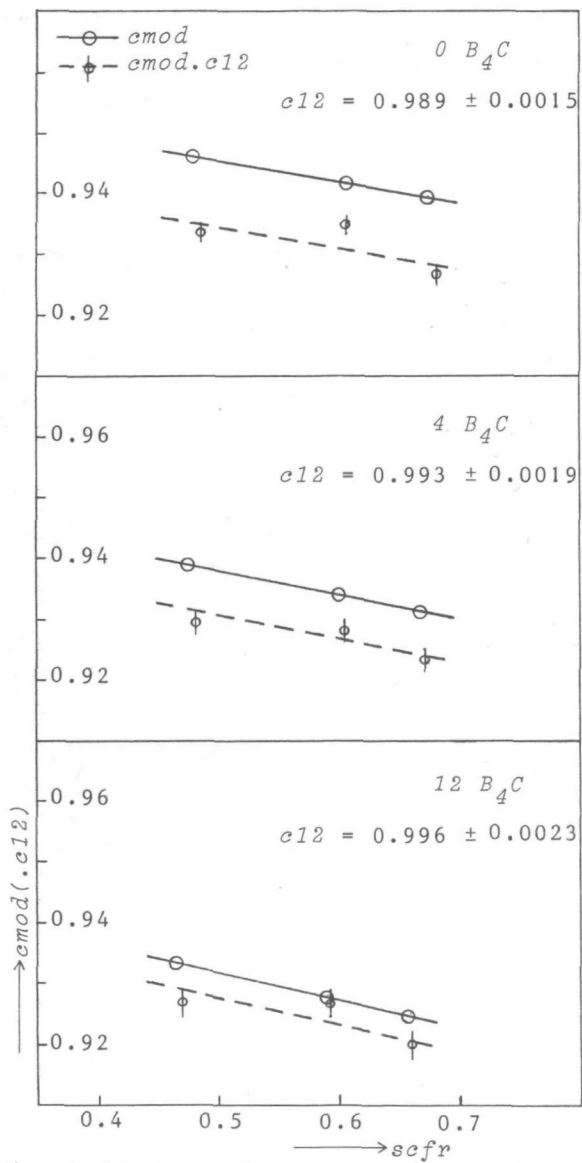
The influence upon  $c_{mod}$  of the inaccuracy of the inelastic scattering cross-section of  $\text{ThO}_2$

<i>c<sub>mod</sub></i> of $\text{ThO}_2$ samples in $^{12}\text{B}_4\text{C}$ spectrum			
sample thickness mm	$\sigma_{inel}^-$ 0%	$\sigma_{inel}^-$ 10%	$\sigma_{inel}^-$ 20%
2.6	0.9596	0.9621	0.9646
15	0.9457	0.9490	0.9526

After calculating  $c_{mod}$ , the correction factor  $c_{12}$  has yet to be determined.

The mean detector efficiency for neutrons leaving the sample after one or more collisions in the sample is further influenced by the slowing down in the furnace sample holder ( $\text{Al}_2\text{O}_3$ ), by the holes in the graphite ball (see sec. 3.5.2.) and by the deviation from the correct position of the dodecahedron and the  $\text{BF}_3$  tubes. The correction for these influences is taken together in the correction factor  $c_{12}$ .

Therefore a detailed calculation of  $c_{12}$  would be very complicated. Assuming the influence of the sample material on  $c_{12}$  is small,  $c_{12}$  can be determined experimentally by means of a reference material with very well-known properties.



graphite samples :  
 dia.: 40 mm  
 thick.:  
 15, 21, 25 mm  
 material :  
 nuclear grade A  
 type im2  
 composition:  
 see sec. 3.2.

Fig. 3.14 Comparison of  $c_{mod}$  as calculated and  $c_{mod.c12}$  as measured for several graphite samples

As the inelastic scattering cross-section at energies below 5 MeV is known and since the absorption cross-section of carbon can be neglected, while the scattering cross-section is nearly constant up to 200 keV,  $c_{12}$  has been determined for several graphite samples (nuclear grade A, type im2, see sec. 3.2.) by calculating  $c_{mod}$  and measuring  $c_{mod} \cdot c_{12}$ . The results are shown in Fig. 3.14.

The values of  $c_{12}$  in the three different neutron spectra can be seen as a measure of the energy dependence of the accuracy of the graphite ball measurements. The values of  $c_{12}$  will be rather accurate for measurements with other sample materials than carbon, if only the spectrum of the scattered neutrons is not very different from the incident spectrum on the sample.

If the scattered neutron spectrum is faster than the incident spectrum, as is the case with strongly absorbing samples,  $c_{12}$  from Fig. 3.14 tends to be too low. If the scattered neutron spectrum is softer than the incident spectrum, as is the case with hydrogen,  $c_{12}$  will be too high.

### 3.6. The reference factor

#### 3.6.1. General

To be able to reduce the influence of short-term and long-term changes in the reactor power, the air humidity, the graphite ball temperature and other circumstances, the graphite ball detector has been equipped with a sample oscillator having two sample ovens, which can be positioned in the graphite ball alternatively (see Fig. 3.1).

The east side oven contains a reference sample consisting of 25-mm lead and is not heated. The west side oven contains the unknown sample. The detector signal  $R_{abs}$ , with the east side oven and the reference sample in position and with the *Bi-C* scatterer in the ball, can be used as a reference signal. The detector signal  $R_{sc}$ , with the east side oven and the reference sample in position but without the *Bi-C* scatterer, being related to  $R_{abs}$  by

$$bigratio = \frac{R_{abs}}{R_{sc}} \quad (3.18)$$

can be used as a reference signal in the measurements without the Bi-C scatterer.

With

$$ref_b = \frac{R_{abs}}{W_{abs,o}} \quad (3.19)$$

relation (3.15) becomes:

$$abs = 1 - \frac{W_{abs} \cdot ref_b}{R_{abs}} + (1 - mod.c12) \cdot scfr \quad (3.20)$$

and with (3.18) and (3.19), relation (3.17) becomes:

$$scfr = \frac{W_{sc} \cdot ref_b}{R_{sc} \cdot bigratio} \quad (3.21)$$

When the west side oven is heated, the aluminium oven wall, and hence the west side of the oscillator tube, is heated also. The temperature of the outer oven wall may reach about 150°C at a sample temperature of 1200°C.

The counting rate of the graphite ball detector is now influenced by two effects:

- Owing to the expansion of the aluminium oscillator tube, the graphite plugs at both sides of the west side oven are moved westward from their cold position 0.5-1 mm (at 1200°C sample temperature). So the influence of the oscillator passage holes, as discussed in sec. 3.5.2., is changed.
- The temperature of the graphite plugs at both sides of the west side oven is also raised to about 80°C (at 1200°C sample temperature). The peak of the "Maxwell-Boltzmann spectrum" of the thermalized neutrons in the plugs shifts towards higher energy, which reduces their detection efficiency in the BF<sub>3</sub> tubes.

The influence of these temperature dependent effects may be expected

to be different (i.e. stronger) for the scattered neutrons from that for the neutrons in beam direction.

Formula (3.20) may now be written as:

$$abs = 1 - \frac{W_{abs} \cdot ref_b(exp)}{R_{abs}} + \{1 - cmod \cdot c12 \cdot ref_{sc}(exp)\} \cdot scfr \quad (3.22)$$

$ref_b(exp)$  is  $ref_b$  as a function of the oscillator expansion  $exp$  which is used as a measure of the effects mentioned above.

$ref_{sc}(exp)^\dagger$  is the additional correction needed for the scattered neutrons as a function of the oscillator expansion  $exp$  and formula (3.21) becomes:

$$scfr = \frac{W_{sc} \cdot ref_b(exp)}{R_{sc} \cdot bicratio} \quad (3.23)$$

Sec. 3.6.2. gives the measurements of  $bicratio$ ,  $ref_b(exp)$  and  $ref_{sc}(exp)$ .

### 3.6.2. Measurement of the temperature dependent reference factor

The ratios of the reference signals  $R_{abs}$  and  $R_{sc}$  have been measured for the three standard spectra by repeated measurement by turns of  $R_{abs}$  and  $R_{sc}$ .

The results are shown in Table 3.5.

The temperature dependent reference factor for neutrons in the beam direction has been measured by heating the empty west side oven and measuring the detector signals and the total oscillator expansion simultaneously. With  $abs = 0$  and  $scfr = 0$  it follows from formula (3.22) that

$$ref_b(exp) = \frac{R_{abs}}{W_{abs}} = \frac{R_{abs}}{W_{abs,0}} \quad (3.24)$$

---

<sup>†</sup> As a matter of fact,  $c12 \cdot ref_{sc}(exp)$  may be looked upon as a temperature dependent (expansion dependent) value of  $c12$ .

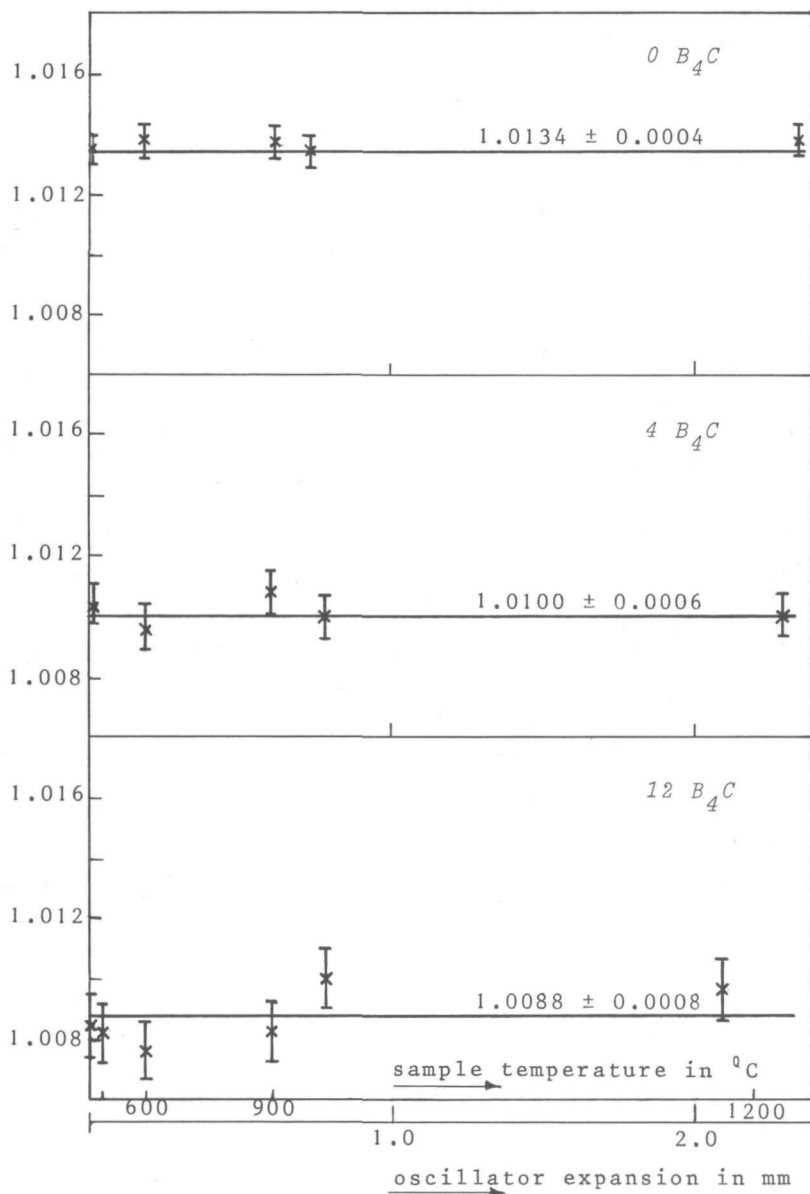


Fig. 3.15 The reference correction for neutrons in the beam direction

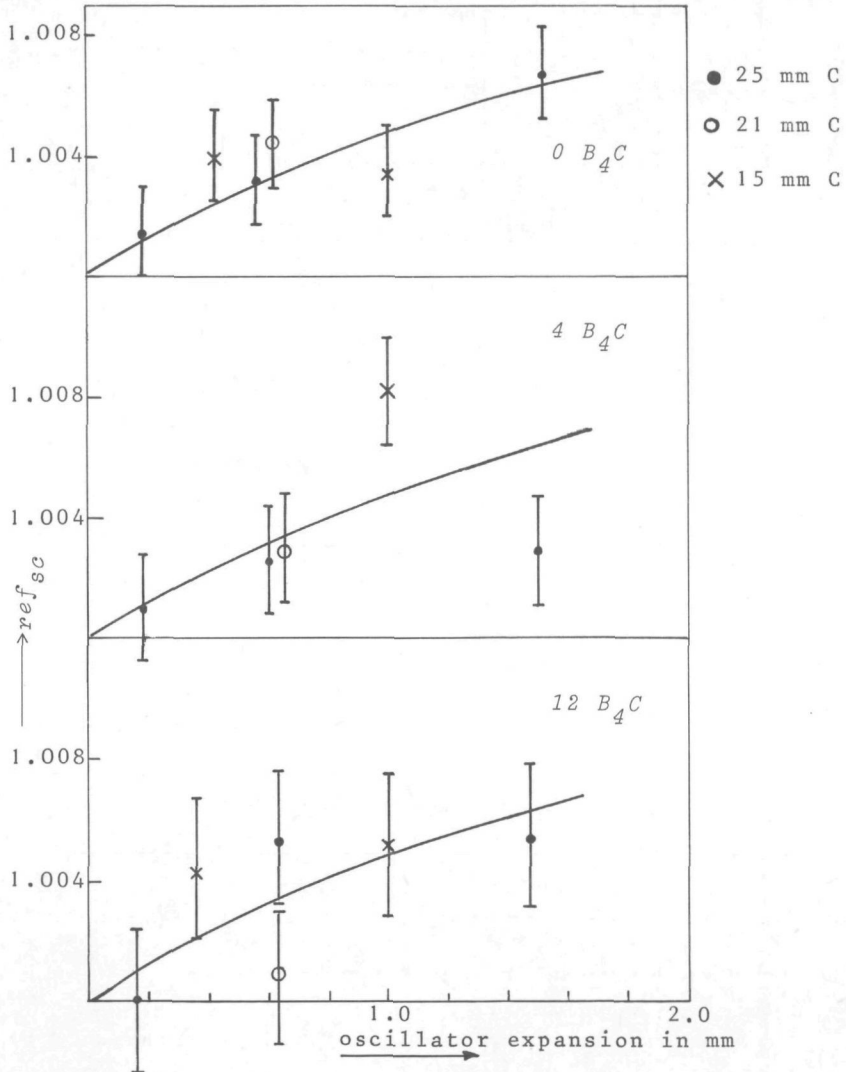


Fig. 3.16 The additional reference correction for the scattered neutrons

spectrum	<i>bicratio</i>	statistical error %
0 $B_4C$	1.7151	0.05
4 $B_4C$	1.7493	0.07
12 $B_4C$	1.7952	0.10

Table 3.5  
The *bicratio* values corresponding to the standard neutron spectra

The results are shown in Fig. 3.15. The expansion (temperature) dependence of  $ref_b$  turns out to be so weak that  $ref_b(exp)$  can be kept constant without grave errors.

The relation between the total oscillator expansion and the sample temperature depends on the air cooling which is applied to the inner surface of the oscillator tube. The temperature values on the abscissa of Fig. 3.15 correspond with the normal performance of the equipment in the measurements of chapter 5.

The temperature dependent additional reference factor for the scattered neutrons has been measured with several graphite samples in the west side oven. After measurement of  $W_{sc}$  and  $R_{sc}$  without  $Bi-C$  scatterer,  $scfr$  is found from (3.23). With  $abs = 0$  and using *mod.c12* from Fig. 3.14,  $ref_{sc}(exp)$  can be found from (3.22):

$$ref_{sc}(exp) = \frac{R_{abs} \cdot (1 + scfr) - W_{abs} \cdot ref_b}{R_{abs} \cdot scfr \cdot mod.c12} \quad (3.25)$$

The results are shown in Fig. 3.16.

Because of the fixed point at  $ref_{sc}(exp=0) = 1.000$ , the inaccuracy of  $ref_{sc}$  decreases with decreasing  $exp$  and is of the order of 0.002 at  $exp = 1.5$  mm.

### 3.7. *Secondary neutron absorption*

#### 3.7.1. *General*

Up to here the tacit assumption has been made that neutrons, after leaving the sample do not reenter it.

With the Monte Carlo computer code MCLAAG (see sec. 4.2.) the number and the spectrum of the neutrons reentering the sample after one or more collisions in the graphite shell have been calculated.

Although the geometrical probability of hitting the sample from any point of the graphite shell is smaller than 1%, the joint probability of the secondary neutrons hitting the sample turns out to be 2.4-4.8% for sample thicknesses varying from 1 to 20 mm.

In Fig. 3.17 the primary and secondary neutron spectra incident to the sample are shown.

Owing to the much slower secondary neutron spectrum and the rather great probability of secondary neutrons hitting the sample, the effect of the secondary neutron absorption may not be neglected.

For the Doppler measurements it is important to distinguish between secondary neutron absorption inside and outside the resonance region, as only the secondary neutron absorption in the resonance region will contribute to the Doppler effect.

In sec. 3.7.2. the total secondary absorption of the  $\text{UO}_2$  and  $\text{ThO}_2$  samples of chapter 5 will be measured, while the resonance region contribution will be calculated separately.

The measurements of chapter 5 will be corrected only for the "cold" secondary neutron absorption. As a consequence, the resulting Doppler effect will be somewhat too high. See also sec. 5.3.

#### 3.7.2. *Measurement of the secondary neutron absorption*

To be able to measure the secondary neutron absorption, a special frame has been constructed in the open sample holder (the sample oven can be replaced by an open sample holder) in which it is possible to

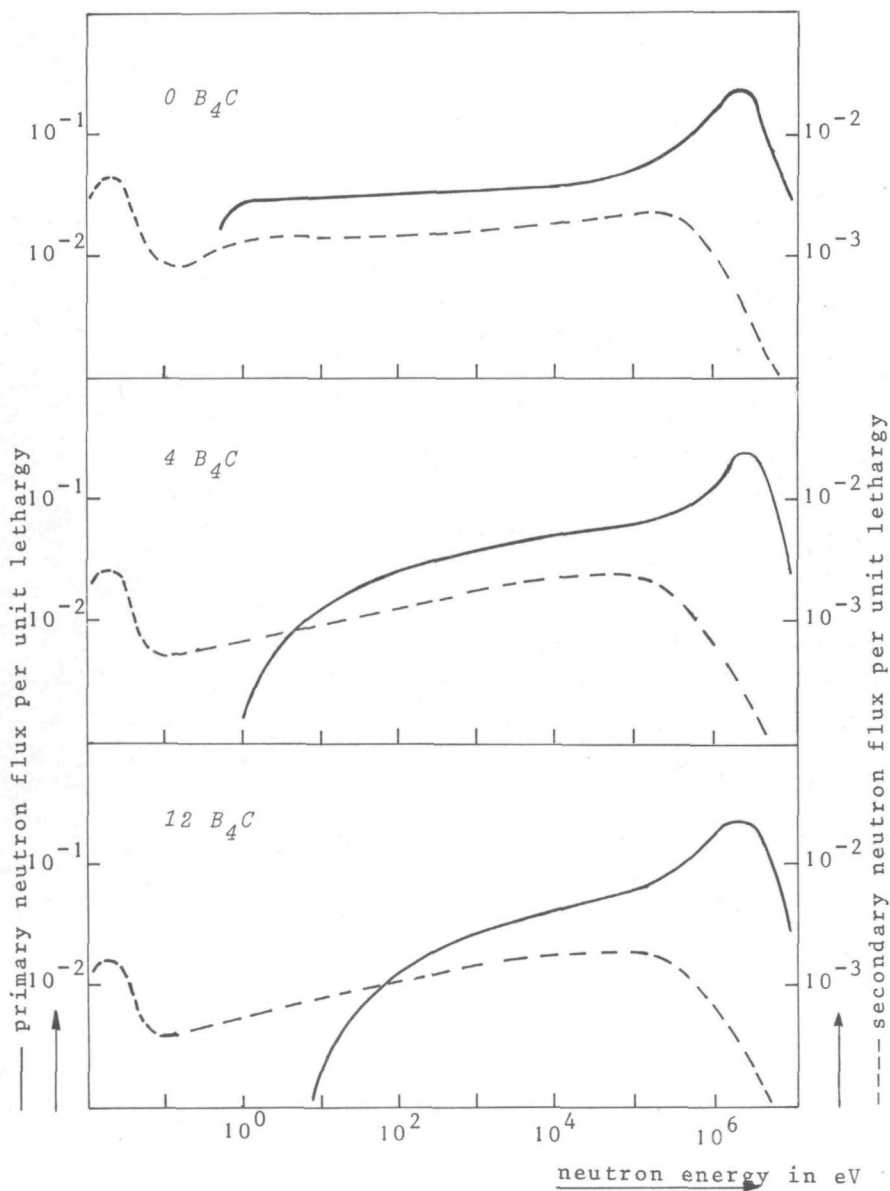


Fig. 3.17 Primary and secondary neutron spectra incident on the sample

mount two target samples at a time. The primary sample is held in the usual central position. The secondary sample is positioned at the west side of the primary sample, outside the primary neutron beam. The secondary sample only contributes to the absorption signal by means of secondary neutron absorption. Thus, using two identical samples, the secondary neutron absorption can be found from the difference between the absorption signals with and without the secondary sample.

Neglecting the neutron shielding from each other and the influence of neutrons directly hitting the secondary sample after scattering from the primary sample, the secondary neutron absorption signals of the  $\text{UO}_2$  and  $\text{ThO}_2$  samples of chapter 5 have been measured. The results are shown in Fig. 3.18.

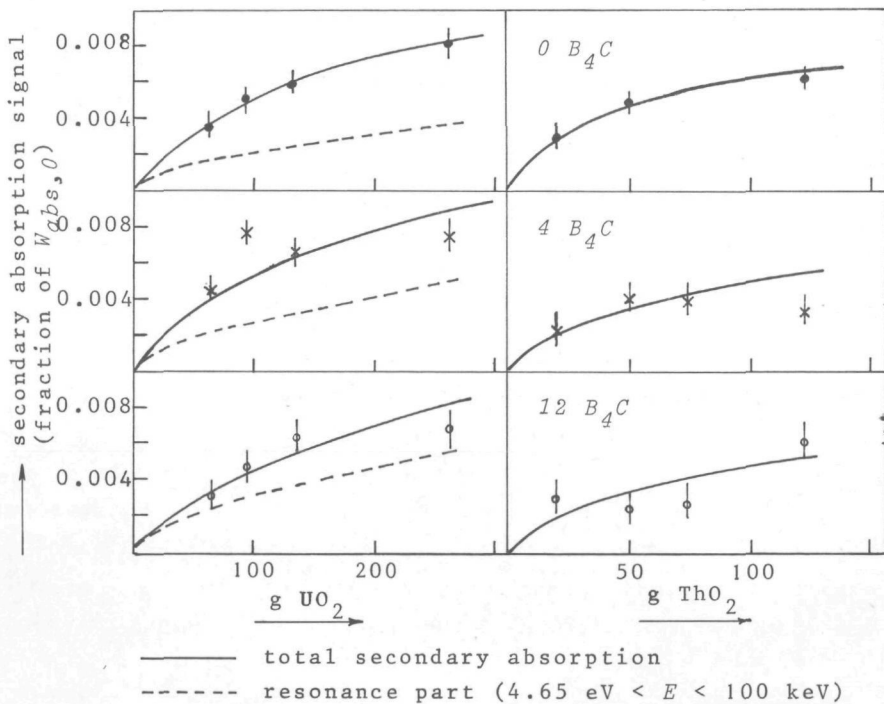


Fig. 3.18 The secondary neutron absorption signal of the  $\text{UO}_2$  and the  $\text{ThO}_2$  samples as a fraction of the empty holder detector signal  $W_{abs,0}$

To get an impression of the resonance part of the secondary absorption signals, calculations of the contribution of the secondary resonance absorption of the  $\text{UO}_2$  samples have been made using the Monte Carlo computer code MCTRANS with changed source routine (see sec. 4.4.). The results are also shown in Fig. 3.18.

The measurements of chapter 5 will not be corrected for the secondary part of the Doppler effect. A possibility of correcting for the secondary part of the Doppler effect would be the construction of an oven with a double sample holder and carrying out two series of measurements, one with and one without secondary sample. A much more attractive way to get rid of the secondary neutron absorption would be to so reduce the ratio of the sample size to the ball diameter that the effect could be neglected. See also chapter 6.

### 3.8. *The thermal expansion of the target sample*

When heating the oven, the molecule density of the sample decreases owing to its thermal expansion. Both neutron absorption and neutron scattering in the target sample will decrease as well, which may influence the Doppler effect to be measured.

The change in the number of neutrons scattered in the sample is found at each temperature by the separate measurement of *scfr*. No special corrections need to be applied.

With  $n(T)$  as the temperature dependent molecule density of the target sample and  $\sigma_t(E,T)$  and  $\sigma_{abs}(E,T)$  as the temperature dependent neutron total and absorption cross-section at energy  $E$  respectively, the probability density of an absorption interaction in the sample of a neutron with energy  $E$ , flying in any direction with coordinate  $x$ , is:

$$n(T) \cdot \sigma_{abs}(E,T) e^{-n(T) \cdot \sigma_t(E,T) \cdot x} \quad (3.26)$$

With a maximum available track length  $L$  in the sample, the integral probability of an absorption interaction is:

$$\int_0^L n(T) \cdot \sigma_{abs}(E, T) e^{-n(T) \cdot \sigma_t(E, T) \cdot x} dx \quad (3.27)$$

Assuming an isotropic expansion, with linear expansion coefficient  $\alpha$ , the molecule density at temperature  $T_1$  can be found from  $n(T_0)$ :

$$n(T_1) = \frac{n(T_0)}{(1 + \alpha\Delta T)^3} \quad (3.28)$$

with  $\Delta T = T_1 - T_0$  ( $T_1 \geq T_0$ )

The maximum available track length after expansion, at temperature  $T_1$ , is  $L(1+\alpha\Delta T)$  and the integral probability of an absorption interaction becomes:

$$\int_0^{L(1+\alpha\Delta T)} \frac{n(T_0)}{(1 + \alpha\Delta T)^3} \sigma_{abs}(E, T_1) e^{-\frac{n(T_0)}{(1 + \alpha\Delta T)^3} \cdot \sigma_t(E, T_1) \cdot x} dx =$$

$$\frac{\sigma_{abs}(E, T_1)}{\sigma_t(E, T_1)} \left[ 1 - e^{-\frac{n(T_0)}{(1 + \alpha\Delta T)^2} \cdot \sigma_t(E, T_1) \cdot L} \right] \quad (3.29)$$

which would be the integral absorption probability in a sample without thermal expansion, but with the same cross-sections and the same dimensions, at a maximum available track length  $L$  and molecule density

$$\frac{n(T_0)}{(1+\alpha\Delta T)^2}$$

Measuring a series of samples with varying sample thicknesses, as will be done with the  $UO_2$  and  $ThO_2$  samples in chapter 5, there is a possibility of correcting graphically for the thermal expansion. In the curve  $abs = f$  (sample mass), the observed values  $abs(T_1)$  are noted down at the sample mass  $\frac{g_0}{(1+\alpha\Delta T)^2}$  in stead of at the true sample mass  $g_0$ . The resulting curve through these points is now corrected for the thermal sample

expansion. The corrected value of the absorption signal,  $C_{exp.abs}$ , at the true sample mass  $g_0$  can be calculated.

$$\text{With } C_{exp.abs} = abs + \Delta abs \quad (3.30)$$

$$\text{and } \Delta abs \approx |\Delta g| \times \frac{dabs}{dg} \quad (3.31)$$

$$\text{and } |\Delta g| = \left[ 1 - \frac{1}{(1 + \alpha \Delta T)^2} \right] \cdot g_0 \quad (3.32)$$

and knowing  $\frac{dabs}{dg}$  from the graph,  $C_{exp}$  can be found:

$$C_{exp} = 1 + \frac{2\alpha \Delta T}{(1 + \alpha \Delta T)^2} \times \frac{g_0}{abs} \times \frac{dabs}{dg} \quad (3.33)$$

The importance of the correction at a given  $\Delta T$  depends on  $\frac{g_0}{abs}$  and  $\frac{dabs}{dg}$ . The strongest effect is found at the  $O B_4 C$  spectrum and the biggest sample.

At  $\Delta T = 1200^\circ C$  and using the expression for the linear expansion of  $UO_2$  (40):

$$\% \text{ expansion} = 2.1481 \times 10^{-7} (\Delta T)^2 + 8.4217 \times 10^{-4} \Delta T + 3.0289 \times 10^{-2} \quad (3.34)$$

$(\Delta T \text{ in } ^\circ C)$

the value of  $C_{exp}$  for the 20-mm  $UO_2$  sample ( $g_0 = 262.67$  g), is:

$$C_{exp} = 1.014 .$$

Owing to this correction the Doppler effect  $D$  (see sec. 3.10.) rises from 0.060 to 0.075. The corresponding values for the 1-mm  $UO_2$  sample ( $g_0 = 14.11$  g) in the  $O B_4 C$  spectrum are :

$C_{exp} = 1.0094$ , and  $D$  rises from 0.358 to 0.371.

The measurements of chapter 5 will be corrected for the thermal expansion effect on the absorption signal. The linear expansion coefficient of  $UO_2$  is found from expression (3.34), while the linear expansion coefficient of  $ThO_2$  will be put to  $9.67 \times 10^{-6} / ^\circ C$  (41).

### 3.9. The sample temperature distribution and position

The temperature distribution of a 6-mm  $\text{Al}_2\text{O}_3$  sample has been measured at several temperatures up to about  $1250^\circ\text{C}$ . Three thermocouples [Pt to Pt(10%Rh)] were attached to the sample as indicated in Fig. 3.19, while a fourth, used as a reference, was fixed at the  $\text{Al}_2\text{O}_3$  sample holder.

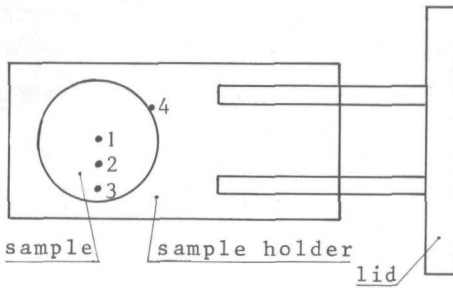


Fig. 3.19

Thermocouple position on the sample in the temperature distribution measurements

From Table 3.6 it appears that the temperature differences over the sample are so small that the temperature in the sample may be considered constant. Less extensive measurements of a 7.5-mm  $\text{UO}_2$  sample have confirmed the flat temperature distribution. In view of the small Doppler induced changes in absorption rate at temperature changes of even  $50^\circ\text{C}$ , the influence of the temperature distribution over the sample will be neglected in the neutron absorption measurements.

Table 3.6  
Temperature distribution over a 6-mm  $\text{Al}_2\text{O}_3$  sample

temp 1 $^\circ\text{C}$	temp 2 $^\circ\text{C}$	temp 3 $^\circ\text{C}$	temp 4 $^\circ\text{C}$
575	550	575	590
920	900	915	940
1095	1070	1080	1190
1245	1220	1235	1375

Table 3.7  
Sample position at  
different temperatures

T °C	$\Delta s$ (mm) $\pm 0.1$ mm	$\Delta l$ mm
20	0	0
800	- 0.5	0.63
1200	- 0.05	1.80

The influence of the sample position upon the detector signal has been measured.

- (a) Even when a 10-mm  $UO_2$  sample was removed 1.5 mm from the centre position in the direction of the oscillator axis, no significant change in the detector signal was perceived with or without  $Bi-C$  scatterer.
- (b) Changing the sample position in the direction of the axis of the neutron beam within the limits of the sample holder caused no perceptible signal change.
- (c) Even a  $2^\circ$  rotation of the sample about the oscillator axis caused no significant signal change, while the normal play of the oscillator tube around its axis is  $< 30'$ .

- (a) The reproducibility of the position of the cold sample has been measured during oscillator operation, and it appeared to be within about 0.01 mm.

The reproducibility of the "cold" position of the sample, after being heated, appeared to be of the order of 0.1 mm.

The sample position was measured at several temperatures, using a  $\gamma$  source and a very narrow line-shaped  $\gamma$  collimator.

In Table 3.7  $\Delta s$  indicates the change of the sample position, while  $\Delta l$  is the observed total expansion of the oscillator tube.  $\Delta l$  and  $\Delta s$  are opposite in direction. The maximum sample displacement of 0.5 mm was perceived at about  $800^\circ C$ .

Conclusion: In the neutron absorption measurements no corrections due to the sample position need to be applied.

### 3.10. Review of the applied correction factors, definitions and relations

After the description of the separate corrections to be applied to the detector signals, it may be useful to give a review of the defined quantities and their relations:

$R_{abs}$  ( $R_{abs}^0$ ) is the detector signal when the east-side sample oven with a 25-mm lead sample and the *Bi-C* scatterer are inside the graphite ball corrected for the insensitive time of the detector and (not) corrected for the background signal.

$W_{abs,o}$  : ditto without a sample.

$W_{sc}$  ( $W_{sc}^0$ ): as  $W_{abs}$  but without *Bi-C* scatterer.

$abs$  expressed as a fraction of  $W_{abs,o}$  is the absorption signal, disappeared owing to neutron absorption in the unknown sample.

$primabs$  ( $primabs_c$  and  $primabs_w$  respectively): ditto owing only to primary neutron absorption in the unknown (cold and warm respectively) sample.

$secabs$ : ditto owing to secondary neutron absorption only.

$D$  is the relative change in the primary absorption signal, caused by the temperature induced nuclear Doppler effect.

$bg$  is the fraction of  $R_{abs}^0$  caused by the background neutrons from outside the detector and scattered from the neutron beam on all the matter in front of the sample.

$wac$  expressed as a fraction of  $R_{abs}$  is the portion of the signal caused by background neutron scattering from the beam on all the matter behind the sample holder, without a sample in the ball and the *Bi-C* scatterer being removed.

$scfr$  expressed as a fraction of  $W_{abs,o}$  is the fraction of the signal caused by neutrons scattered from the sample.

$c12$  is the correction to be applied to  $scfr$ , necessitated by the influence of the holes in the graphite ball and by the deviation from the correct position of the dodecahedron and the  $BF_3$  tubes.

$emod$  is the correction to be applied to  $scfr$ , owing to the change in the detector efficiency of the neutrons after being slowed down in the scattering process in the sample.

$$bigratio = \frac{R_{abs}}{R_{sc}}$$

$$ref_b = \frac{R_{abs}}{W_{abs,0}}$$

$ref_{sc}(exp)$  is the additional correction to be applied to  $scfr$  owing to the oscillator expansion  $exp$  and the rise in temperature of the graphite plugs in the oscillator tube around the heated west-side oven.

$Cexp$  is the correction to be applied to the absorption signal, owing to the thermal expansion of the sample.

The following relations are used for the background correction, which is almost independent of the presence of the  $Bi-C$  scatterer and the difference between the east-side and the west-side oven:

$$R_{abs} = R_{abs}^o (1 - bg) \quad (3.35)$$

$$R_{sc} = R_{sc}^o - bg \cdot R_{abs}^o \quad (3.36)$$

$$W_{abs} = W_{abs}^o - bg \cdot R_{abs}^o \quad (3.37)$$

$$W_{sc} = W_{sc}^o - bg \cdot R_{abs}^o \quad (3.38)$$

The signals  $R_{abs}$  and  $R_{sc}$  (i.e. when the east-side oven is in the ball) are used as reference signals. The relations between the east-side and the west-side signals are:

$$W_{abs} = \left( 1 - abs + scfr\{1-cmod.c12.ref_{sc}(exp)\} \right) \frac{R_{abs}}{ref_b} \quad (3.39)$$

and

$$W_{sc} = \left( \frac{scfr}{ref_b} + \{1 - abs - cmod.c12.ref_{sc}(exp).scfr\}wac \right) .bigratio.R_{sc} \quad (3.40)$$

The absorption signal  $abs$  can be found from (3.39):

$$abs = \frac{R_{abs} - ref_b \cdot W_{abs} + scfr\{1-cmod.c12.ref_{sc}(exp)\}R_{abs}}{R_{abs}} \quad (3.41)$$

The scattered fraction signal  $scfr$  can be found from (3.40):

$$scfr = \frac{W_{sc} - (1-abs).wac.bicratio.R_{sc}}{\left\{\frac{1}{ref_b} - cmod.c12.ref_{sc}(exp).wac\right\}.bicratio.R_{sc}} \quad (3.42)$$

The secondary absorption signal  $secabs$  is found from separate measurements and the primary absorption signal  $primabs$  is now:

$$primabs = abs - secabs \quad (3.43)$$

After measuring the hot and cold absorption signals, the nuclear Doppler effect  $D$  is found from:

$$D = \frac{Cexp.primabs_w - primabs_c}{primabs_c} \quad (3.44)$$

No correction is applied to  $D$  for the temperature dependent part of  $secabs$ .

No correction is applied to  $scfr$  for the hole of the  $Bi-C$  scatterer.

## 4. THE CALCULATION PROGRAMS

### 4.1. Introduction

To verify well-known sample measurements of the graphite ball detector on the one hand, and to be able to evaluate unknown sample measurements on the other, calculations have been made. A detector counting result, or detector integral,  $DI$  may be represented by

$$DI = \int \Phi(E) \cdot tr(\mathcal{L}, \Sigma(E)) \cdot eff(E) dE \quad (4.1)$$

$\Phi(E)$  is the total amount of neutrons per unit energy incident to the sample.

$tr(\mathcal{L}, \Sigma(E))$  is the transmission function of the sample with thickness  $\mathcal{L}$  and macroscopic cross-section  $\Sigma(E)$ .

$eff(E)$  is the mean detector efficiency for neutrons with energy  $E$ . After calculation of  $\Phi(E)$ ,  $eff(E)$  and  $tr(\mathcal{L}, \Sigma(E))$  of a well-known sample, a check on  $DI$  can be made. When, however,  $\Phi(E)$  and  $eff(E)$  are known by calculation, and  $DI$  is a reliable measurement result, the mean value of  $tr(\mathcal{L}, \Sigma(E))$ , and hence a mean value of  $\Sigma(E)$  of an unknown sample can be determined. Solving  $\Sigma(E)$  from  $tr(\mathcal{L}, \Sigma(E))$ , however, is beyond the scope of this work.

This chapter gives a review of the programs and models used to calculate  $\Phi(E)$ ,  $tr(\mathcal{L}, \Sigma(E))$  and  $eff(E)$ , starting from literature cross-section data.

For the practical performance of the calculations formula (4.1) has been approached by the discrete representation:

$$DI = \sum_g \Phi_g \cdot tr(\mathcal{L}, \Sigma_g) \cdot eff_g \cdot \Delta E_g \quad (4.2)$$

where  $\Phi_g$ ,  $\Sigma_g$  and  $eff_g$  are the constant values of  $\Phi(E)$ ,  $\Sigma(E)$  and  $eff(E)$  on the energy interval  $\Delta E_g$ , with  $g$  as the index of the group number.

Section 4.2. gives the calculation of the mean detector efficiency  $eff_g$ , for the different energy groups. The computer codes MCLAAG, TREFKANS and MCBUIS have been designed especially for this purpose. Section 4.3. shows the calculation models of the programs used to determine the different neutron spectra. The computer code FAST ZOOM DELFT for the calculation of the neutron spectrum in the ATHENE 2-core system has been copied from existing work. Special attention is requested for the computer program MCREVERSE for the calculation of the neutron spectra resulting from the filter system and the neutron collimator. A new technique is introduced, which may be indicated as "backward Monte Carlo game", the theory of which is to be found in the Appendix.

Section 4.4. gives the model and the special features of MCTRANS, which is a computer code especially designed to calculate the transmission  $tr(l, \Sigma_g)$  and other properties of the sample.

#### 4.2. The detector efficiency

The mean detector efficiency  $eff_g$  for the neutrons with energy  $E_g$  incident to the inner wall of the graphite ball, is found by calculating the mean probability of being detected by the 20  $BF_3$  detectors, which are mounted around the ball.

When designing the calculations, the possibility of a polyethylene socket with variable wall thickness around each of the  $BF_3$  tubes was included. The sockets provide the possibility of an easy variation of the detector efficiency function. The experiments with the sockets are not yet finished and so will not be mentioned in the following. The calculation scheme, however, takes account of the possibility. Therefore the calculations have been divided into two main programs MCLAAG and MCBUIS and an auxiliary program TREFKANS. See Fig. 4.1.

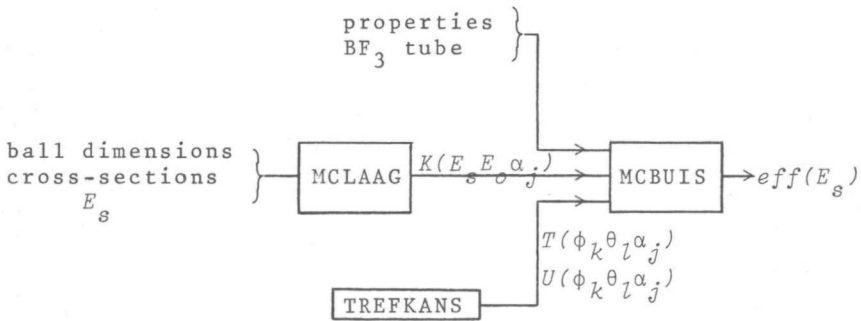


Fig. 4.1 Calculation scheme of detector efficiency

MCLAAG describes the neutron transport in the graphite ball.

TREFKANS determines the probability of hitting a  $BF_3$  tube of a neutron leaving the graphite ball. MCBUIS calculates the detection probability of a neutron hitting a  $BF_3$  tube.

To solve the neutron transport equation, the programs MCLAAG and MCBUIS utilize the standard Monte Carlo technique, as described by Cashwell (42) and Spanier (43). Both programs take account of neutron absorption and elastic scattering reactions. The collision kernel is based on the principle of isotropy in the centre-of-mass system for

all energy groups, except for the thermal group, in which isotropy in the laboratory system is used. The techniques of "particle splitting" and "Russian roulette" are used to improve the speed of variance reduction.

The Monte Carlo computer code MCLAAG describes the neutron transport in the graphite ball. The model of the ball is simplified by neglecting the holes of the beam entrance and the oscillator passage.

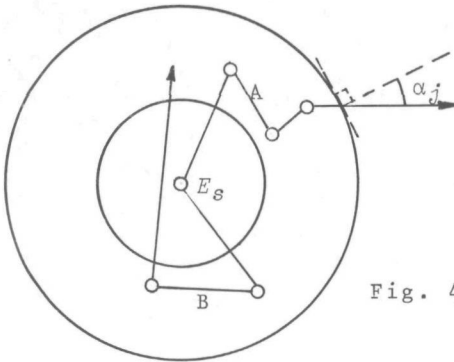


Fig. 4.2 The calculation model of the graphite ball in MCLAAG

See Fig. 4.2. The Monte Carlo neutrons are started from the centre of the ball, in energy group  $s$ , with energy  $E_s$ . By repeated selection of neutron tracks, like A (see Fig. 4.2), MCLAAG determines the distribution of the energies  $E_o (\leq E_s)$  and the directions  $\alpha_j$  of the neutrons leaving the ball. The output is recorded in the three-dimensional array  $K(E_s, E_o, \alpha_j)$ . In most calculations  $E_s$  and  $E_o$  are discretized in the 26-group ABBN set (44) and  $\alpha_j$  is discretized by the relation of the lower limits of the groups of solid angle:

$$\frac{\cos \alpha_j + (1 - \sin \alpha_j)}{2} = 1 - \frac{j}{j_{max}} \quad (4.3)$$

where  $j_{max}$  is the total number of groups of solid angle.

If requested, MCLAAG also furnishes the two dimensional array  $K(E_s, E_{2c})$ , which gives the probabilities of the neutrons reentering the sample at energy  $E_{2c} (\leq E_s)$  after being started from the centre of the ball with energy  $E_s$  and after being scattered once or more times in the graphite, like track B in Fig. 4.2. The neutrons

reentering the sample from the graphite are called the 'secondary neutrons'. See also sec. 3.7.

The computer code TREFKANS gives the probability of hitting a  $\text{BF}_3$  tube of a neutron leaving the graphite ball. TREFKANS uses a network of meshes on the surface of the graphite ball, each of which is determined by the angle coordinates  $\phi_k$  and  $\theta_l$  for mesh  $(k, l)$ . See Fig. 4.3.

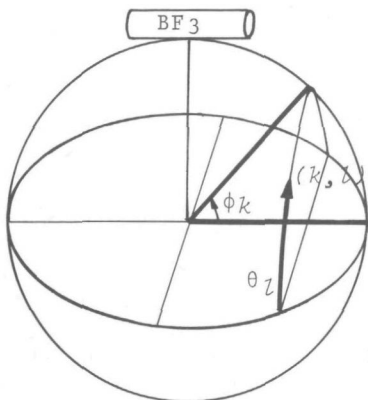


Fig. 4.3 The calculation model of TREFKANS

The output of TREFKANS consists of the three-dimensional arrays  $T(\phi_k, \theta_l, \alpha_j)$  and  $U(\phi_k, \theta_l, \alpha_j)$ . The elements of  $T$  give the probability of hitting a  $\text{BF}_3$  tube, fixed at  $\phi = \theta = \frac{\pi}{2}$ , of a neutron which has left the ball at mesh  $(k, l)$  with  $\alpha_j$  (see MCLAAG) as the angle of departure from the surface of the ball. The elements of  $U$  are the corresponding limits of the azimuth for a neutron to hit the  $\text{BF}_3$  tube.

The mean probability  $\bar{T}(\alpha_j)$  of hitting the  $\text{BF}_3$  tube of any neutron leaving the ball at the angle of departure  $\alpha_j$ , is found from:

$$\bar{T}(\alpha_j) = \frac{1}{K \cdot L} \sum_l \sum_k T(\phi_k, \theta_l, \alpha_j) \quad (4.4)$$

where  $K$  and  $L$  are the total number of meshes in the direction of  $\phi$  and  $\theta$  respectively.

The surface areas of all meshes have been chosen equal and the number of meshes has been so chosen ( $K = 20$ ,  $L = 40$  on an octant of the ball) that  $\bar{T}(\alpha_j)$  varies less than 1% at a further increase of  $K$  and  $L$ .

The Monte Carlo computer code MCBUIS calculates the detection probability of a neutron hitting the  $\text{BF}_3$  tube.

The input of MCBUIS consists of the physical properties of the  $\text{BF}_3$  tube and the output arrays  $K(E_s, E_o, \alpha_j)$  of MCLAAG and  $T(\phi_k, \theta_l, \alpha_j)$  and  $U(\phi_k, \theta_l, \alpha_j)$  of TREFKANS. To calculate  $eff(E_s)$ , the starting energy  $E_o$  and the angle of departure from the surface of the ball  $\alpha_j$  are selected from the distribution of the two-dimensional section of  $K(E_s, E_o, \alpha_j)$  in the case of the fixed group of interest  $s$ . The mesh of departure is now selected from the normalized distribution  $T(\phi_k, \theta_l, \alpha_j)/(K.L.\bar{T}(\alpha_j))$  and the corresponding azimuth to hit the  $\text{BF}_3$  tube is found from  $U(\phi_k, \theta_l, \alpha_j)$ .

Finally,  $eff(E_s)$  for the 20  $\text{BF}_3$  tubes together is found from:

$$eff(E_s) = \sum_l \sum_k \sum_j \sum_o K(E_s, E_o, \alpha_j) \cdot \frac{T(\phi_k, \theta_l, \alpha_j)}{K.L.\bar{T}(\alpha_j)} \cdot D(E_o, \alpha_j, \phi_k, \theta_l) \times 20 \quad (4.5)$$

where  $D(E_o, \alpha_j, \phi_k, \theta_l)$  is the mean detection efficiency for neutrons leaving the surface of the ball under the conditions  $E_o, \alpha_j, \phi_k, \theta_l$ .

The detector efficiency has been calculated in the 26-group ABBN cross-section set (44). The results are shown in Fig. 4.4. See also Fig. 2.6 for the comparison of  $eff(E_s)$  for different ball diameters.

The accuracy of the joint calculations of the detector efficiency has been estimated by repeating the calculations with different random generators in the Monte Carlo programs. The estimated statistical errors of the individual group values are indicated in Fig. 4.4.

To check the influence of cross-section errors on the calculated detector efficiency, the cross-sections of the graphite have all been multiplied by 1.04. The calculation results are shown in Fig. 4.4. To be able to evaluate these calculations, some remarks of Schmidt (45) concerning the total cross-section of graphite are quoted:

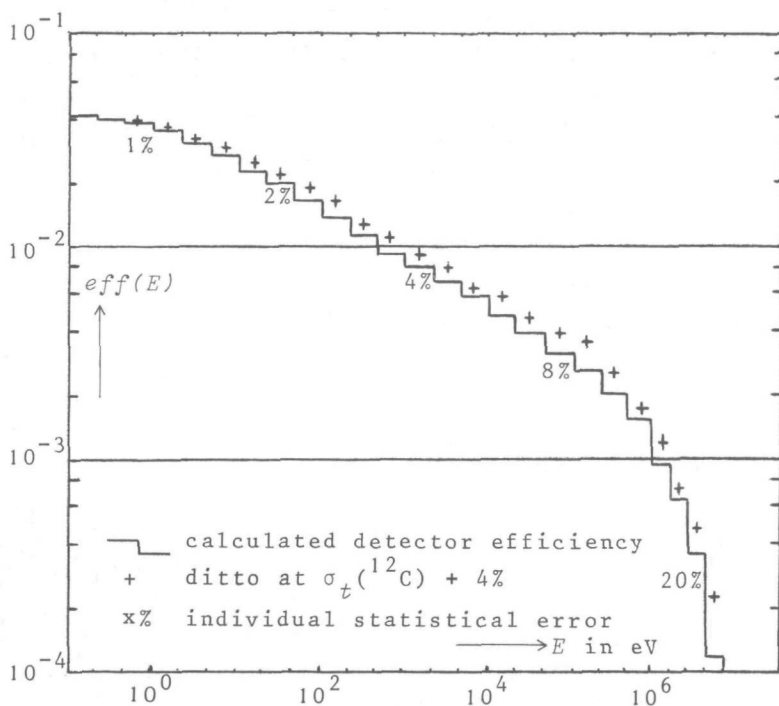


Fig. 4.4 The calculated efficiency of the graphite ball detector

- "The recommended  $\sigma_t$  (thermal) value of 4.71 b may, at worst, be a few % too small".
- "The overall accuracy of the recommended  $\sigma_t$  values below 1.4 MeV is estimated to be between  $\pm 5\%$  and  $\pm 10\%$ ".

Owing to the influence of the holes in the ball, the real overall mean detector efficiency will be 5 to 10% lower than the calculated value, depending on the neutron spectrum (see sec. 3.5.2.).

For further error discussion see sec. 5.3.

### 4.3. Calculations of the neutron spectra

#### 4.3.1. Introduction

For the purpose of valuable calculations of the detector integrals,

as represented by formula (4.1), in the case of resonance absorption samples, like  $\text{UO}_2$  and  $\text{ThO}_2$ , the neutron spectrum should satisfy the following conditions:

- The gradient of the spectrum in the resonance area ( $3 \text{ eV} < E < 50 \text{ keV}$ ) should be known.
- There should be neither coincidence nor overlap of flux dips or flux peaks with the resonance peaks of the sample material.

The gradient of the reactor spectrum has been calculated by means of the computer code FAST ZOOM DELFT, which is based on one-dimensional neutron diffusion theory. See sec. 4.3.2. An experimental check on the calculations of FAST ZOOM DELFT has been made with proton recoil measurements of the high-energy range and a series of  $\text{B}_4\text{C}$  measurements of the lower energy range. See sec. 5.1. The gradients of the  $\text{B}_4\text{C}$ -filtered collimator beam spectra have been calculated with the specially designed "backward Monte Carlo" program MCREVERSE (sec. 4.3.3.), the theory of which is given in the Appendix. No experimental check has been carried out on the gradients of the filtered spectra.

As for coincidence and overlap of flux peaks or dips with resonance peaks of the sample, no special calculations or measurements have been carried out, as they are very complicated and too far beyond the scope of this work. However, the assumption of the absence of coincidence or overlap is reasonable on account of the following arguments.

- Each neutron of the collimator beam has been scattered once at least, which smooths down possible spectral irregularities.
- The ATHENE fissile fuel is composed of 95%-enriched  $^{235}\text{U}$  and about 5%  $^{238}\text{U}$ , so the influence of  $^{238}\text{U}$  resonance is rather limited in this case.
- Accidental overlap is not very likely, as the widths of the resonance peaks is only of the order of tenths eV.

#### 4.3.2. The neutron spectrum in the ATHENE 2-core system

The computer code FAST ZOOM DELFT utilizes one dimensional, multi-group neutron diffusion theory and is described by Van Dam (46). Fig. 4.5a gives a schematic view of the real ATHENE-core configuration. It is composed of two water-filled core boxes, each of which contains 6 MTR type fuel elements. Between the two core boxes there is an air chamber, and a graphite reflector is mounted around the boxes. In view of the central position of the neutron scatterer in the reactor core, the neutron spectrum in the centre of the two boxes has been calculated. Because FAST ZOOM DELFT is a one-dimensional code, the model of the reactor has been made cylindrical. See Fig. 4.5b.

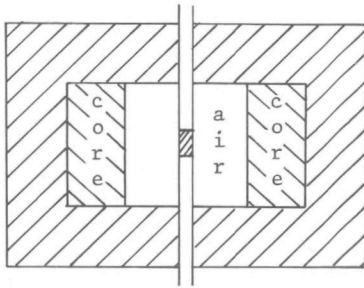


Fig. 4.5a The ATHENE core configuration

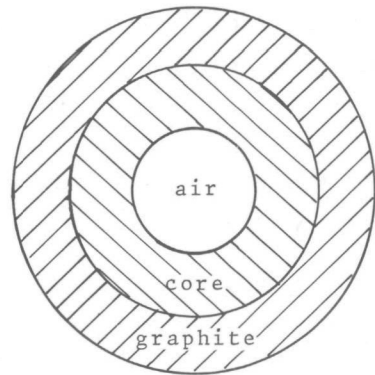


Fig. 4.5b The ATHENE core calculation model

The cylindrical model has been divided into 5 cylindrical zones.

- (1) air
- (2) the inner aluminium wall of the core box
- (3) a homogeneous mixture in the right proportions of  $^{235}\text{U}$ ,  $^{238}\text{U}$ , Al,  $\text{H}_2\text{O}$  in the core boxes
- (4) the outer aluminium wall of the core box
- (5) the graphite reflector

The calculation results are presented in the 26-group ABBN set distribution. See Fig. 5.1.

As for the accuracy of the diffusion theory neutron spectra, it can be stated (47) that the calculated spectrum near (within a few mean free paths) an external source, turns out too soft and farther from the source it turns out too fast. In the case of the ATHENE core, the mean distance from the core to the neutron scatterer is of the order of a few mean free paths. So the ratio of fast ( $> 1$  MeV) to slow ( $< 1$  MeV) neutrons will be accepted to be the right one. The gradient of the low-energy tail ( $< 50$  keV) can be accepted to be rather accurate, as there are no strong absorbers or important material boundaries near the centre of the core.

4.3.3. MCREVERSE. *A backward Monte Carlo program for the calculation of the filtered neutron beam spectra*

To calculate the neutron spectrum in the collimator resulting from a known reactor spectrum and a composite neutron filter, the transmission of the filter has to be calculated as a function of neutron energy.

An obvious way to solve the transmission problem is a Monte Carlo calculation of the neutron transport through the filter tube. See Fig. 4.6. Using a normal forward Monte Carlo integration of the

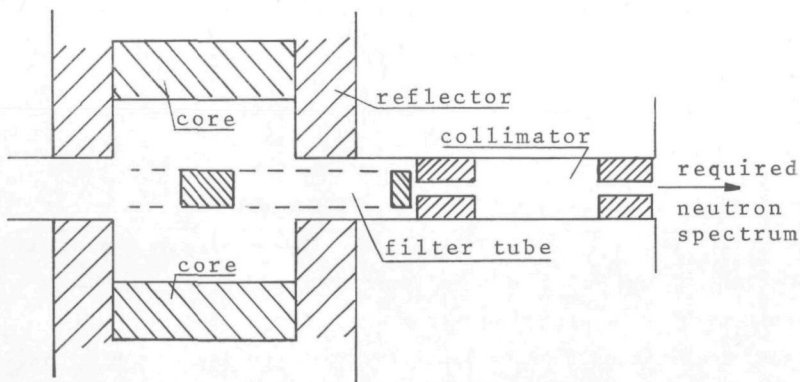


Fig. 4.6 The calculation model in MCREVERSE

neutron transport equation, the variance of the transmission probability to be calculated will decrease very slowly, owing to the very slight geometrical probability of leaving the filter via the collimator opening.

To avoid this slight probability, a new technique of selecting possible neutron tracks will be introduced, starting from the end of the track and choosing backwards possible points of origin of the neutron.

Using Bayes's rule for the probability of causes, it will be shown that the probability density of finding in phase point  $B$  of the source the origin of a neutron, perceived in phase point  $A$  of the target is equal to the probability density of the forward transition from  $B$  to  $A$ . Just as it is possible to derive the standard forward Monte Carlo transport and collision kernels, starting from a physical point of view, so it is possible to derive backward transport and collision kernels, from which previous neutron events can be selected. As a result it will turn out, that the backward kernels are the same as the kernels to be used in a Monte Carlo integration of the adjoint neutron transport equation. See the Appendix.

The unknown forward transition probability will be found from the backward Monte Carlo program. Using MCREVERSE, the reactor can be divided into three neutron source areas: (1) the reactor core boxes, (2) the reflector, (3) the beam holes. With the spectra and the relative strengths of the source areas given, it is possible to find the unknown collimator beam spectrum.

The calculation results of MCREVERSE for the  ${}^4B_4C$  and the  ${}^{12}B_4C$  filters, carried out with the 26-group ABBN cross-section set (44), are shown in Fig. 2.5: the middle and the lower curve respectively. The accuracy of the calculated filtered spectra is determined by the accuracy of the reactor spectrum (see sec. 4.3.2.) and the accuracy of the transition probability. The accuracy of the transition probability is determined by the statistical error (which has been put at 5% standard deviation for each group element) and the errors due to the approximation of the reactor model.

The influence of these errors on the gradient of the curve through the calculated group values is estimated to be rather small. Moreover, the influence of the spectrum upon the absorption and Doppler values is not very strong (see sec. 5.2.). Therefore the calculated values of the neutron spectra will be accepted to be correct.

#### 4.4. MCTRANS. Calculations of the sample properties

MCTRANS is a Monte Carlo program for the calculation of single, disk-shaped, sample properties. Therefore the geometrical calculation model is a simple disk. See Fig. 4.7. The input-output scheme is shown in Fig. 4.8.

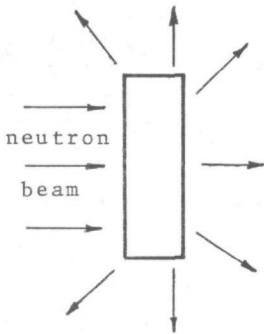


Fig. 4.7 The calculation model of MCTRANS

The source neutrons are selected from a parallel beam, incident to one side of the disk. Except for absorption and elastic scattering, the program also takes into account fission and inelastic scattering properties.

With MCTRANS it is possible to calculate several samples at a time,

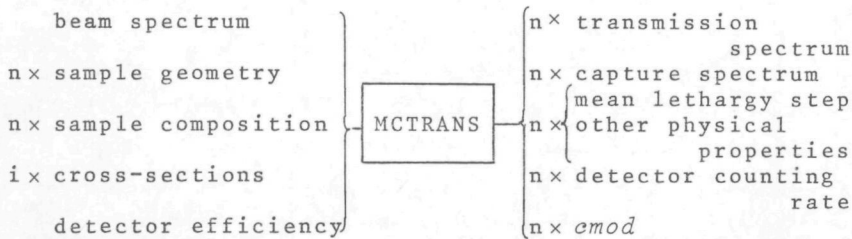


Fig. 4.8 Input-output scheme of MCTRANS

in such a way that each neutron is shot to each of the samples with the same start parameters and the same position of the random generator of the Monte Carlo mechanism. Owing to this feature the program is very efficient in parameter studies.

The input of either group cross-sections or point cross-sections for the different isotopes enables the program to deal with resonance absorbers as well as more simple materials.

The accuracy of the transmission spectra and the detector signals is determined mainly by the accuracy of the input cross-section data. The error due to statistics can be made smaller than 0.1% in acceptable computing time.

One of the most important quantities to be calculated by MCTRANS is the correction of the measurements for the slowing-down effect in the target sample,  $\epsilon_{mod}$ . See sec. 3.5. Supposing  $\epsilon_{12} = 1$ ,  $\epsilon_{mod}$  is defined by formula (3.13) as:

$$\epsilon_{mod} = \frac{\int_0^{\infty} \Phi_0(E) \left[ 1 - t(E) - abs(E) \right] \cdot eff(E) dE}{\int_0^{\infty} \Phi_0(E) \left[ 1 - t(E) - abs(E) \right] \cdot mod(E) \cdot eff(E) dE} \quad (4.6)$$

or in words

$$\frac{\text{signal of scattered neutrons without energy change}}{\text{signal of scattered neutrons with energy change}}$$

The numerator of formula (4.6) can be found with MCTRANS by storing the weight of the scattered particles, after leaving the sample, in an array with indication of the starting energy. The denominator of formula (4.6) can be found by storing the same particles with indication of their leaving energy. However, to prevent systematic errors due to the group structure of  $eff(E)$ , it is more advisable to calculate the denominator of formula (4.6) by storing the lethargy step between starting and leaving energy of the particles. For each starting energy group  $g$  an apparent efficiency value  $eff_g^m$  be defined by :

$$eff_g^m = \frac{\int_g \Phi_0(E) \left[ 1-t(E)-abs(E) \right]_{mod(E)} \cdot eff(E) dE}{\int_g \Phi_0(E) \left[ 1-t(E)-abs(E) \right] \cdot dE} \quad (4.7)$$

$eff_g^m$  can be found from the logarithmic interpolation between the efficiency group values  $eff_g$  of Fig. 4.4:

$$\ln eff_g^m = \ln eff_g + \frac{(\overline{\Delta \ln E})_g}{\ln E_{g+1} - \ln E_g} \times (\ln eff_{g+1} - \ln eff_g) \quad (4.8)$$

(in the case of  $|\overline{\Delta \ln E}_g| < |\ln E_{g+1} - \ln E_g|$ )

where  $E_g$  is the mean energy of group  $g$ , and  $(\overline{\Delta \ln E})_g$  is the mean lethargy step of the scattered neutrons in starting group  $g$ .

Approaching the integrals of formula (4.6) by the sums over all energy groups, with indication  $g$ ,  $emod$  can be found from:

$$emod = \frac{\sum_g \Phi_{0g} \cdot \left[ 1-t-abs \right]_g \cdot eff_g}{\sum_g \Phi_{0g} \left[ 1-t-abs \right]_g \cdot eff_g^m} \quad (4.9)$$

where  $\Phi_{0g}$  is the group flux of group  $g$ .

The accuracy of the interpolation is good in the range of 1 eV to 100 keV, since the efficiency curve on the bilogarithmic scale of Fig. 4.4 is almost a straight line on this interval. The error in  $emod$  due to statistics and interpolation is estimated to be  $< 0.2\%$ , and may be neglected with respect to the inaccuracy due to the uncertainty of the inelastic scattering cross-sections in the case of the  $UO_2$  and  $ThO_2$  calculations. See also sec. 3.5.5.

## 5. EXPERIMENTAL RESULTS AND COMPARISON WITH CALCULATIONS

### 5.1. The neutron spectrum

Two measuring methods have been used to verify the calculations of the unfiltered neutron beam spectrum.

Utilizing the experience of the "Reactor Centrum Nederland", the spectrum in the energy range between 30 keV and 1 MeV has been measured by Montizaan (48) by means of proton recoil technique. The measurements were carried out with two metal spheres (dia. 40 mm), filled with 4 atm  $H_2$  and 4 atm  $CH_4$  gas respectively. Special provisions were made to avoid deviations from the usual corrections for wall and end-effects which have to be applied to the detector results in the case of a homogeneous neutron field. The results of the measurements have been adapted to the groups of the ABBN set (44). They are shown in Fig. 5.1.

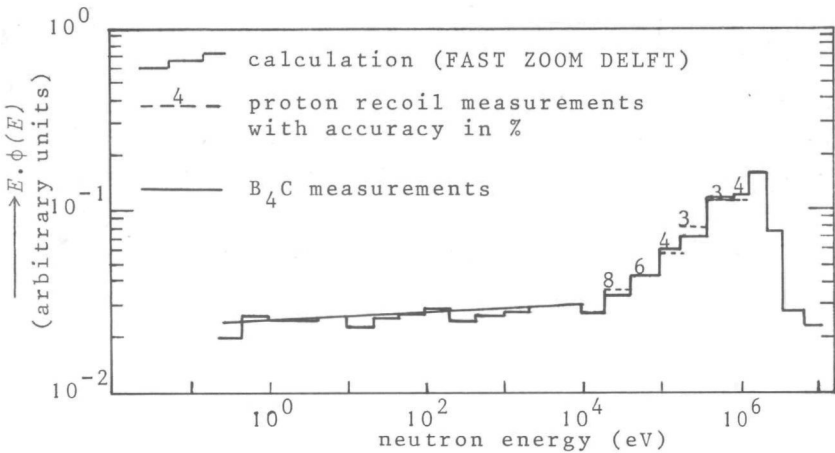


Fig. 5.1 The unfiltered neutron beam spectrum

The accuracy of the measurement values, which is given by Montizaan, including all effects of the measurements and the unfolding technique is also indicated in Fig. 5.1.

For more details of the proton recoil measurements the reader may be referred to the report of Montizaan (48).

In addition to the proton recoil measurements for the higher energy part of the neutron spectrum, the lower energy tail of the spectrum has been tested in the graphite ball detector by comparing the changes of the measured and the calculated detector signals. For this purpose a series of 15 boron carbide samples of various thicknesses was used. Knowing the compositions of the samples and the cross-sections of boron and carbon, a transmission factor  $trf(m,g)$ , for each sample  $m$  and for each energy group  $g$  (of the ABBN set(44)) can be calculated by MCTRANS (see sec. 4.4.). With  $F(g)$  as the total number of neutrons in energy group  $g$ , incident to the sample, and  $eff(g)$  as the mean detector efficiency for neutrons of group  $g$ , and  $f_{tr}^*(m,i)$  as the total number of neutrons resulting from sample  $m$  in energy group  $i$ ,  $trf(m,g)$  is defined by

$$trf(m,g) = \frac{\sum_i f_{tr}^*(m,i) \cdot eff(i)}{F(g) \cdot eff(g)} \quad (5.1)$$

For each sample  $m$ , with  $rl(m)$  as the measured ratio of the detector signal with sample  $m$  and the detector signal without sample, the following equations can be written:

$$\sum_{i=1}^{26} F(i) \cdot eff(i) \cdot trf(m,i) = rl(m) \sum_{i=1}^{26} F(i) \cdot eff(i) \quad (5.2)$$

A system of 15 equations arises from the series of 15 different sample measurements, and hence 15 elements  $F(i)$  of the neutron spectrum can be solved, if the remaining 11 elements are put equal to the calculated neutron flux values.

Unfortunately, the condition of the coefficient matrix of the system is rather poor and no reliable results were obtained from the direct solution of the system. However, neglecting the more detailed spectral irregularities, it is known from theory (49) that in the case of weak absorption or very slowly varying absorption, the

relation between the neutron flux density per unit energy  $\phi(E)$  and the energy  $E$  can be written as:

$$\ln E \phi(E) = c \ln E + k \quad (5.3)$$

where  $c$  and  $k$  are constant.

Assuming that relation (5.3) is correct for the centre of the ATHENE core, it is easy to find  $c$  from a least squares fit:

$$\frac{d}{dc} \sum_{m=1}^{15} \left\{ \sum_{i=1}^{gun-1} F_c(i) \cdot eff(i) (trf(m,i) - r_l(m)) + \sum_{i=gun}^{26} F_c(i) \cdot eff(i) \right. \\ \left. (trf(m,i) - r_l(m)) \right\}^2 = 0 \quad (5.4)$$

where  $gun$  is the lowest group number of the unknown group flux elements  $F_c(i)$ .  $F_c(i)$  is found from :

$$F_c(i) = e^k \cdot (E_{up,i} \cdot E_{low,i})^{\frac{c}{2}} \cdot \ln \frac{E_{up,i}}{E_{low,i}} \quad (5.5)$$

$E_{up,i}$  and  $E_{low,i}$  are the upper and lower boundaries of the energy group  $i$ . The values of  $F_c(i)$ , for  $i < gun$ , are again put equal to the calculated group flux values. The constant  $k$  has been determined by the normalization:

$$F_c(gun) = F(gun) \quad (5.6)$$

where  $F(gun)$  is the calculated value of  $F_c(i)$ , for  $i = gun$ .

Varying  $gun$  gives a variation of the resulting value of  $c$ . The mean value of  $c$ , resulting from formula (5.4) for the different values of  $gun$ , is :

$$c = 0.023 \pm 0.005 \quad (5.7)$$

In Fig. 5.1 the resulting straight line through the points  $F_c(i)$  is normalized to group 12 ( $4.65 \text{ keV} < E < 10 \text{ keV}$ ).

## 5.2. The $UO_2$ and $ThO_2$ Doppler measurements

A series of temperature dependent neutron absorption measurements of natural  $UO_2$  and  $ThO_2$  samples has been carried out for the three neutron spectra of Fig. 2.5 (see also Fig. 3.17). The sample properties of  $UO_2$  and  $ThO_2$  are listed in Table 5.1 and Table 5.2 respectively. In Fig. 5.2 to 5.6 incl. the measuring results are shown in different ways. In Figs. 5.2 and 5.3 the neutron absorption signal is given as a function of the sample temperature. The vertical marks indicate the statistical errors of the individual measuring values. In Figs. 5.4 and 5.5 the neutron absorption is a function of the sample mass. In Fig. 5.6 the relative change of the neutron absorption, indicated as the Doppler effect  $D$ , is shown for the temperature interval 293-1300 K. A Monte Carlo calculation by the program MCTRANS of the neutron absorption in the  $UO_2$  samples has been carried out with a set of point cross-sections of the KEDAK file, as listed by Schmidt (50). The cross-sections between 1 and 1000 eV were calculated from the resonance parameters of the resolved resonances without Doppler broadening. The cross-sections in the range of 1 keV to 10 MeV are based on an average "eye-guide" curve drawn through all listed experiments available before 1962 and they were not corrected for energy resolution nor for Doppler broadening. In Fig. 5.4 these calculations are labelled with the temperature 0 K which is consequently not quite correct. Unfortunately, a more extensive set of Doppler broadened point cross-sections (with resolved resonances up to 4 keV), under preparation, could not be produced in time.

Another comparison with calculation has been made with the program RICH (51), which calculates temperature dependent effective resonance integrals, using the Doppler broadened single level Breit-Wigner formulae. De Kruijf (52) has so adapted RICH that it had become possible to calculate the effective resonance integrals for infinite slabs of material. The RICH calculation results for room

Table 5.1 The properties of the UO<sub>2</sub> samples

UO <sub>2</sub>		
general impurity level <0.1 %		
isotope composition:		
<sup>234</sup> U		0.0055%
<sup>235</sup> U		0.716 %
<sup>236</sup> U		0.001 %
<sup>238</sup> U		99.27 %
diameters ~ 40 mm		
sample indication	thickness mm	mass g
U-1	1.06 <sub>±</sub> 0.10	14.105
U-2	2.21 <sub>±</sub> 0.10	29.345
U-3	3.20 <sub>±</sub> 0.10	42.400
U-5	5.01 <sub>±</sub> 0.01	65.082
U-7.5	7.57 <sub>±</sub> 0.01	99.864
U-10	10.03 <sub>±</sub> 0.01	132.912
U-15	15.16 <sub>±</sub> 0.02	197.589
U-20	20.17 <sub>±</sub> 0.02	262.671

Table 5.2 The properties of the ThO<sub>2</sub> samples

ThO <sub>2</sub>		
general impurity level <0.2 %		
heavy metals <0.003%		
carbon <0.002%		
diameters ~ 40 mm		
sample indication	thickness mm	mass g
Th-3	2.6 <sub>±</sub> 0.2	19.565
Th-6	5.9 <sub>±</sub> 0.2	49.402
Th-9	8.8 <sub>±</sub> 0.2	73.752
Th-15	15.1 <sub>±</sub> 0.2	122.720

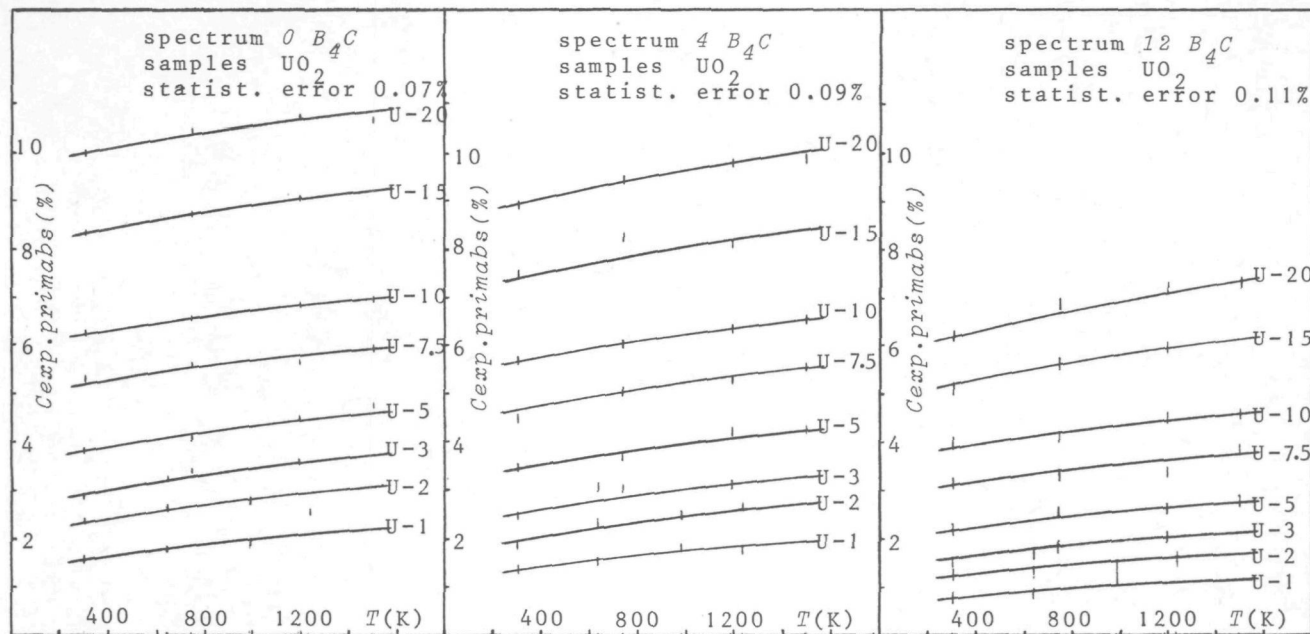


Fig. 5.2 The temperature dependent primary neutron absorption in the UO<sub>2</sub> samples corrected for thermal sample expansion

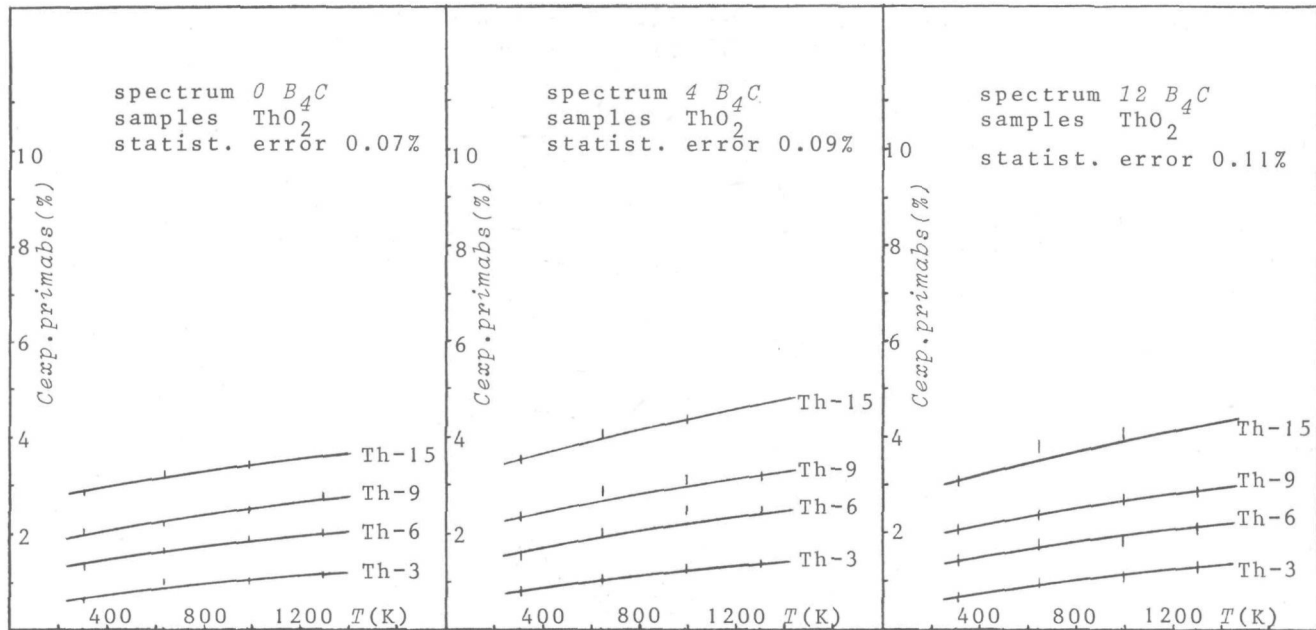


Fig. 5.3 The temperature dependent primary neutron absorption in the  $ThO_2$  samples corrected for thermal expansion

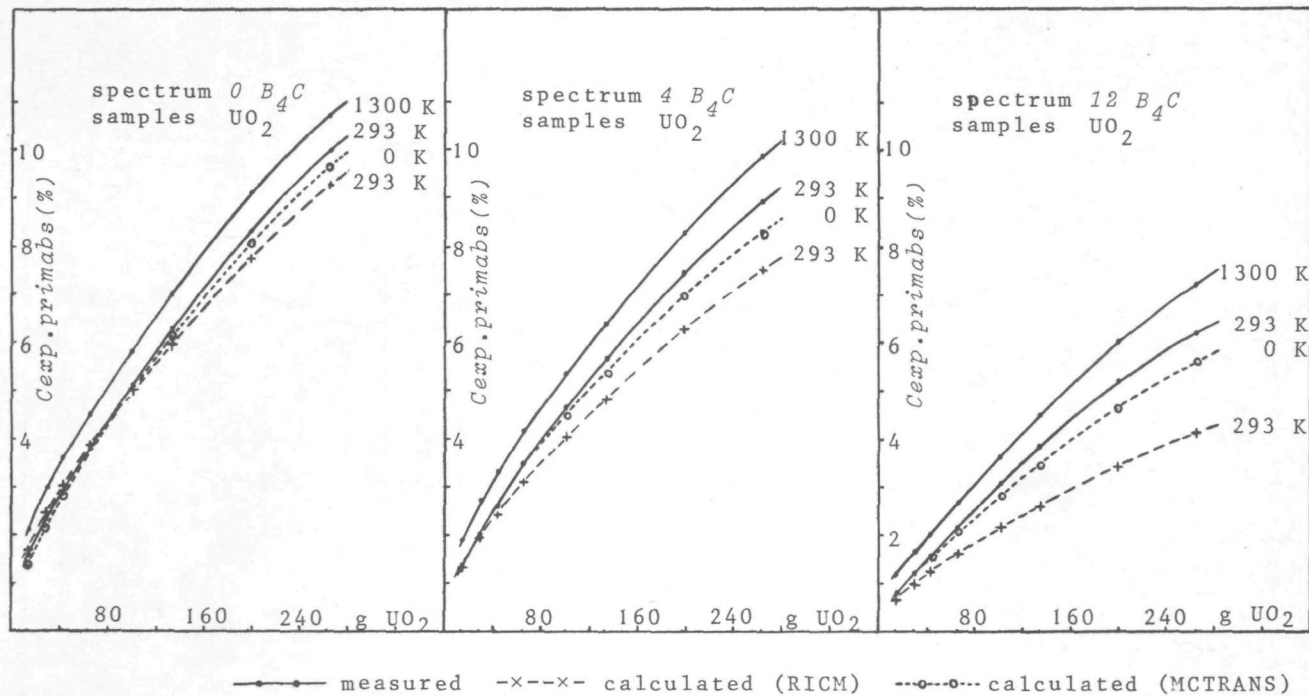


Fig. 5.4 The primary neutron absorption in the UO<sub>2</sub> samples as a function of the sample mass

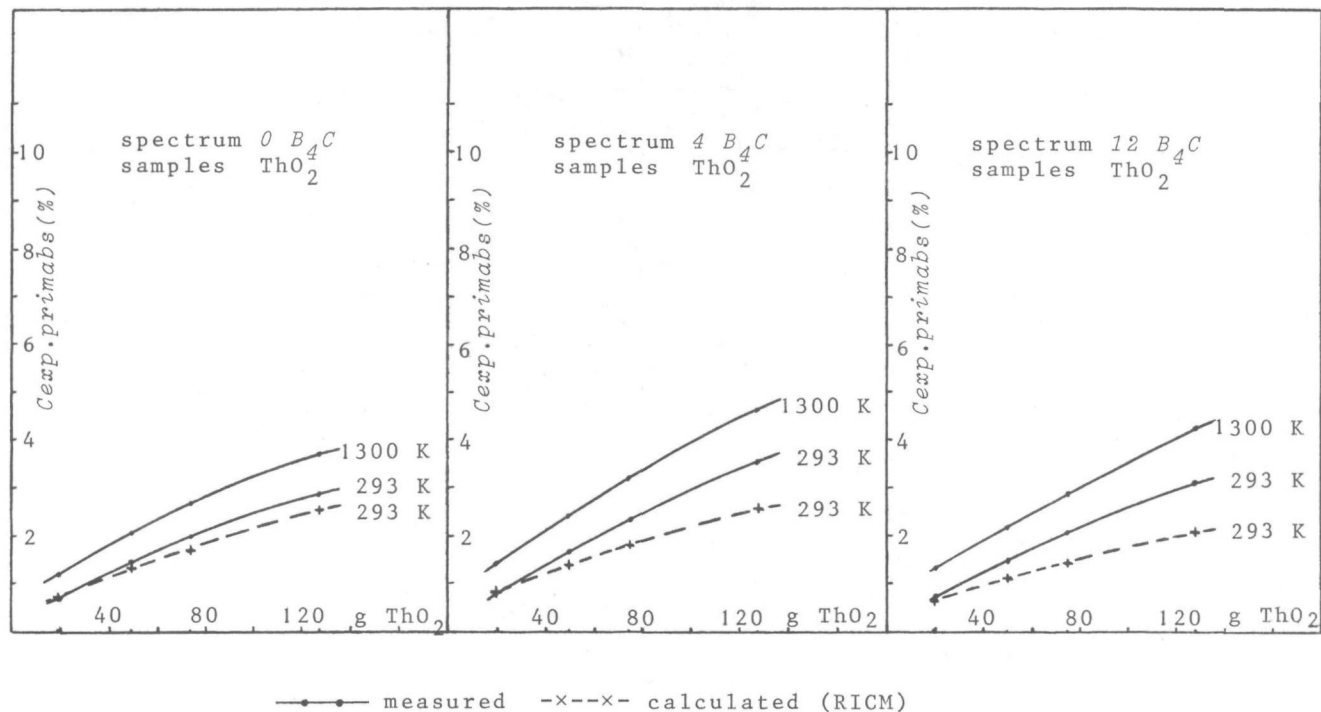
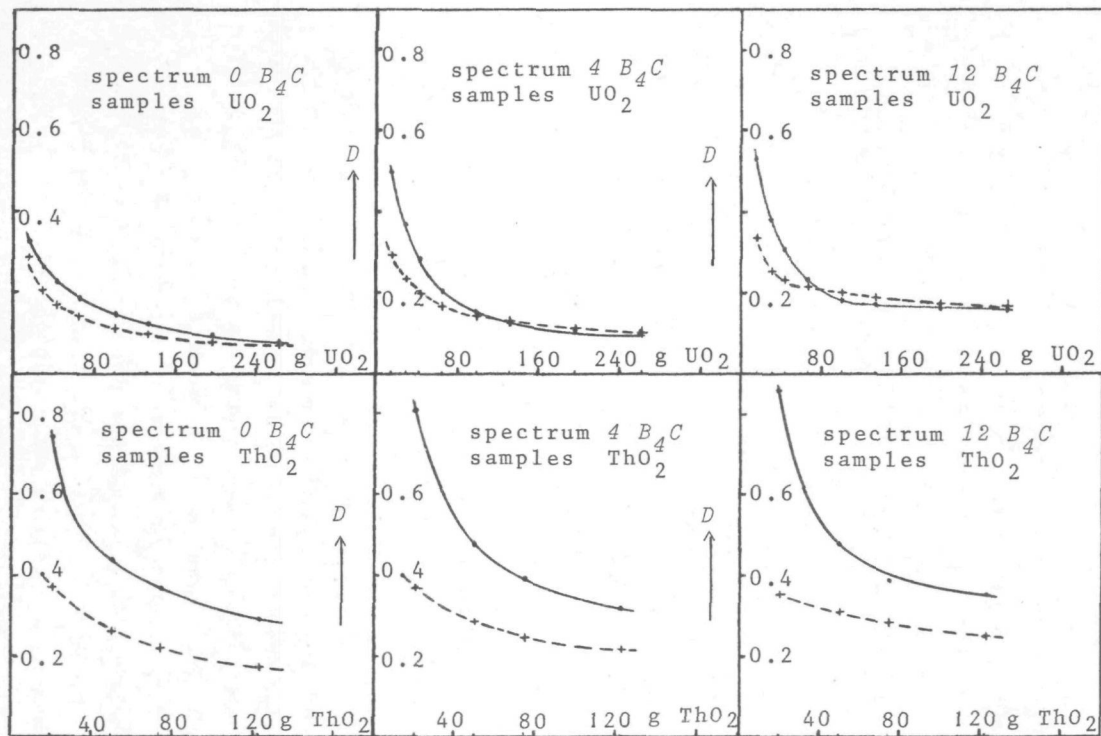


Fig. 5.5 The primary neutron absorption in the  $ThO_2$  samples as a function of the sample mass



—●— measured (as found from Figs. 5.4 and 5.5)    -x--x- calculated (RICM)

Fig. 5.6 Doppler effect (293-1300 K) of the  $UO_2$  and  $ThO_2$  samples

temperature are shown in Fig. 5.4 and 5.5. The Doppler effect  $D$ , calculated from the RICM results, is shown in Fig. 5.6. The RICM temperature dependent effective resonance integrals for both  $UO_2$  and  $ThO_2$  have been calculated with the ENDF/B-III resonance parameters

An evaluation of the error margins is given in sec. 5.3. With the results of this error discussion it may be stated that, partially in consequence of the large error margins, there is good agreement between measurement and calculation of the  $UO_2$  absorption signal and the  $UO_2$  Doppler effect in the case of the  $\frac{1}{E}$  spectrum ( $O B_4 C$  spectrum).

The fast neutron spectrum results of  $UO_2$  are compared with some other experiments in the literature. Table 5.3 gives a comparison of several fast neutron spectrum  $^{238}U$  Doppler experiments. Although there may be important differences in the experimental circumstances of the various experiments, the C/E ratio of the calculated Doppler effect C and the experimental value E can be used as a measure of comparison. The second column of Table 5.3 gives a coarse indication of the applied neutron spectra (see also Fig. 1.2). The third column indicates the technique which is used in the experiment. The fourth column gives some information about the samples. In all experiments of Table 5.3 except those of the present work, the samples were irradiated in or near the centre of a critical reactor core. So in all these cases the neutron flux incident on the sample was shielded in a different way by the surrounding fissile and fertile materials. A good evaluation of the influence of the sample thickness on the Doppler effect is therefore very difficult. The C/E values of the seventh column are the quotients of the calculated and measured temperature induced changes of the signals. The bracketed experimental uncertainties of this work indicate the expected uncertainties for the improved version of the graphite ball detector as proposed in sec. 5.3.3. Till (11) gives a compilation of the most important fast spectrum

Table 5.3 Comparison of  $^{238}\text{U}$  fast neutron spectrum Doppler experiment results of different measurement techniques

LMFBR : liquid metal fast breeder reactor spectrum  
 SCFBR : steam cooled fast breeder reactor spectrum  
 R.O. : reactivity oscillation induced by Doppler sample  
 A.A. : activation analysis of Doppler sample

author	spectrum indication	measur. technique	samples	temp.interv. K	experim. uncertainty	C/E Doppler effect
C.E. Till(11)	LMFBR (U-fuelled)	R.O.	general	293-1100	2-5%	~ 0.8
	LMFBR (Pu-fuelled)	R.O.	general	293-1100	2-5%	~ 1.0
G.J. Fischer(7)	LMFBR (Pu-fuelled)	R.O.	$\text{UO}_2$ rods length 6", dia. 0.5"	500-1100	< 8%	0.72
	SCFBR (Pu-fuelled)	R.O.	$\text{UO}_2$ rods length 6", dia. 0.5"	500-1100	< 6%	0.97
E.A. Fischer(8)	SCFBR (U-fuelled)	R.O.	$\text{UO}_2$ rods length 90 mm, dia. 35 mm	300-1000	2-5%	~ 1.0
	SCFBR (Pu-fuelled)	R.O.	$\text{UO}_2$ rods length 90 mm, dia. 35 mm	300-1000	2-5%	~ 0.9
G.R. Pflasterer(20)	LMFBR (U-fuelled)	A.A.	U-metal foils thick. 0.003", 0.005", dia. 0.49"	293-715	~ 10%	~ 0.5
L.I. Tirén(21,26)	LMFBR	A.A.	$\text{UO}_2$ disks <sup>2</sup> 0.27 g/cm <sup>2</sup>	300-1800	10%	0.65-0.80
this work	SCFBR (12 B <sub>4</sub> C)	beam	thin (1.1 g/cm <sub>2</sub> <sup>2</sup> )	293-1300	45% (13)	0.63
		transm.	thick (22 g/cm <sup>2</sup> )	293-1300	20% (10)	1.03

(LMFBR) reactivity oscillation Doppler experiments in the U.S. up to 1972 for several resonance absorber materials. Combining the results of all  $^{238}\text{U}$  experiments he arrives at the conclusion of a general tendency to underpredict the  $^{238}\text{U}$  Doppler effect measured in critical assemblies. For  $^{235}\text{U}$  fuelled assemblies the measured  $^{238}\text{U}$  Doppler effect has usually been underpredicted by 20% or more. The  $^{238}\text{U}$  Doppler effect normalized to the  $^{235}\text{U}$  reactivity worth at the same position has been underpredicted by 30% or more. For plutonium fuelled systems, the pattern is somewhat different. The measured  $^{238}\text{U}$  Doppler effect has generally been matched quite well by calculation, but the  $^{238}\text{U}$  Doppler effect normalized to the worth of  $^{239}\text{Pu}$  at the same position has usually been underpredicted by approximately 25%. Till also gives a comparison of C/E values for calculations using different cross-section data and calculation procedures. The C/E ratio for the  $^{238}\text{U}$  Doppler effect normalized to the reactivity worth of the main fuel fissile isotope varies from 0.59 to 0.69 for the U-fuelled assembly and from 0.69 to 0.82 for the Pu-fuelled assembly. From Table 5.3 and the foregoing it may be clear that there are still considerable discrepancies between the measured and the calculated  $^{238}\text{U}$  Doppler effect, part of which is undoubtedly caused by interpretation problems and experimental uncertainties.

In contrast with the rather numerous  $^{238}\text{U}$  Doppler measurements, only very few authors make mention of Th Doppler measurements. Dekker(32) and some others mentioned by Dekker, have measured and calculated the resonance integral and the Doppler effect of some Th metal rods in a  $\frac{1}{E}$  flux. Within the error limits of 10-20% he found a reasonable agreement between measurement and calculation.  $\text{ThO}_2$  Doppler measurements in a  $\frac{1}{E}$  spectrum have also been reported - see for instance (53) - but no comparison with calculation has been given. Till (11) is the only one who mentions Th Doppler measurements in fast neutron spectra. However he does not give C/E values. As far as is known to the author no Doppler C/E values of Th or  $\text{ThO}_2$  in fast neutron spectra are available at the moment.

In this work the absorption signals and the Doppler effects of several  $\text{ThO}_2$  disks have been measured and calculated by RICM. See Table 5.2 and Figs. 5.3, 5.5 and 5.6. In view of the tendency of RICM to underpredict the absorption signals of thick samples, compared with the Monte Carlo calculation in the case of  $\text{UO}_2$ , the agreement between measurement and calculation in the case of  $\text{ThO}_2$  in the  $\frac{1}{E}$  spectrum ( $O B_4 C$  spectrum) is reasonable and is certainly within the error limits (see sec. 5.3.). Although the error margins of the  $\text{ThO}_2$  Doppler measurements are rather large, the RICM calculations with the ENDF/B-III resonance data seem to underpredict the  $\text{ThO}_2$  Doppler effect.

### 5.3. Error discussion

#### 5.3.1. Experimental uncertainties

An evaluation of the error margins of both the experimental results and the corresponding calculations is necessary for a good comparison.

The experimental uncertainties may be divided into several groups:

- uncertainty in the determination of the absorption signal  $primabs$  of a cold sample;
- uncertainty in the Doppler effect  $D$  of a one-sample measurement;
- uncertainty in the determination of  $primabs$  and  $D$  from the curves of a series of sample measurements.

For a clear picture of the experimental uncertainties the formulae (3.43, 41, 42, 44) for the determination of the absorption signal and the Doppler effect are repeated here:

$$primabs = abs - secabs \quad (5.8)$$

$$abs = \frac{R_{abs} - ref_b \cdot W_{abs} + scfr \{ 1 - cmod.c12.ref_{sc}(exp) \} \cdot R_{abs}}{R_{abs}} \quad (5.9)$$

$$scfr = \frac{W_{sc} - (1-abs).wac.bicratio.R_{sc}}{\left\{ \frac{1}{ref_b} - cmod.c12.ref_{sc}(exp).wac \right\}.bicratio.R_{sc}} \quad (5.10)$$

$$D = \frac{C_{exp}.primabs_w - primabs_c}{primabs_c} \quad (5.11)$$

All the measurement results have been determined from neutron countings. So each single measurement has a statistical uncertainty. Assuming that all factors of formula (5.9) are fixed values, except for the countings  $R_{abs}$  and  $W_{abs}$ , the statistical uncertainty in  $abs$  has been calculated for each measurement by the on-line PDP-9 computer. Typical absolute values of the standard deviation in  $abs$ , due to counting statistics, are 0.0007, 0.0009 and 0.0011 for the  $0 B_4C$ , the  $4 B_4C$  and the  $12 B_4C$  spectrum measurements respectively, which is indicated by the vertical marks in Figs. 5.2 and 5.3.

The systematic error in the absorption signal  $primabs$  of a cold sample is composed of the uncertainties in the various factors and corrections of the formulae (5.8,9,10). The systematic error in  $abs$  is determined by  $ref_b$ ,  $scfr$ ,  $cmod$  and  $c12$  ( $ref_{sc}(exp) = 1$ ). The differences between  $W_{abs}$  and  $R_{abs}$  are small for samples with small absorption. So the ratio  $W_{abs}/R_{abs}$  is always near 1 and the uncertainty in  $abs$  due to  $ref_b$  equals the undiminished uncertainty in  $ref_b$ . From sec. 3.6.2. it follows that the uncertainty in  $ref_b$  is 0.0004, 0.0006 and 0.0008 for the  $0 B_4C$ , the  $4 B_4C$  and the  $12 B_4C$  spectrum respectively. The uncertainty in the correction  $scfr(1 - cmod.c12)$  consists of a statistical error in  $scfr$ , which is determined in each measurement from the counting results  $W_{sc}$  and  $R_{sc}$  using formula (5.10), and a systematic error in each of the terms. The value of  $scfr$  varies from about 0.05 to 0.55 for the different samples and  $(1 - cmod.c12)$  is continually about 0.05. The typical error in  $scfr$  due to counting statistics is 0.0004, 0.0006 and 0.0008 for the  $0 B_4C$ , the  $4 B_4C$  and the  $12 B_4C$  spectrum respectively. Because of the multiplication by 0.05 the statistical error in  $scfr$  may be neglected. A systematic error in  $scfr$  is caused by the uncertainties

in the various terms of formula (5.10) on the one hand and by the neglect of the influence of the  $Bt-C$  scatterer hole in the graphite ball on the other. The influence upon  $abs$  of the former may be neglected in consequence of the smallness of  $wac$  and the multiplication by 0.05. In sec. 3.5.2. it is estimated that  $scfr$  is determined 2-4% (relative) too low, depending on the neutron spectrum, owing to the influence of the  $Bt-C$  scatterer hole. However, in the determination of  $c12$  from the measurement of  $emod.c12$  and the calculation of  $emod$  for some graphite samples, as discussed in sec. 3.5.5., the same underestimate of  $scfr$  has been made, resulting in a shifting of  $c12$  which compensates exactly the underestimate of  $scfr$  for graphite samples and which also compensates almost completely the underestimate of  $scfr$  for  $UO_2$  and  $ThO_2$ . Therefore, the influence of the shifting of  $scfr$  will be neglected.

In the calculation of  $emod$  the most important source of error is the uncertainty of the inelastic scattering cross-sections, as discussed in sec. 3.5.5. The order of  $emod$  and the uncertainty in  $emod$  (with an assumption of 10% uncertainty in  $\sigma_{inel}$ ) is  $0.95 \pm 0.003$ . In sec. 3.5.5. the uncertainty in  $c12$  is estimated to be 0.0015, 0.0019 and 0.0023. Treating the errors as maximum errors, the order of  $(1 - emod.c12)$  and its uncertainty are estimated to be  $0.05 \pm 0.0045$ , 0.0049, 0.0053 for the three spectra. The influence upon  $abs$  depends on  $scfr$  and varies with the sample thickness.

The uncertainty in the secondary neutron absorption  $secabs$  (see sec. 3.7.2.) is 0.0009, 0.0012 and 0.0015 for the  $0 B_4C$ , the  $4 B_4C$  and the  $12 B_4C$  spectrum respectively. However (see Fig. 3.18), with sample mass decreasing to 0,  $secabs$  also decreases smoothly to 0 as a fixed point. Therefore the uncertainty mentioned only holds for the thick samples. The uncertainty in  $secabs$  of the thin samples is estimated to be half the values mentioned.

The systematic error in  $primabs$  of a cold sample is given in Table 5.4. The uncertainty in the sample thickness has been neglected.

The uncertainty in the Doppler effect  $D$  of a one-sample measurement may also be divided in a statistical error and a systematic error.

Table 5.4 The systematic error in *primabs* for a single, cold sample measurement

	$0 B_4C$	$4 B_4C$	$12 B_4C$
thin sample	0.0011	0.0014	0.0018
thick sample	0.0036	0.0043	0.0050

Since the statistical uncertainty of the difference of the two terms in the numerator of formula (5.11) is much larger than the statistical uncertainty of the denominator, the statistical error in  $D$  will be considered to originate only from the numerator. Treating the statistical errors of  $primabs_w$  and  $primabs_c$  as standard deviations, the standard deviation of the numerator of formula (5.11) is 0.0010, 0.0013 and 0.0015 for the  $0 B_4C$ , the  $4 B_4C$  and the  $12 B_4C$  spectrum respectively.

The systematic uncertainty in  $D$  is caused by the systematic errors of the temperature dependent factors in the numerator of formula (5.11) and the systematic uncertainty of the denominator.

With an estimate of 10% uncertainty in the linear expansion coefficient  $\alpha$ , the uncertainty in  $C_{exp}$ , at  $\Delta T = 1000$  °C, is about 0.001 and will be neglected.

A temperature dependent systematic error in  $primabs_w$  is caused by the additional reference correction for the scattered neutrons  $ref_{sc}(exp)$  which is discussed in sec. 3.6.2. The uncertainty in  $ref_{sc}$ , at  $\Delta T = 1000$  °C ( $exp \approx 1.0$  mm), is estimated to be 0.0008, 0.0010 and 0.0012 for the  $0 B_4C$ , the  $4 B_4C$  and the  $12 B_4C$  spectrum respectively. Consequently, the uncertainty in *abs* is negligible for the thin samples and increases to 0.0004, 0.0005 and 0.0006 for the thick samples. The joint systematic error in  $D$ , except for the shifting of  $D$  due to the secondary neutrons, is listed in Table 5.5 for the  $UO_2$  samples. The uncertainty in the temperature measurement of the samples is estimated to be less than 50 °C and has been neglected.

Table 5.5 The relative systematic error in  $D$ , except for the shifting due to the secondary neutrons, for the  $UO_2$  samples

	$0 B_4C$	$4 B_4C$	$12 B_4C$
thin sample	7.0%	11.2%	24.0%
thick sample	8.9%	10.0%	13.9%

The most inelegant error in  $D$  is caused by the Doppler effect of the secondary neutrons. Assuming that the fraction of  $D$ , which is caused by the secondary neutrons, equals the fraction of  $abs$  caused by the resonance part of the secondary neutrons (and it may be worse), the secondary part of  $D$  has been calculated for the  $UO_2$  samples. Table 5.6 gives the relative contribution to  $D$  of the secondary neutrons in the  $UO_2$  samples. The curves of Fig. 5.6 have not been corrected for the secondary part of  $D$ .

Table 5.6 The estimated relative contribution to the Doppler effect  $D$  of the secondary neutrons in the  $UO_2$  samples

	$0 B_4C$	$4 B_4C$	$12 B_4C$
thin sample	4.4%	7.2%	13%
thick sample	3.7%	5.5%	9%

Table 5.7 The total uncertainty in the individual absorption signals of  $UO_2$ , determined from the curves of Figs. 5.2 and 5.4

	$0 B_4C$		$4 B_4C$		$12 B_4C$	
		rel.to <i>primabs</i>		rel.to <i>primabs</i>		rel.to <i>primabs</i>
thin sample	0.0014	8.9%	0.0017	13.6%	0.0022	29.3%
thick sample	0.0039	3.9%	0.0046	5.2%	0.0054	8.7%

Table 5.8 The total uncertainty in the individual absorption signals of  $ThO_2$  determined from the curves of Figs. 5.3 and 5.5

	$0 B_4C$		$4 B_4C$		$12 B_4C$	
		rel.to <i>primabs</i>		rel.to <i>primabs</i>		rel.to <i>primabs</i>
thin sample	0.0015	22.2%	0.0019	24.5%	0.0024	34.2%
thick sample	0.0040	13.9%	0.0048	13.6%	0.0056	18.1%

Table 5.9 The total uncertainty in the Doppler effect  $D$  of the  $UO_2$  samples determined from the curves of Figs. 5.2 and 5.4

	$0 B_4C$		$4 B_4C$		$12 B_4C$	
		rel.		rel.		rel.
thin sample	0.056	16.7%	0.109	21.9%	0.238	44.7%
thick sample	0.011	14.1%	0.016	15.4%	0.033	19.9%

Table 5.10 The total uncertainty in the Doppler effect  $D$  of the  $ThO_2$  samples, determined from the curves of Figs. 5.3 and 5.5

	$0 B_4C$		$4 B_4C$		$12 B_4C$	
		rel.		rel.		rel.
thin sample	0.236	31.9%	0.290	36.0%	0.405	47.3%
thick sample	0.072	25.0%	0.075	24.2%	0.107	30.8%

From theory it is known that the absorption rate in a Doppler sample is a smoothly varying function with both varying temperature and varying sample mass. As a matter of fact, the absorption rate may be looked upon as a three-dimensional curvature smoothly changing with both sample weight and sample temperature. If the mathematical shape of the curvature were known, except for only one parameter, the statistical uncertainty in this parameter would be reduced by a factor  $\sqrt{m}$  by the determination of  $m$  independent measurement points of the curvature. The absorption curvature of  $UO_2$  ( $ThO_2$ ) is determined by 30 (15) statistically independent measurement points.

Unfortunately, the exact shape of the curvature is not known. However, an estimated statistical error reduction by  $\frac{1}{2}\sqrt{30}$  ( $\frac{1}{2}\sqrt{15}$ ) in the determination of the individual absorption rates from the curves of Figs. 5.2-5 seems to be reasonable.

The total uncertainty in the individual absorption signals determined from the curves of Figs. 5.2-5 is listed in Tables 5.7 and 5.8. The total uncertainty in the Doppler effect  $D$ , determined from the curves of Figs. 5.2-5 is listed in Tables 5.9 and 5.10.

### 5.3.2. Calculation errors

To evaluate the uncertainties in the Monte Carlo calculations of the absorption signals, the expression for  $abs$  may be derived from formula (4.2):

$$abs = 1 - \frac{\sum_g \phi_g \cdot tr(l, \Sigma_g) \cdot eff_g \cdot \Delta E_g}{\sum_g \phi_g \cdot eff_g \cdot \Delta E_g} \quad (5.12)$$

For each sample and each temperature a separate calculation of  $tr(l, \Sigma_g)$  has to be carried out by the MCTRANS program. The elements  $\phi_g$ ,  $eff_g$  and  $\Delta E_g$  are fed into MCTRANS as fixed input data. So the uncertainty in  $abs$  consists of a statistical error in  $tr(l, \Sigma_g)$  and a systematic error in each of the elements of formula (5.12). The uncertainties in the neutron spectra and in the detector efficiency have been discussed in chapter 4. And since they are both in the

numerator and in the denominator of formula (5.12), and since  $tr(l, \Sigma_g)$  is not much smaller than 1, their influence upon  $abs$  is small and will be neglected. The calculation model of the disk-shaped samples in MCTTRANS is quite accurate and no systematic error of  $tr(l, \Sigma_g)$  needs to be taken into account. The remaining error to be considered is the statistical error of the Monte Carlo process. Typical absolute errors in the calculated values of  $abs$  due to the Monte Carlo statistics are 0.0015 for the thin samples and 0.004 for the thick samples.

As already mentioned in sec. 5.2., the Monte Carlo MCTTRANS calculations of the  $UO_2$  absorption signals were carried out with a set of point cross-sections of the KEDAK file of 1962. The cross-sections below 1000 eV were calculated from the resonance parameters without Doppler broadening. The cross-sections above 1000 eV were based on an "eye-guide" curve drawn through all listed experiments, which had been carried out at room temperature. To be able to estimate the necessary correction of the MCTTRANS curves, an additional set of RICM calculations has been carried out for the U-1 and the U-20 samples. In these calculations the resonance parameters were not Doppler broadened. With the effective group cross-sections from these calculations and with those from the normal RICM calculations at room temperature (RICM(293 K)) it was possible to calculate the absorption signals with Doppler broadening above 1000 eV and without Doppler broadening below 1000 eV (RICM(0 K below 1000 eV)). Now the ratio RICM(293 K) / RICM(0 K below 1000 eV) was applied to raise the MCTTRANS values of the absorption signals as a correction for the room temperature Doppler effect.

However, a cause of shifting 5 or 6% (relative) in the opposite direction, in the case of the  ${}^0B_4C$  spectrum only, is the effective Cd cut-off energy. Before entering the graphite ball the neutron beam passes through a 1.5-mm Cd foil. No special effort has been made to determine the effective Cd cut-off energy, which is estimated to be between 0.7 and 0.8 eV. The MCTTRANS calculations as well as the RICM calculations have utilized the group structure of the Bondarenko cross-section set (44). All calculations of  $abs$  and  $D$  are based on a

cut-off energy of 1.0 eV, being the boundary of one of the groups. With a cut-off energy of 0.465 eV, which is also a group boundary, all calculated  $0 B_4C$  points of Figs. 5.4 and 5.5 are lowered by about 12%. With an effective cut-off energy of about 0.75 eV the calculated  $0 B_4C$  curves of Figs. 5.4 and 5.5 would be lowered by 5 or 6% (relative) and the  $0 B_4C$  Doppler effect curves of Fig. 5.6 would be raised by 5 or 6% relative.

The corrected MCTTRANS values are shown in Table 5.11.

Table 5.11 The MCTTRANS calculated absorption signals for the U-1 and the U-20 samples after the estimated corrections for the room temperature Doppler effect and the effective Cd cut-off energy

	$0 B_4C$	$4 B_4C$	$12 B_4C$
thin sample	0.01503	0.01639	0.00865
thick sample	0.09475	0.08831	0.06267

Evaluation of the accuracy of the RICM calculations is quite difficult. The most important approximation that is used in the program may be the assumption of a homogeneous distribution of the collision points in the sample, which is less accurate with increasing sample thickness. The representation of the disk-shaped samples by infinite slabs is also less accurate with increasing sample thickness. The best comparison of the RICM calculations is with the MCTTRANS Monte Carlo calculations. It turns out that RICM underpredicts the *abs* values for thick samples and fast neutron spectra.

No corrections have been applied for the crystal-binding effect. The energy distribution of the nuclei of a solid target is found to be of the same Maxwellian shape as for a gaseous target (54), but with a changed effective temperature:

$$T_{eff} = \frac{3}{2} \theta_D \int_0^1 x^3 \operatorname{coth} \left\{ \frac{\theta_D}{2T} \cdot x \right\} dx \quad (5.13)$$

where  $\theta_D$  is the Debye temperature (K) and  $T$  is the thermodynamic temperature (K).

Schmidt (55) gives a Debye temperature of  $\text{UO}_2$   $\theta_D = 600$  K. For  $T = 293$  K  $T_{eff}$  is found to be  $T_{eff} = 350$  K. Using  $T_{eff}$  instead of  $T$  would raise the calculated value of  $abs$  by about 0.0005. For  $T = 1300$  K,  $T_{eff} \approx T$ , so the calculated Doppler effect will decrease by 6 to 7%. On the other hand, the estimations for  $\theta_D$  vary between 200 K and 600 K (56) which would indicate the 6 to 7% to be a maximum.

### 5.3.3. Conclusions

Several conclusions can be made after studying the measurement and calculation uncertainties.

1. In all cases the  $^{12}\text{B}_4\text{C}$  (fast spectrum) experimental results are much more inaccurate than the  $^0\text{B}_4\text{C}$  ( $\frac{1}{E}$  spectrum) results. Except for the relative contribution to the Doppler effect of the secondary neutrons, the increase in inaccuracy is due to worse counting statistics of the individual  $^{12}\text{B}_4\text{C}$  countings and the counting in the determination of the  $^{12}\text{B}_4\text{C}$  correction factors. These worse counting statistics are the consequence of the limited reactor power (4 kW) of the ATHENE reactor and the maximum accepted single measurement time of about 200 min. If it had been possible to raise the reactor power to the same counting level as in the  $^0\text{B}_4\text{C}$  case, the  $^{12}\text{B}_4\text{C}$  statistics would have equalled almost the  $^0\text{B}_4\text{C}$  statistics.
2. In all measurement results, especially the absorption signals, the systematic uncertainties are predominant. All systematic uncertainties, except for the one in  $mod$ , are caused by counting statistics. In consequence of the forced time schedule of the measurement series, the time to be spent on the determination of the correction factors has been limited. A

reduction of these systematic uncertainties by at least a factor 2 seems very well possible.

3. The most important systematic error, especially for the thick samples, is the uncertainty in  $\sigma_{mod}$ , caused by the uncertainty of the inelastic scattering cross-sections.

A reduction of this error can only be realized by a reduction of the counting efficiency of the neutrons with energies above 30 keV. A small reduction of the thickness of the graphite shell would be very effective. See Fig. 2.6.

4. The most inelegant error is the contribution to the Doppler effect of the secondary neutrons (neutrons reentering the sample after being scattered in the graphite shell), which is caused by the repeated crossing of the inner space of the ball by most of the neutrons.

The "secondary Doppler effect" can be eliminated in two ways:

- (1) measurement with and without secondary sample in a specially designed oven (see sec. 3.7.);
- (2) the "secondary Doppler effect" can be reduced by choosing a larger inner diameter of the graphite ball. To reduce it by a factor 4, the inner diameter would have to be raised from 20 to 40 cm.

5. After the estimated corrections of the MCTTRANS- $0 B_4C-UO_2$  curve of Fig. 5.4 for the room temperature Doppler broadening and for the effective Cd cut-off energy, the difference "measured - MCTTRANS" is +0.0007 for the thin sample up to + 0.0047 for the thick sample, which values are very well within the error limits.

For the MCTTRANS calculations of the  $4 B_4C$  and the  $12 B_4C$  spectrum the room temperature Doppler broadening corrections are less than for the  $0 B_4C$  spectrum. The agreement between the measured and the MCTTRANS calculated curves of Fig. 5.4 is within the error limits.

6. RICM underpredicts the absorption signal for thick samples and fast neutron spectra.
7. Although the agreement between measurement and RICM calculation

of the  $UO_2$  Doppler effect is almost completely within the error limits, it tends to be underpredicted for the thin samples.

8. RICM underpredicts the  $ThO_2$  Doppler effect, especially for the thin samples.
9. Without fundamental changes in the measuring system, considerable error reduction is still possible.

A calculation has been made for possible error reduction under the following assumptions:

- (a) The neutron beam intensity (reactor power) is not limited.
- (b) The inner diameter of the graphite ball is 40 cm (was 20 cm).
- (c) The thickness of the graphite shell is such that the influence of the uncertainty in  $\sigma_{mod}$  is reduced to 0.001 (was 0.003).
- (d) The counting statistics are the same for the three spectra and equal the  $0 B_4 C$  statistics of the performed series (i.e. 100 min per individual measurement at a counting rate of about 4000 c/s).
- (e) The influence of the systematic errors (except for  $\sigma_{mod}$ ) is reduced by a factor 2. See also point 2 mentioned above.
- (f) The  $ThO_2$  measurement series is also extended to 30 independent measurements.

The outcome of the calculations is:

total error in <i>primabs</i> (with all spectra)	}	thin 0.00085 (was 0.0014-0.0022)
		thick 0.0019 (was 0.0039-0.0054)

total relative error in <i>D</i> (with all spectra)	}	thin $UO_2$ : 13% (was 16.7-44.7%)
		$ThO_2$ : 19% (was 31.9-47.3%)
		thick $UO_2$ : 10% (was 14.1-19.9%)
		$ThO_2$ : 14% (was 25.0-30.8%)

"secondary Doppler effect"	thin 3% (was 13%)
	thick 2% (was 9%)

## APPENDIX

### *The backward Monte Carlo routine*

To show the analogy of the backward to the forward Monte Carlo routines, the most important procedures of the forward Monte Carlo technique and the forward transition probability from source to target will be given first.

In the normal forward Monte Carlo technique it is usual to select neutrons from a source. By repeated selection of neutron histories from the transport kernel  $T(\underline{r}' \rightarrow \underline{r}, \underline{U})$  and the collision kernel  $C(\underline{U}' \rightarrow \underline{U}, \underline{r})$ , the transition probability from the source to the target can be found.

$\underline{r}$  represents the space coordinates  $x, y, z$ .

$\underline{U}$  represents the speed coordinates of the neutron:

lethargy  $u$  (or neutron velocity  $|v| = |v_0| \exp\left\{-\frac{1}{2}u\right\}$ , where  $v_0$  is an arbitrary reference speed), and direction  $\Omega$ .

Spanier and Gelbard (57) characterize the transport kernel  $T$  by stating that, for a particle leaving a collision (or the source) at phase point  $(\underline{r}', \underline{U})$ , the expected number of next collisions in the spatial volume  $V$  is:

$$\int_V T(\underline{r}' \rightarrow \underline{r}, \underline{U}) d\underline{r} \quad (\text{A.1})$$

The collision kernel  $C$  is similarly defined so that, for a particle entering a collision at  $(\underline{r}, \underline{U}')$ , the expected number of particles leaving the collision in the lethargy volume  $W$  is:

$$\int_W C(\underline{U}' \rightarrow \underline{U}, \underline{r}) d\underline{U} \quad (\text{A.2})$$

Therefore,  $C$  can be seen as the probability density of the individual transition  $\underline{U}' \rightarrow \underline{U}$  and  $T$  can be seen as the probability density of the individual transition  $\underline{r}' \rightarrow \underline{r}$ .

In the case of a homogeneous medium with different isotopes  $i$ , the macroscopic total cross-section  $\Sigma_t(\underline{r}', u) = \Sigma_t(u) = \sum_i \Sigma_{ti}(u)$  and the macroscopic scattering cross-section  $\Sigma_s(\underline{r}', u) = \Sigma_s(u) = \sum_i \Sigma_{si}(u)$  are constant on the trajectory  $\underline{r}' \rightarrow \underline{r}$ .

The distribution of interaction points of neutrons on the trajectory  $\underline{r}' \rightarrow \underline{r}$  is:

$$\Sigma_t(u) \exp \left\{ -\Sigma_t(u) \cdot |\underline{r} - \underline{r}'| \right\} \quad (\text{A.3})$$

To select the scattering collisions, the interaction distribution has to be corrected by  $\frac{\Sigma_s(u)}{\Sigma_t(u)}$  and the transport kernel  $T$  becomes:

$$T(\underline{r}' \rightarrow \underline{r}, U) = \Sigma_s(u) \exp \left\{ -\Sigma_t(u) \cdot |\underline{r} - \underline{r}'| \right\} \quad (\text{A.4})$$

In an individual case a next collision point may be selected from the normalized transport kernel by means of a random generator  $rg$  ( $0 < rg < 1$ ):

$$rg = \int_0^p \frac{T(\underline{r}' \rightarrow \underline{r}, U)}{\int_0^L T(\underline{r}' \rightarrow \underline{r}, U) d|\underline{r} - \underline{r}'|} d|\underline{r} - \underline{r}'| \quad (\text{A.5})$$

where  $L$  is the maximum available track length and  $p$  is the selected distance  $|\underline{r} - \underline{r}'|$ . The "weight" of the neutron has to be corrected by the normalization factor:

$$\int_0^L \Sigma_s(u) \exp \left\{ -\Sigma_t(u) |\underline{r} - \underline{r}'| \right\} d|\underline{r} - \underline{r}'| \quad (\text{A.6})$$

(N.B. Formally, as indicated by formula (A.1), the transport kernel should be integrated over the space volume and it should be written:

$$T'(\underline{r}' \rightarrow \underline{r}, \underline{U}) = \Sigma_s(u) \exp\left\{-\Sigma_t(u) \cdot |\underline{r} - \underline{r}'|\right\} \frac{\delta\left(\frac{r-r'}{|\underline{r}-\underline{r}'|} - \frac{U}{|U|}\right)}{|\underline{r}-\underline{r}'|^2} \quad (\text{A.7})$$

With

$$d\underline{r} = |\underline{r} - \underline{r}'|^2 d|\underline{r} - \underline{r}'| d\Omega \quad (\text{A.8})$$

the number of scattering collisions in the space volume  $V$  is :

$$\begin{aligned} \int_V T'(\underline{r}' \rightarrow \underline{r}, \underline{U}) d\underline{r} &= \int_0^{\mathcal{P}} d|\underline{r} - \underline{r}'| \int_0^{4\pi} d\Omega \cdot T'(\underline{r}' \rightarrow \underline{r}, \underline{U}) \cdot |\underline{r} - \underline{r}'|^2 \\ &= \int_0^{\mathcal{P}} T(\underline{r}' \rightarrow \underline{r}, \underline{U}) d|\underline{r} - \underline{r}'| \end{aligned} \quad (\text{A.9})$$

where the  $\delta$ -function couples the transport kernel to the flight direction of the neutron.

Formalisms of this kind will not be mentioned in the following.)

After selection of the next collision point, the transition of lethargy and direction is determined by means of the collision kernel  $C$ .

The collision kernel  $C$  may be represented explicitly as:

$$C(\underline{U}' \rightarrow \underline{U}, \underline{r}) = \sum_i k_i C_i(\underline{U}' \rightarrow \underline{U}, \underline{r}) \quad (\text{A.10})$$

where  $k_i$  denotes the probability of a scattering collision with isotope  $i$ , and  $C_i$  is the corresponding collision kernel.  $k_i$  can be represented as:

$$k_i = \frac{\Sigma_{si}(u')}{\sum_i \Sigma_{si}(u')} \quad (\text{A.11})$$

Selection of the isotope  $i$  to be collided with, can be made by means of the random generator  $rg$  ( $0 < rg < 1$ ):

$$\sum_{n=0}^{i-1} k_n \leq rg < \sum_{n=0}^i k_n \quad \text{with } k_0 = 0 \quad (\text{A.12})$$

The collision kernel  $C_i$  can be found by deriving the frequency function for elastic collision. The frequency function in lethargy is defined by:

$$g_i(u' \rightarrow u) du \equiv \text{fraction of all scattering collisions which result in the final lethargy range } u \text{ to } u+du, \text{ where } u' \leq u \leq u' + \ln \frac{1}{\alpha_i} \quad (\text{A.13})$$

With

$$\alpha_i = \left( \frac{A_i - 1}{A_i + 1} \right)^2 \quad (\text{A.14})$$

and  $A_i$  is the mass number of isotope  $i$ .

Meghreblian (49) gives a full derivation for the case of isotropy in the centre-of-mass system, and shows that:

$$g_i(u' \rightarrow u) du = \frac{\exp\{-(u-u')\}}{1-\alpha_i} du \quad (\text{A.15})$$

Since all possible transitions from  $u'$  to any  $u$  on the interval  $u' \leq u \leq u' + \ln \frac{1}{\alpha_i}$  are permissible, the individual transition  $u' \rightarrow u$  has to be selected from a kernel  $C_i$ , which is normalized to unity.

Apparently, formula (A.15) is already normalized:

$$\int_{u'}^{u'+\ln \frac{1}{\alpha_i}} g_i(u' \rightarrow u) du = 1 \quad (\text{A.16})$$

So  $C_i$  can be put equal to  $g_i$  :

$$C_i(\underline{U}' \rightarrow \underline{U}, \underline{r}) = \frac{\exp\{-(u-u')\}}{1-\alpha_i} \quad (\text{A.17})$$

Another way to write down  $C_i$ , which will turn out to be useful for the analogy to the backward case, is:

$$C_i(\underline{U}' \rightarrow \underline{U}, \underline{r}) = \frac{\Sigma_s(u' \rightarrow u)}{\int_{u'}^{u'+\ln \frac{1}{\alpha_i}} \Sigma_s(u' \rightarrow u) du} = \frac{\Sigma_s(u')g(u' \rightarrow u)}{\int_{u'}^{u'+\ln \frac{1}{\alpha_i}} \Sigma_s(u')g(u' \rightarrow u) du} \quad (\text{A.18})$$

Apparently  $C_i$  can be seen as the quotient of the differential scattering cross-section  $\Sigma_s(u' \rightarrow u)$  and the integral scattering cross-section.

Selection of lethargy  $u$  after collision with isotope  $i$  can be made from  $C_i$  by means of the random generator  $rg$  ( $0 < rg < 1$ ):

$$rg = \int_{u'}^u \frac{\exp\{-(u''-u')\}}{1-\alpha_i} du'' \quad (\text{A.19})$$

To be able to formulate the normal forward transition probability from a plane source  $S_0$ , with strength  $Q(\underline{s}'_0, \underline{U}'_0)$ , where  $\underline{s}'_0$  indicates the two coordinates of the source plane to a plane target  $S_t$  (see Fig. A.1), some new variables are introduced.

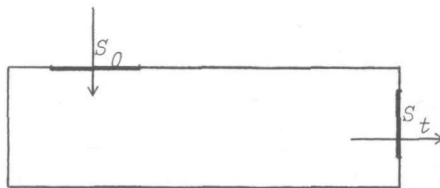


Fig. A.1 Medium with plane source  $S_0$  and plane target  $S_t$

With  $\phi(\underline{r}, \underline{U})$  as the neutron flux density, the collision density  $\psi$  of neutrons entering collision is related via:

$$\psi(\underline{r}, \underline{U}) = \Sigma_t(\underline{r}, u) \phi(\underline{r}, \underline{U}) \quad (\text{A.20})$$

The Boltzmann equation for the neutron transport can be written as:

$$\psi(\underline{r}, \underline{U}) = \iint \psi(\underline{r}', \underline{U}') C(\underline{U}' \rightarrow \underline{U}, \underline{r}) T(\underline{r}' \rightarrow \underline{r}, \underline{U}) d\underline{U}' d\underline{r}' + \int Q(\underline{r}', \underline{U}') T(\underline{r}' \rightarrow \underline{r}, \underline{U}) d\underline{r}' \quad (\text{A.21})$$

With  $\chi(\underline{r}', \underline{U})$  as the density of neutrons leaving collision at phase point  $(\underline{r}', \underline{U})$ ,  $\psi$  can be written:

$$\psi(\underline{r}, \underline{U}) = \int \chi(\underline{r}', \underline{U}) T(\underline{r}' \rightarrow \underline{r}, \underline{U}) d\underline{r}' \quad (\text{A.22})$$

where  $\chi(\underline{r}, \underline{U})$  is found from:

$$\begin{aligned} \chi(\underline{r}, \underline{U}) &= \int \psi(\underline{r}, \underline{U}') C(\underline{U}' \rightarrow \underline{U}, \underline{r}) d\underline{U}' + Q(\underline{r}, \underline{U}) \\ &= \int \chi(\underline{r}', \underline{U}') T(\underline{r}' \rightarrow \underline{r}, \underline{U}') C(\underline{U}' \rightarrow \underline{U}, \underline{r}) d\underline{r}' d\underline{U}' + Q(\underline{r}, \underline{U}) \quad (\text{A.23}) \end{aligned}$$

The transition probability  $\alpha$  can be seen as the quotient of the number of neutrons leaving the medium via  $(S_t, U_t)$  and the number of neutrons having entered it via  $(S_o, U_o)$ :

$$\alpha = \frac{\int_{U_t} \int_{S_t} \left[ \int_V \chi(\underline{r}, \underline{U}) \exp\{-\Sigma_t(u) \cdot |\underline{s}'_t - \underline{r}|\} d\underline{r} \right] d\underline{s}'_t d\underline{U}'_t}{\int_{U_o} \int_{S_o} Q(\underline{s}'_o, \underline{U}'_o) d\underline{s}'_o d\underline{U}'_o} \quad (\text{A.24})$$

(For simplicity the  $\delta$ -function, which should couple  $\underline{U}$  and  $\underline{s}'_t - \underline{r}$ , has been neglected)  $V$  is the space volume, and  $|\underline{s}'_t - \underline{r}|$  represents the last track before leaving the medium.

With  $n$  as a discrete index, representing the collision number,  $\chi$  may be written as a sum:

$$\chi(\underline{r}, \underline{U}) = \sum_{n=0}^{\infty} \chi_n(\underline{r}, \underline{U}) \quad (\text{A.25})$$

where  $\chi_n$  is the density of particles resulting from collision  $n$ , with

$$\chi_0(\underline{r}, \underline{U}) = Q(\underline{r}, \underline{U}) \quad (\text{A.26})$$

$$\chi_1(\underline{r}, \underline{U}) = \int_{U_0} \int_{S_0} Q(\underline{s}'_0, \underline{U}'_0) T_1 \cdot C_1 \frac{d\underline{s}'_0}{d\underline{U}'_0} \quad (\text{A.27})$$

$$\chi_n(\underline{r}, \underline{U}) = \int \int \chi_{n-1}(\underline{r}', \underline{U}') T_n \cdot C_n \frac{d\underline{r}_{-n-1}}{d\underline{U}_{-n-1}} \quad (\text{A.28})$$

$$n = 2, 3, \dots$$

with

$$T_1 = T(\underline{s}_0 \rightarrow \underline{r}_1, \underline{U}'_0) \text{ and } T_n = T(\underline{r}_{-n-1} \rightarrow \underline{r}_n, \underline{U}_{-n-1})$$

and

$$C_1 = C(\underline{U}'_0 \rightarrow \underline{U}_1, \underline{r}_1) \text{ and } C_n = C(\underline{U}_{-n-1} \rightarrow \underline{U}_n, \underline{r}_n)$$

From the expressions (A.26), (A.27) and (A.28) it follows that  $\chi_n$  can be found with the usual forward Monte Carlo technique by starting neutrons from the source and by repeating  $n$  times a random selection from the transport kernel and the collision kernel.

$\chi_n$  can be written:

$$\chi_n(\underline{r}_n, \underline{U}_n) = \iiint \dots \int Q(\underline{s}'_0, \underline{U}'_0) T_1 C_1 T_2 C_2 \dots T_n C_n \frac{d\underline{s}'_0}{d\underline{U}'_0} \frac{d\underline{r}_{-1}}{d\underline{U}_{-1}} \dots \frac{d\underline{r}_{-n-1}}{d\underline{U}_{-n-1}} \quad (\text{A.29})$$



In analogy to the usual forward Monte Carlo technique it will be shown that it is possible to select neutron tracks starting from the target, which is now called a backward source with strength  $Q^*(\underline{s}_t, \underline{U}_t)$  and using a backward transport kernel  $T^*(\underline{r} \rightarrow \underline{r}', \underline{U})$  and a backward collision kernel  $C^*(\underline{U} \rightarrow \underline{U}', \underline{r}')$ . The latter two can be derived from the usual forward neutron properties, using Bayes's rule for the probability of causes (58). The kernel  $T^*$  is used to select possible previous neutron transport trajectories, and  $C^*$  is used to select possible previous neutron lethargy and direction. It will turn out that the probability density of selecting an

the probability density of selecting the same neutron track from the source to the target.

To simplify the use of the expressions, the new notional words "backtron" and "upscatter collision" are introduced. "Backtrons" are the virtual particles having the property to describe the possible causes of perceived neutrons. And "upscatter collision" stands for the transition event of a backtron in lethargy and direction. (N.B. The use of the word backtron has been suggested by Mr. H. van Dam)

*The backward collision kernel*

Consider a population of events  $E_k$ .  $E_k$  is described by the fact that a neutron enters an infinitely small volume element around the space point  $\underline{r}$ , in the small lethargy group  $\Delta u_k$  around  $u_k$ . The a priori probability per unit lethargy of the entrance occurring in the lethargy element  $\Delta u_k$  is equal for each element. Now a subpopulation of events  $E_k$  for each  $k$  is defined by the fact that the entering neutron makes an elastic collision with isotope  $i$  at  $\underline{r}$ , which changes the lethargy of the neutron into the interval  $\Delta u_l$  around  $u_l$ , with the conditional probability  $P\{L_l|E_k\}$ . The size of this subpopulation in each group of entrance  $\Delta u_k$  is determined by  $\Sigma_S(u_k)dx$ , where  $dx$  is a small line element around  $\underline{r}$  in the flight direction of the neutron. The probability  $P\{E_k\}$  for an event  $E_k$  of occurring and of belonging to the subpopulation mentioned is given by:

$$P\{E_k\} = \Sigma_S(u_k) dx \Delta u_k \quad (A.30)$$

The conditional probability  $P\{L_l|E_k\}$  of the transition from  $\Delta u_k$  to  $\Delta u_l$  is given by the frequency function in lethargy:

$$P\{L_l|E_k\} = \frac{\exp\{-(u_l-u_k)\}}{1-\alpha_i} \Delta u_l \quad (A.31)$$

If the lethargy interval of a neutron leaving the subpopulation of events is given to be  $\Delta u_l$  then with Bayes's rule it is possible to

find the conditional probability  $P\{E_k | L_l\}$ :

$$P\{E_k | L_l\} = \frac{P\{L_l | E_k\} \cdot P\{E_k\}}{\sum_j P\{L_l | E_j\} \cdot P\{E_j\}} = \frac{\frac{\exp\{-(u_l - u_k)\}}{1 - \alpha_i} \Delta u_l \cdot \Sigma_s(u_k) dx \Delta u_k}{\sum_j \frac{\exp\{-(u_l - u_j)\}}{1 - \alpha_i} \Delta u_l \cdot \Sigma_s(u_j) dx \Delta u_j}$$

(A.32)

See also Fig. A.2.

The normalized backward collision kernel may be looked upon as the probability density of the individual neutron transition from  $u_k$  to  $u_l$ , relative to all possible neutron transitions from any  $u_j$  on the interval  $u_l - \ln \frac{1}{\alpha_i} \leq u_j \leq u_l$ , resulting in  $u_l$ . As all possible transitions from this interval of  $u_j$  to  $u_l$  are permissible, and since the properties of the medium are isotropic,  $C_i^*$  has to be a normalized kernel and can be found from  $P\{E_k | L_l\}$  in the limit of  $\Delta u_k \rightarrow 0$  and the maximum number of  $j \rightarrow \infty$ :

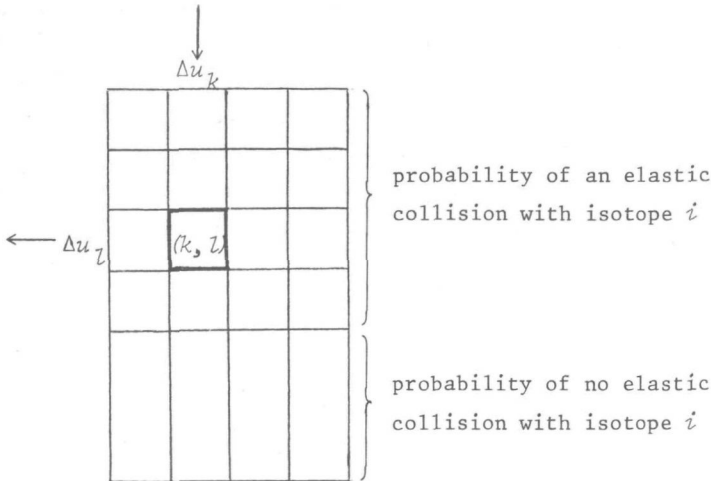


Fig. A.2 Population of events  $E_k$  ( $k=1, 2, 3, \dots$ ) at point  $\underline{r}$ . Each mesh  $(k, l)$  of the subpopulation indicates the transition probability  $P\{E_k\} \cdot P\{L_l | E_k\}$  of a neutron of making an elastic collision with isotope  $i$  in lethargy group  $\Delta u_k$  and of leaving the collision in lethargy group  $\Delta u_l$ .

$$C_i^*(\underline{U} \rightarrow \underline{U}', \underline{r}) du_k = \frac{\Sigma_{si}(u_k) \cdot \frac{\exp\{-(u_l - u_k)\}}{1 - \alpha_i} du_k}{\int_{u_l - \ln \frac{1}{\alpha_i}}^{u_l} \Sigma_{si}(u_j) \frac{\exp\{-(u_l - u_j)\}}{1 - \alpha_i} du_j} \quad (\text{A.33})$$

So  $C_i^*$  is again the quotient of a differential scattering cross-section and the integral scattering cross-section integrated on the interval of possible lethargy of origin of the neutron.

With the definition

$$\Sigma_i^*(u) \equiv \int_{u - \ln \frac{1}{\alpha_i}}^u \Sigma_s(u') \frac{\exp\{-(u - u')\}}{1 - \alpha_i} du' \quad (\text{A.34})$$

and

$$\Sigma^*(u) = \sum_i \Sigma_i^*(u) \quad (\text{A.35})$$

(the use of the symbol  $\Sigma^*$  has been introduced by Eriksson and Kalos (59)) the backward collision kernel for upscatter collision with isotope  $i$  becomes:

$$C_i^*(\underline{U} \rightarrow \underline{U}', \underline{r}) = \frac{\Sigma_{si}(u')}{\Sigma_i^*(u)} \frac{\exp\{-(u - u')\}}{1 - \alpha_i} \quad (\text{A.36})$$

Now the composite backward collision kernel  $C^*$  may be represented by:

$$C^*(\underline{U} \rightarrow \underline{U}', \underline{r}) = \sum_i k_i^*(u) C_i^*(\underline{U} \rightarrow \underline{U}', \underline{r}) \quad (\text{A.37})$$

with

$$k_i^*(u) = \frac{\Sigma_i^*(u)}{\Sigma^*(u)} \quad (\text{A.38})$$

and the isotope to be collided with can be selected with the random generator  $rg$  ( $0 < rg < 1$ ):

$$\sum_{n=0}^{i-1} k_n^*(u) \leq rg < \sum_{n=0}^i k_n^*(u) \quad \text{with } k_0^*(u) = 0 \quad (\text{A.39})$$

Finally, lethargy  $u'$ , after the upscatter collision, may be selected from  $C_i^*$  :

$$rg = \int_{u'}^u \frac{\Sigma_{si}(u'')}{\Sigma_i^*(u)} \frac{\exp\{-(u-u'')\}}{1-\alpha_i} du'' \quad (\text{A.40})$$

The characterization of the backward collision kernel in the sense of formula (A.2) is quite analogous to the forward case.

### *The backward transport kernel*

Consider a population of possible neutron transportations on the lethargy level  $u$ , on a line with coordinate  $x$ . The transportations have two properties.

1. A neutron transportation does take place after generation of the neutron on the small line element  $\Delta x_k$ , around  $x_k$ , with a probability  $P\{E_k\}$ .

Whether the neutron generation, from a scattering event, takes place or not is determined by the integral scattering cross-section  $\Sigma^*(u)$ , for all scattering events resulting in lethargy  $u$ . (For the definition of  $\Sigma^*(u)$  see formulae (A.34) and (A.35)).

The a priori probability per unit length of a neutron being generated on the element  $\Delta x_k$  is equal for each line element. So:

$$P\{E_k\} = \Sigma^*(u) \cdot \Delta x_k \quad (\text{A.41})$$

2. The neutron transportation started from  $\Delta x_k$  has the conditional probability  $P\{L_l | E_k\}$  of ending on the small line element  $\Delta x_l$  around  $x_l$ .  $P\{L_l | E_k\}$  is given by the forward interaction frequency function:

$$P\{L_l | E_k\} = \exp\{-\Sigma_t(u) \cdot |x_l - x_k|\} \cdot \Sigma_t(u) \Delta x_l \quad (\text{A.42})$$

Now using Bayes's rule, it is possible to find the conditional probability  $P\{E_k | L_l\}$  :

$$P\{E_k | L_l\} = \frac{P\{L_l | E_k\} \cdot P\{E_k\}}{\sum_j P\{L_l | E_j\} \cdot P\{E_j\}} = \frac{\exp\{-\Sigma_t(u) |x_l - x_k|\} \cdot \Sigma_t(u) \Delta x_l \cdot \Sigma^*(u) \Delta x_k}{\sum_j \exp\{-\Sigma_t(u) |x_l - x_j|\} \cdot \Sigma_t(u) \Delta x_l \cdot \Sigma^*(u) \Delta x_j} \quad (\text{A.42})$$

where the sum over  $j$  indicates all possible points of origin on  $x$ . The normalized backward transport kernel  $Tn^*$  may be looked upon as the probability density for the individual neutron transportation from  $x_k$  to  $x_l$ , relative to all possible neutron transportations from any point on  $x$  to  $x_l$ . So  $Tn^*$  can be found from  $P\{E_k | L_l\}$  in the limit of  $\Delta x_k \rightarrow 0$  and the maximum number of  $j \rightarrow \infty$ :

$$Tn^*(x_k \rightarrow x_l, u) dx_k = \frac{\Sigma^*(u) \cdot \exp\{-\Sigma_t(u) \cdot |x_l - x_k|\} dx_k}{\int_0^L \Sigma^*(u) \cdot \exp\{-\Sigma_t(u) \cdot |x_l - x_j|\} dx_j} \quad (\text{A.43})$$

where  $L$  is the maximum available track length on  $x$ .

Apparently, the normalized kernel  $Tn^*$  is equal to the normalized forward transport kernel used as integrand in formula (A.5). In analogy to the forward transport kernel it is now possible to write down the unnormalized backward transport kernel, which is the probability density of an individual backtron transportation resulting in an upscatter event:

$$T^*(\underline{r} \rightarrow \underline{r}', U) = \Sigma^*(u) \exp\{-\Sigma_t(u) |\underline{r}' - \underline{r}|\} \quad (\text{A.44})$$

In the individual case a next upscatter collision point may be selected from the normalized backward transport kernel, using the random generator  $rg$  ( $0 < rg < 1$ ):

$$rg = \int_0^P \frac{T^*(\underline{r} \rightarrow \underline{r}', U)}{\int_0^L T^*(\underline{r} \rightarrow \underline{r}', U) d|\underline{r}' - \underline{r}|} d|\underline{r}' - \underline{r}| \quad (\text{A.45})$$

and the weight of the backtron has to be corrected by the normalization factor:

$$\int_0^L \Sigma^*(u) \exp\{-\Sigma_t(u) |\underline{r}' - \underline{r}|\} d|\underline{r}' - \underline{r}| = \frac{\Sigma^*(u)}{\Sigma_t(u)} [1 - \exp\{-\Sigma_t(u) \cdot L\}] \quad (\text{A.45}')$$

The characterization of the backward transport kernel in the sense of formula (A.1) is again quite analogous to the forward case.

Vayssier (60) gives a derivation of the same kernels  $T^*$  and  $C^*$  from the adjoint neutron transport theory, and Eriksson (59) and Levitt (61) also give essentially the same kernels.

To be able to find the quantity of interest, i.e. the forward transition probability  $\alpha$  of formula (A.24), from the backward Monte Carlo program, a backward transition probability  $\alpha^*$  is defined as the quotient of the number of backtrons leaving the medium via  $(S_o, U_o)$  and the number of backtrons having entered it via  $(S_t, U_t)$ . With the new variable  $\chi^*(\underline{r}, \underline{U})$  as the density of backtrons leaving the upscatter collision at phase point  $(\underline{r}, \underline{U})$ ,  $\alpha^*$  can be written:

$$\alpha^* = \frac{\int_{U_o} \int_{S_o} \left[ \int_V \chi^*(\underline{r}, \underline{U}) \cdot \exp\{-\Sigma_t(u) \cdot |\underline{s}' - \underline{r}|\} d\underline{r} \right] d\underline{s}' dU'_o}{\int_{U_t} \int_{S_t} Q^*(\underline{s}'_t, \underline{U}'_t) d\underline{s}'_t dU'_t} \quad (\text{A.46})$$

where  $V$  is the space volume and  $|\underline{s}' - \underline{r}|$  represents the last track before leaving the medium.

Again as in the forward case, with  $n$  as a discrete index representing the upscatter collision number,  $\chi^*$  may be written as a sum:

$$\chi^*(\underline{r}, \underline{U}) = \sum_{n=0}^{\infty} \chi_n^*(\underline{r}, \underline{U}) \quad (\text{A.47})$$

where  $\chi_n^*$  is the density of backtrons resulting from upscatter collision  $n$ , with:

$$\chi_0^*(\underline{r}, \underline{U}) = Q^*(\underline{r}, \underline{U}) = Q^*(\underline{s}_t, \underline{U}_t) \quad (\text{A.48})$$

$$\chi_1^*(\underline{r}, \underline{U}) = \int_{U_t} \int_{S_t} Q^*(\underline{s}'_t, \underline{U}'_t) T_1^* C_1^* d\underline{s}'_t d\underline{U}'_t \quad (\text{A.49})$$

where

$$T_1^* = T^*(\underline{s}'_t \rightarrow \underline{r}_1, \underline{U}'_t) \text{ and } C_1^* = C^*(\underline{U}'_t \rightarrow \underline{U}, \underline{r}_1)$$

and with

$$T_n^* = T^*(\underline{r}_{n-1} \rightarrow \underline{r}_n, \underline{U}_{n-1}) \text{ and } C_n^* = C^*(\underline{U}_{n-1} \rightarrow \underline{U}_n, \underline{r}_n) \quad n = 2, 3, \dots$$

$$\begin{aligned} \chi_n^*(\underline{r}_n, \underline{U}_n) &= \iint \chi_{n-1}^*(\underline{r}_{n-1}, \underline{U}_{n-1}) T_n^* C_n^* d\underline{r}_{n-1} d\underline{U}_{n-1} = \\ &= \iint \dots \iint Q^*(\underline{s}'_t, \underline{U}'_t) T_1^* C_1^* T_2^* C_2^* \dots T_n^* C_n^* d\underline{s}'_t d\underline{U}'_t d\underline{r}_{-1} d\underline{U}_{-1} \dots d\underline{r}_{n-1} d\underline{U}_{n-1} \end{aligned} \quad (\text{A.50})$$

Since  $C_j^*$  and  $C_{n+1-j}$  describe the same lethargy transition and  $T_j^*$  describes the same transport as  $T_{n+2-j}$ , the upscatter collision indices may be renumbered, corresponding to the forward collision indices:

$$\chi_n^*(\underline{r}, \underline{U}) = \iint \dots \iint Q^*(\underline{s}'_t, \underline{U}'_t) T_{n+1}^* C_n^* T_n^* C_{n-1}^* \dots T_2^* C_1^* d\underline{s}'_t d\underline{U}'_t d\underline{r}_{n+1} d\underline{U}_{n+1} \dots d\underline{r}_2 d\underline{U}_2 \quad (\text{A.51})$$

where  $n+1$  indicates the track number from the backward source to the first upscatter collision points. Now, from formulae (A.44), (A.36), (A.37), (A.38) it follows that

$$\begin{aligned} T_j^* C_{j-1}^* &= \Sigma^*(u_{j-1}) \exp[-\Sigma_t(u_{j-1}) \cdot |r_{j-1} - r_j|] \cdot \int_i \frac{\Sigma_i^*(u_{j-1}) \Sigma_{si}(u_{j-2})}{\Sigma^*(u_{j-1}) \Sigma_i^*(u_{j-1})} \\ &\cdot \frac{\exp\{-(u_{j-1} - u_{j-2})\}}{1 - \alpha_i} = \exp[-\Sigma_t(u_{j-1}) |r_{j-1} - r_j|] \cdot \int_i \Sigma_{si}(u_{j-2}) \\ &\cdot \frac{\exp\{-(u_{j-1} - u_{j-2})\}}{1 - \alpha_i} \quad 2 \leq j \leq n \end{aligned} \quad (\text{A.52})$$

From formulae (A.4), (A.10), (A.11), (A.17) follows:

$$T_j^* C_{j-1} = \Sigma_s(u_{j-1}) \exp\{-\Sigma_t(u_{j-1}) \cdot |r_j - r_{j-1}|\} \cdot \frac{\Sigma_s i(u_{j-2})}{\Sigma_s(u_{j-2})} \cdot \frac{\exp\{-(u_{j-1} - u_{j-2})\}}{1 - \alpha_i} \quad (\text{A.53})$$

So:

$$T_j^* C_{j-1}^* = \frac{\Sigma_s(u_{j-2})}{\Sigma_s(u_{j-1})} T_j^* C_{j-1} \quad (\text{A.54})$$

and

$$T_n^* C_{n-1}^* \cdots T_2^* C_1^* = \frac{\Sigma_s(u_0)}{\Sigma_s(u_{n-1})} T_n^* C_{n-1} \cdots T_2^* C_1 \quad (\text{A.55})$$

With

$$\begin{aligned} T_{n+1}^* C_n^* &= \exp\{-\Sigma_t(u_n) \cdot |r_n - r_{n+1}|\} \cdot \Sigma_s i(u_{n-1}) \frac{\exp\{-(u_n - u_{n-1})\}}{1 - \alpha_i} = \\ &= \exp\{-\Sigma_t(u_n) \cdot |r_n - r_{n+1}|\} \cdot \Sigma_s(u_{n-1}) \cdot C_n \end{aligned} \quad (\text{A.56})$$

$\chi_n^*$  becomes:

$$\begin{aligned} \chi_n^*(r_n, u_n) &= \left( \int \cdots \int \right) Q^*(s'_t, u'_t) \Sigma_s(u_0) \exp\{-\Sigma_t(u_n) \cdot |r_n - r_{n+1}|\} \cdot C_n \cdot T_n \cdot \\ &C_{n-1} \cdots T_2 \cdot C_1 \frac{ds'_t du'_t dr_{-n+1} du_n \cdots dr_{-2} du_{-1}}{dt} \end{aligned} \quad (\text{A.57})$$

Comparison of  $a^*$  in (A.46) with  $a$  in (A.24) can be made by comparing the terms containing  $\chi_n^*$  and  $\chi_n$ :

$$a_n^* = \frac{\int_{U_0} \int_{S_0} \left( \int \cdots \int \right) Q^*(s'_t, u'_t) \Sigma_s(u_0) \exp\{-\Sigma_t(u_n) \cdot |r_n - r_{n+1}|\} C_n T_n C_{n-1} \cdots T_2 C_1}{\int_{U_t} \int_{S_t} Q^*(s'_t, u'_t) \frac{ds'_t du'_t}{dt} \frac{ds'_t du'_t \cdots dr_{-2} du_{-1}}{dt} \cdot \exp\{-\Sigma_t(u_0) \cdot |s'_0 - r_{-1}|\} \frac{ds'_0 du'_0}{dt}} \quad (\text{A.58})$$

with

$$a^* = \sum_{n=0}^{\infty} a_n^* \quad (\text{A.59})$$

As

$$T_1 = \Sigma_s(u_o) \exp\{-\Sigma_t(u_o) \cdot |s'_o - r_1|\} \quad (\text{A.60})$$

$a_n^*$  becomes:

$$a_n^* = \frac{\int_{U'_o S'_o} \dots \int_{U'_t S'_t} Q^*(s'_t, U'_t) \cdot \exp\{-\Sigma_t(u_n) \cdot |r_n - r_{n+1}|\} C_n^{T_n} \dots C_1^{T_1} ds'_t dU'_t \cdot ds'_o dU'_o}{\int_{U'_t S'_t} \int_{U'_o S'_o} Q^*(s'_t, U'_t) ds'_t dU'_t} \quad (\text{A.61})$$

and  $a_n$  can be written:

$$a_n = \frac{\int_{U'_t S'_t} \dots \int_{U'_o S'_o} Q(s'_o, U'_o) T_1 C_1 \dots T_n C_n \cdot \exp\{-\Sigma_t(u_n) \cdot |r_{n+1} - r_n|\} \cdot ds'_o dU'_o \cdot ds'_t dU'_t}{\int_{U'_o S'_o} \int_{U'_o S'_o} Q(s'_o, U'_o) ds'_o dU'_o} \quad (\text{A.62})$$

where

$$a = \sum_{n=0}^{\infty} a_n \quad (\text{A.63})$$

The integrand of the numerator of  $a_n^*$  can be seen as the product of the source strength  $Q^*$  and the probability density of an individual neutron track, which has been selected in backward direction.

Apparently, this probability density is equal to the probability density of the same individual neutron track, selected in forward direction, as can be seen from the integrand of the numerator of  $a$ . If the total neutron source in phase space is divided into small groups, so that  $Q$  can be put constant on one group  $(S_o, U_o)$ , and choosing  $Q^*$  constant on  $(U_t, S_t)$  it follows that

$$a_n = \frac{\int_{U'_t S'_t} ds'_t dU'_t}{\int_{U'_o S'_o} ds'_o dU'_o} a_n^* \quad (\text{A.64})$$

As relation (A.64) holds for all  $n \geq 0$ , it follows that

$$a = \frac{\Delta \text{ target}}{\Delta \text{ source}} a^* \quad (\text{A.65})$$

with

$$\Delta \text{ target} = \int_{U_t} \int_{S_t} \frac{ds'_t dU'_t}{-} \quad (\text{A.66})$$

and

$$\Delta \text{ source} = \int_{U_0} \int_{S_0} \frac{ds'_0 dU'_0}{-} \quad (\text{A.67})$$

The practical calculation of  $a^*$  can be done in different ways:

- Calculate separately  $\Sigma_i^*(u_j)$  for all energy groups  $j$  and all isotopes  $i$ .

The Monte Carlo program comprises the following procedures:

- select a backtron from  $Q^*(S_t, U_t)$
- select the next upscatter collision point from  $T^*$  (A.44) by means of (A.45) and correct the weight of the backtron by the normalization factor (A.45')
- select the isotope to be collided with from  $k_i^*$  (A.38) by means of (A.39)
- select the lethargy after the upscatter collision from  $C_i^*$  (A.36) by means of (A.40)
- repeat selection from  $T^*$ ,  $k_i^*$  and  $C_i^*$  until the backtron life is terminated by the "Russian roulette"
- repeat all procedures until the variance of  $a^*$  has been reduced sufficiently

If  $\Sigma_s(u)$  does not change much from one group to another, the use of  $\Sigma^*$  can be avoided without significant loss of speed of variance reduction, using the following procedures:

- select a backtron from  $Q^*(S_t, U_t)$
- select the next upscatter collision point from

$$T^{**} = \Sigma_s(u) \exp\{-\Sigma_t(u)|\underline{r}' - \underline{r}|\} \quad (\text{A.68})$$

by means of

$$rg = \int_0^p \frac{T^{**}(\underline{r} \rightarrow \underline{r}', U)}{\int_0^L T^{**}(\underline{r} \rightarrow \underline{r}', U) d|\underline{r}' - \underline{r}|} d|\underline{r}' - \underline{r}| \quad (A.69)$$

$0 < rg < 1$

- correct the weight of the backtron by the normalization factor:

$$\int_0^L T^{**}(\underline{r} \rightarrow \underline{r}', U) d|\underline{r}' - \underline{r}| \quad (A.70)$$

- select the isotope to be collided with from

$$k_i^{**} = \frac{\sum_i s_i(u)}{\sum_i s_i(u)} \quad (A.71)$$

by means of

$$\sum_{n=0}^{i-1} k_n^{**} \leq rg < \sum_{n=0}^i k_n^{**} \quad \text{with } k_0^{**} = 0 \quad (A.72)$$

$0 < rg < 1$

- select the lethargy  $u'$  after the upscatter collision from

$$C_i^{**} = \frac{\exp\{-(u-u')\}}{1-\alpha_i} \quad (A.73)$$

by means of

$$rg = \int_{u'}^u \frac{\exp\{-(u-u'')\}}{1-\alpha_i} du'' \quad 0 < rg < 1 \quad (A.74)$$

- correct the weight of the backtron by

$$\frac{\sum_i s_i(u')}{\sum_i s_i(u)} \quad (A.75)$$

$$\text{With } C^{**} = \sum_i k_i^{**} C_i^{**} \quad (A.76)$$

and formula (A.52) it can be seen that

$$\begin{aligned}
T_j^{**} C_{j-1}^{**} &= \Sigma_s(u_{j-1}) \exp\{-\Sigma_t(u_{j-1}) \cdot |\frac{r_{j-1}-r_j}{r_j}|\} \cdot \sum_i \frac{\Sigma_{si}(u_{j-1})}{\Sigma_s(u_{j-1})} \\
&\cdot \frac{\exp\{-(u_{j-1}-u_{j-2})\}}{1-\alpha_i} \cdot \frac{\Sigma_{si}(u_{j-2})}{\Sigma_{si}(u_{j-1})} = \\
&= \exp\{-\Sigma_t(u_{j-1}) \cdot |\frac{r_{j-1}-r_j}{r_j}|\} \cdot \sum_i \Sigma_{si}(u_{j-2}) \frac{\exp\{-(u_{j-1}-u_{j-2})\}}{1-\alpha_i} = \\
&= T_j^* C_{j-1}^* \tag{A.77}
\end{aligned}$$

- repeat selection from  $T^{**}$ ,  $k_i^{**}$  and  $C_i^{**}$  until the backtron life is terminated by the "Russian roulette"
- repeat all procedures until the variance of  $\alpha^*$  has been reduced sufficiently

If the medium is not homogeneous, there are no essential changes. If, for example, the medium consists of a number of different layers the total transport kernel is composed of several separate transport kernels for the individual homogeneous layers. The same treatment as in the usual forward Monte Carlo technique can be applied. The choice of the isotope to be collided with now depends on  $\underline{r}$ :

$$k_i^*(\underline{r}) = \frac{\Sigma_{si}(u, \underline{r})}{\sum_i \Sigma_{si}(u, \underline{r})} \tag{A.78}$$

If thermal neutrons are important, a separate treatment is necessary, because the collision kernels  $C$  and  $C^*$  no longer hold, owing to the relation between lethargy step and deflection angle being no longer unique.

Other types of neutron reactions, such as inelastic scattering and fission, can be treated likewise in an adjoint Monte Carlo program. See (59). They will be omitted here.

In general it may be stated that the use of a backward or adjoint Monte Carlo program as described here will give variance reduction, if the neutron source may be divided into larger phase groups than the target. For a more extensive treatment of the variance reduction the reader be referred to the literature (59,61).

## REFERENCES

### CHAPTER 1.

- (1) F. Storrer, A. Khairallah and J. Ozeroff (Euratom CEA, Cadarache), "Theoretical Aspects of the Measurement of the Doppler Coefficient in a Critical Facility", ANL-6792 (1963).
- (2) J. Ladet, I. Puig, L. Stevens, "Use of Rapsodie for the Measurement of the Doppler Coefficient of Fast Power Reactors", ANL-6792 (1963).
- (3) P.J. Persiani (A.N.L.), "Reactivity Coefficient Measurements in FARET", ANL-6792 (1963).
- (4) T.H. Springer and S.G. Carpenter, "Fast Spectrum Doppler Measurements", ANL-6792 (1963).
- (5) C.E. Till, R.A. Lewis and R.N. Hwang, "ZPR-6 Doppler Measurements and Comparisons with Theory", ANL-7320 (1966).
- (6) S.G. Carpenter et al., "Dependence of the Doppler Coefficient of Reactivity for Heavy Elements on Chemical Form, Surface-to-Mass Ratio, and Neutron Spectrum", ANL-7320 (1966).
- (7) G.J. Fischer et al., "Doppler Effect Measurements in Plutonium Fueled Fast Power Breeder Reactor Spectra", Nucl.Sci.Eng. 25, 37 (1966).
- (8) E.A. Fischer, "Interpretation of Doppler Coefficient Measurements in Fast Critical Assemblies", KFK-473, Kernforschungszentrum Karlsruhe, (1966).
- (9) P. Engelmann et al., "Initial Experiments in the Karlsruhe Fast Critical Facility SNEAK", KFK-471, Kernforschungszentrum Karlsruhe (1966).
- (10) R.E. Kaiser and J.M. Gasidlo, "On the Effect of Core Configuration on  $^{238}\text{U}$  Doppler Measurements in ZPPR-Assembly 2", Proc.Conf. on New Developments in Reactor Physics and Shielding" CONF 720901, pp 1006-15, (1972).
- (11) C.E. Till, "The Fast Neutron Doppler Effect", Proc. Conf. on New Developments in Reactor Physics and Shielding", CONF 720901 pp 1152-65, (1972).

- (12) P.H. Kier and M. Salvatores, "The Effect of Local Flux Distortions on the Doppler Effect of Small Fissile Samples", Nucl. Sci. Eng. 53, 479-82, (1974).
- (13) R.A. Karam and W.Y. Kato, "On the Discrepancy between Measured and Calculated Central Reactivity Coefficients", Nucl. Sci. Eng. 52, 201-8, (1973).
- (14) J.F. Meyer et al., "<sup>238</sup>U Doppler Reactivity Mapping in the FFTF Engineering Mockup Critical", Trans. Am. Nucl. Soc. 16, 270-2, (1973).
- (15) R.A. Harris (West Hanford), "Application of the Results of the SEFOR Doppler Experiments to FTR", Trans. Am. Nucl. Soc. 16, 281 (1973).
- (16) H.H. Hummel (A.N.L. 111), "Sensitivity studies of the Effect of Uncertainty in the <sup>238</sup>U(n,γ) and in the <sup>239</sup>Pu(n,f) and (n,γ) cross sections", CONF 710301, pp 65-71, (1971)
- (17) L. Barleon and E.A. Fischer, "Small Sample Doppler Effect Measurements and their Interpretation in Fast Reactor Spectra", Nucl. Sci. Eng. 47, 247-61, (1972).
- (18) J. Baughn and R. Sher (Stanford), "Measurement of the Doppler Effect in Thin Uranium Metal", Trans. Am. Nucl. Soc. 16, 318-19, (1973).
- (19) G.R. Pflasterer and R. Sher, "Activation Measurement of the Doppler Effect for <sup>238</sup>U Capture and <sup>235</sup>U Fission in a Fast Neutron Spectrum", Nucl. Sci. Eng. 30, 374 (1967).
- (20) G.R. Pflasterer, "Measurement of the Doppler Effect for Uranium-238 Capture and Uranium-235 Fission in a Fast Neutron Spectrum", PhD Thesis, Stanford University, 1966.
- (21) L.I. Tirén and I. Gustafsson, "Activation Doppler Measurements on <sup>238</sup>U and <sup>235</sup>U in Some Fast Reactor Spectra", AE-314, Aktiebologer, Atomenergi, Sweden (1968).
- (22) W.G. Davey and P.I. Amundson, "Activation Measurements of the Doppler Effect in <sup>238</sup>U in ZPR-3 Assembly 47 (SEFOR)", Trans. Am. Nucl. Soc. 9, 226 (1966).

- (23) E. Hellstrand, "Reactor Physics in the Resonance and Thermal Regions", Vol. II, p 151. A.J. Goodjohn and G.C. Pomraning (eds), M.I.T. Press, Cambridge, U.S.A. (1966).
- (24) W.K. Foell et al., "Pulsed Activation Techniques for the Measurement of Doppler Effects", Proc. Conf. on New Developments in Reactor Physics and Shielding. CONF 720901, pp 1016-32, (1972).
- (25) S.K. Bhattacharyya, W.K. Foell, "High Temperature Doppler Measurement Using the Pulsed Activation Technique", Trans. Am. Nucl. Soc. 17, 461-2, (1973).
- (26) L.I. Tirén, "Activation Doppler Measurements", NP 17908, Aktiebolaget Atomenergi, Sweden (1968).
- (27) H. Seufert and D. Stegemann, "Energy and Temperature Dependent Capture Measurements below 30 keV, Supporting Doppler Effect Calculations", KFK-631, Kernforschungszentrum Karlsruhe (1967).
- (28) L.S. Beller and W.H. Heneveld, "High Temperature Measurements of Doppler Effect in UC and UO<sub>2</sub> by Method of Temperature Cycled Reactivity Oscillation", NAA-SR-12501, Atomics International, Canoga Park, California, 1967.
- (29) F.C. Schoenig, Jr., and F.A. White, "The Temperature Dependence of epithermal Neutron Capture and Fission in U-235 Dioxide", Nucl. Sci. Eng. 37, 66-84 (1969).
- (30) Subin Banharnsupavat et al., "A New Technique for Measuring the Doppler Effect", Trans. Am. Nucl. Soc. 18, 332 (1974).
- (31) A.L. Dekker and H.R. Kleijn, "The Local Pile Oscillator as a Device for Measuring Epithermal Neutron Absorption", Nucl. Instr. & Meth. 55, 87-92, (1967).
- (32) A.L. Dekker, "The Local Pile Oscillator as a Device for Measuring Temperature Dependence in Epithermal Neutron Absorption". Thesis, Delft University of technology, Netherlands (1969).

CHAPTER 2.

- (33) P.W. Renaud, "Voorstudie om te komen tot een keuze van meetmethode voor het bepalen van het Doppler effect van enkele splijt- en kweekstoffen in snelle neutronenspektra", Athene 568, Eindhoven University of Technology (1969)
- (34) W.L. Zijp, "Kursusdiktaat Stralingsdetectie", Deel II: Statistiek, p 10, Petten, 1963.

CHAPTER 3.

- (35) P.F. Palmedo et al., "Effect of Hydrogen Content of Graphite in Fast Critical Experiments", Trans. Am. Nucl. Soc. 13, 253-4 (1970).
- (36) W.N Reynolds, "Physical Properties of Graphite", Elsevier Publishing Co. Ltd. London, 1968.
- (37) Charles L. Mantell, "Carbon and Graphite Handbook", John Wiley and Sons, Inc., New York, 1968.
- (38) W.L. Zijp, "Kursusdiktaat Stralingsdetectie", Deel II: Statistiek, p 47 e.v., Petten 1963.
- (39) J.J. Schmidt, "Neutron Cross Sections for Fast Reactor Materials", part I: evaluation, KFK 120 (EANDC-E-35U) Kernforschungszentrum, Karlsruhe (1966).
- (40) Reactor Handbook. Second Edition. Volume I: Materials, p 293, edited by C.R. Tipton, Jr., Interscience Publishers, Inc., New York, 1960.
- (41) E. Ryshkewitch, "Oxide Ceramics", p 411, Academic Press, New York and London, 1960.

CHAPTER 4.

- (42) E.D. Cashwell and C.J. Everett, "A practical manual on the Monte Carlo method for random walk problems", London, 1959.

- (43) J. Spanier and E.M. Gelbard, "Monte Carlo Principles and Neutron Transport Problems", Addison-Wesley Publishing Company, Reading, Massachusetts, 1969.
- (44) "Group Constants for Nuclear Reactor Calculations", edited by I.I. Bondarenko, New York, 1964.
- (45) J.J. Schmidt, "Neutron Cross Sections for Fast Reactor Materials", part I: evaluation (p A54, A56), KFK-120 (EANDC-E-35U), Kernforschungszentrum Karlsruhe (1966).
- (46) H. van Dam, "FAST ZOOM DELFT, a computer code in Algol for one dimensional multigroup neutron diffusion calculations", Delft, 1967. THD-RF-112.
- (47) H. van Dam, "Experimental and Theoretical Analysis of Fast Neutron Spectra", Thesis, Delft, 1971.

CHAPTER 5.

- (48) J. Montizaan and H. Ames, "Snelle neutronenspectrometrie met een stootprotonenspectrometer in de ATHENE-reactor te Eindhoven", Petten, September 1974. RCN-74-099. Personal communication.
- (49) R. Meghreblian and D. Holmes, "Reactor Analysis", ch.4, Mc Graw-Hill Book Company, Inc., New York, 1960.
- (50) J.J. Schmidt, "Neutron Cross Sections for Fast Reactor Materials", part II: Tables KFK-120, December 1962.
- (51) RICM - An IBM-7090 Code of Resonance Integral Calculation for Multiregion Lattice. JAERI 1134, Japan Atomic Energy Research Institute (Aug. 1967).
- (52) F. de Kruijf, (Interuniversitair Reactor Instituut Delft), personal communication.
- (53) F.C. Schoenig et al., "The Temperature Dependence to 1550 °C of the Effective Resonance Integral of Thorium Oxide Rods", Nucl.Sci.Eng. 26, 393-398 (1966).

- (54) L. Dresner, "Resonance Absorption in Nuclear Reactors", p. 33, Pergamon Press, 1960.
- (55) J.J. Schmidt, "Neutron Cross Sections for Fast Reactor Materials", part I: evaluation, p. D128, KFK-120 (1966).
- (56) R. Froelich and K. Ott, Nukleonik 8, 137 (1966).

#### APPENDIX

- (57) J. Spanier and E.M. Gelbard, "Monte Carlo Principles and Neutron Transport Problems", p. 57, Addison-Wesley Publishing Company, Massachusetts, 1969.
- (58) W. Feller, "An Introduction to Probability Theory and Its Applications", Vol. 1, p. 114, second edition, John Wiley & Sons, Inc., New York, 1965.
- (59) B. Eriksson et al. and M.H. Kalos, "Monte Carlo integration of the Adjoint Neutron Transport Equation", Nucl.Sci.Eng., 37, 410-422, 1969.
- (60) G. Vayssier, "Optimum Shielding against Neutron and Gamma Radiation", Thesis, Eindhoven University of Technology, to be published.
- (61) L. Levitt, J. Spanier, "A New Non-Multigroup Adjoint Monte Carlo Technique", Nucl.Sci.Eng., 37, 278-287, 1969.

LIST OF SYMBOLS

$A$	mass number	
$a$	transition probability	
$abs$	neutron absorption of sample	
$B$	transmission function of neutron filter	
$0 B_4C$	indication of unfiltered neutron spectrum	
$4 B_4C$	indication of neutron spectrum filtered by 4 mm $B_4C$	
$12 B_4C$	indication of neutron spectrum filtered by 12 mm $B_4C$	
$bg$	cumulative background fraction of reference signal $R_{abs}^0$	
$bicratio$	$R_{abs}/R_{sc}$	
$Bi-C$ scatterer	description on p. 24	
$C$	collision kernel	
$c12$	correction for deviation from correct position of dodecahedron	
$Cexp$	correction for sample expansion	
$emod$	correction for slowing down of neutrons in sample	
$D$	Doppler effect	
$DI$	detector integral	$s^{-1}$
$E$	energy	eV
	event	
$eff$	detector efficiency	
$exp$	oscillator expansion	mm
$g$	energy group indication	
$g(u' \rightarrow u)$	frequency function for elastic collision in lethargy	
$gun$	lowest group number	
$i$	isotope indication	
$k$	isotope selection kernel	
$L$	maximum available track length event	m

$l$	length, thickness	m
$m$	sample indication	
$mod$	see formula (3.8)	
$n$	molecule density	$\text{cm}^{-3}$
$P\{E_k\}$	probability of event $E_k$	
$P\{L_l E_k\}$	probability of event $L_l$ on condition of event $E_k$	
$p$	neutron track length	m
$primabs$	primary neutron absorption in sample	
$Q$	source strength	$\text{s}^{-1}$
$R$	detector signal with reference sample	$\text{s}^{-1}$
$\underline{r}$	space vector	
$r_i$	inner radius of graphite ball	cm
$r_o$	outer radius of graphite ball	cm
$ref_b$	$R_{abs}/W_{abs,o}$	
$ref_{sc}$	extra reference correction for scattered neutron fraction	
$rg$	random generator ( $0 < rg < 1$ )	
$s$	plane	
$\underline{s}$	plane vector	
$scfr$	scattered neutron fraction	
$secabs$	secondary neutron absorption in sample	
$T$	temperature	$\text{K}(^{\circ}\text{C})$
	transport kernel	
$t$	fraction of $\Phi_o$ passing sample without interaction	
$tr$	transmission function of sample	
$trf$	transmission factor	
$\underline{U}$	neutron speed vector	
$U$	fixed value of $\underline{U}$	
$u$	lethargy	
$V$	spatial volume	
$v$	neutron velocity	$\text{m s}^{-1}$
$W$	detector signal with unknown sample	$\text{s}^{-1}$

<i>wac</i>	background fraction caused by oven wall and air column behind sample	
<i>x</i>	line coordinate	m
$\alpha$	$(A-1)^2/(A+1)^2$	
	angle coordinate	rad
$\Delta$	difference	
<i>v</i>	angle coordinate	rad
$\theta_D$	Debye temperature	K
$\Sigma$	macroscopic cross-section	cm <sup>-1</sup>
$\sigma$	microscopic cross-section	b
$\tau$	insensitive time of detector	s
$\Phi(E)$	neutron flux	s <sup>-1</sup> eV <sup>-1</sup>
$\phi(E)$	neutron flux density	cm <sup>-2</sup> s <sup>-1</sup> eV <sup>-1</sup>
$\phi$	angle coordinate	rad
$\chi$	collision density of neutrons leaving collision	
$\psi$	collision density of neutrons entering collision	
$\underline{\Omega}$	neutron flight direction vector	

lower index

<i>a</i>	absorption
<i>abs</i>	<i>Bi-C</i> scatterer being present in graphite ball
<i>b</i>	beam
<i>c</i>	cold
<i>2c</i>	neutrons reentering sample
<i>col</i>	collimator
<i>eff</i>	effective
<i>g</i>	group number
<i>i</i>	isotope number
<i>inel</i>	inelastic
<i>k, l</i>	arbitrary number
<i>m</i>	measured

$n(1,2,..)$  collision number  
o neutrons leaving the graphite ball  
s scattering/source/start  
sc  $B\dot{i}$ -C scatterer being absent from graphite ball  
t total/target/true  
w warm  
o without sample/incident to sample/coming from source

upper index

o not corrected for background signal  
\* refers to backtron movement

## SUMMARY

The aim of this work is the design and the testing of a method of measuring the nuclear Doppler effect in intermediate and fast neutron spectra.

The experiments were carried out at the ATHENE reactor of the Eindhoven University of Technology.

Two starting points were used in the design of the system:

- the system had to be cheap and flexible;
- only simple geometries and neutron-physically well-known materials were to be applied to make the qualitative and quantitative measurement interpretations sufficiently reliable.

Of the existing methods, the reactivity oscillation method may be mentioned as the most sensitive. The interpretation of the results, however, is very complicated, so that the uncertainty of the final results may be of the order of tens of percents.

A second method is the activation analysis of irradiated Doppler samples. The inaccuracy of the measurements is of the order of 10%. The interpretation of the measurements is less complicated than with the reactivity oscillation method. However, difficult flux-overlap problems are involved here as well. Only thin foils are used as irradiation samples.

In the second chapter the choice and the design of the graphite ball detector are elucidated. The principle of the system is the transmission of a neutron beam, with a properly filtered neutron spectrum through a disk-shaped target. The neutrons are detected by  $\text{BF}_3$  detector tubes. The detector is insensitive to changes in the neutron scattering properties of the sample by means of a  $4\pi$  mounting of the 20  $\text{BF}_3$  tubes around the sample. A hollow graphite ball around the sample thermalizes partially the fast neutrons and thus increases the detector efficiency. The graphite

also disperses the neutrons spatially. A sample oscillator makes possible a periodical comparison with a permanent reference sample. In this way the influence of fluctuating circumstances is reduced to a minimum.

The third chapter discusses the experimental equipment and its most important properties. Some improvements have been made to achieve a maximum signal/background ratio.

The corrections to be applied for a correct interpretation of the measurements are dealt with.

Chapter 4 describes the computing programs applied. The programs MCLAAG, TREFKANS and MCBUIS have been specially designed to calculate the energy dependent detector efficiency.

The ATHENE reactor core spectrum has been computed by the program FAST ZOOM DELFT, the results of which have been compared with proton recoil measurements and a series of  $B_4C$  sample measurements with the graphite ball detector. The calculations of the filtered neutron spectra have been carried out with the MCREVERSE program. This program utilizes a specially designed novel technique, indicated as "backward Monte Carlo" calculation. Its discussion is to be found in the Appendix. Although this technique has a different approach, it turns out to equal the Monte Carlo solution of the adjoint neutron transport equation.

The program MCTRANS is designed to calculate the disk-shaped sample properties.

Finally, chapter 5 shows the results of a series of  $UO_2$  and  $ThO_2$  sample measurements with the graphite ball detector followed by an error discussion. The agreement between measurement and calculation for  $UO_2$  is almost completely within the error limits. The Doppler calculations for the thinnest  $UO_2$  samples in the fast neutron spectra and all  $ThO_2$  Doppler calculations by the RICM program underpredict the Doppler effect.

The error margins of the series of measurements performed, especially in the fastest spectrum, were much larger than may be indicated as characteristic of this measurement method, in consequence of the very limited reactor power (4 kW) and a forced measurement time schedule. The error margin in the integral neutron absorption of the  $\text{UO}_2$  samples, which in this case was between 4 and 29% (relative), can certainly be reduced to the range 2 to 11%. The error margin in the Doppler effect of the  $\text{UO}_2$  samples, which was now between 14 and 45% can certainly be reduced to the range 10 to 13%.

With these lower error margins the accuracy of the measurements is of the same order as, for example, the Doppler measurements by means of the activation analysis technique, while the interpretation of the measurements may be called relatively simple and reliable.

## SAMENVATTING

De opzet voor het werk dat in dit proefschrift wordt beschreven is het ontwerpen en testen van een meetmethode voor het nucleaire Dopplereffekt in intermediaire en snelle neutronenspektra.

De experimenten zijn uitgevoerd bij de ATHENE reaktor van de Technische Hogeschool te Eindhoven.

Twee uitgangspunten zijn gebruikt bij het ontwerp van de meetmethode:

- het systeem moet goedkoop en flexibel zijn;
- in het detektiesysteem mogen slechts eenvoudige geometrieën en neutronenfysisch goed bekende materialen worden toegepast, opdat de interpretatie van de signalen voldoende betrouwbaar is, zelfs indien dit uitsluitend met behulp van berekeningen moet gebeuren.

Van de reeds eerder toegepaste meetmethodes is de reactiviteits-oscillatiemethode de meest gevoelige. De interpretatie van de signalen levert evenwel grote problemen, zodat de onzekerheid in de resultaten in de orde van tientallen procenten ligt.

Een tweede methode is de aktiveringsanalyse van bestraalde Doppler monsters. De meetnauwkeurigheid ligt in de orde van 10%. De interpretatie van de resultaten is eenvoudiger dan bij de reactiviteits-oscillatiemethode, alhoewel fluxoverlappingsproblemen ook hier een rol spelen. Metingen worden steeds verricht aan zeer dunne monsters.

In het tweede hoofdstuk wordt de keuze en het ontwerp van de grafietbol detektor toegelicht. Het principe berust op de transmissie van een neutronenbundel, met een zorgvuldig gefilterd spectrum, door een schijfvormig monster. Detektie van de neutronen vindt plaats door middel van  $\text{BF}_3$  detektoren. De grafietbol detektor is ongevoelig voor verandering in de verstrooiingseigenschappen van een monster door een  $4\pi$  opstelling van de 20  $\text{BF}_3$  buizen rondom het monster. Een holle grafietbol tussen het monster en de  $\text{BF}_3$  buizen zorgt voor gedeeltelijke thermalisering van de snelle neutronen en verhoogt aldus de detektorefficiency. Tevens zorgt het grafiet voor

een ruimtelijke verspreiding van de neutronen. Een monstrososcillator maakt een periodieke vergelijking met een referentiemonster mogelijk. De invloed van fluktuerende omstandigheden wordt hierdoor tot een minimum beperkt.

In het derde hoofdstuk wordt een bespreking gegeven van de experimentele opstelling en de belangrijkste eigenschappen daarvan. Voor een maximale signaal/achtergrondverhouding zijn enkele verbeteringen aangebracht. De correctiefactoren die nodig zijn voor een korrekte interpretatie van de signalen worden behandeld.

Het vierde hoofdstuk geeft een beschrijving van de gebruikte rekenprogramma's. De programma's MCLAAG, TREFKANS en MCBUIS zijn speciaal ontworpen om de energie-afhankelijke detektorefficiency te berekenen.

Het ATHENE reaktor spektrum is berekend met behulp van het programma FAST ZOOM DELFT. De resultaten hiervan worden vergeleken met proton recoil metingen en een serie metingen aan  $B_4C$  monsters met behulp van de grafiëbol detektor. De berekening van de gefilterde neutronenspektra is uitgevoerd met het programma MCREVERSE. Dit programma maakt gebruik van een nieuw ontworpen rekentechniek, aangeduid met de naam "achterwaartse Monte Carlo" berekening. De argumentering van deze nieuwe techniek wordt gegeven in het Appendix. Alhoewel anders benaderd, blijkt deze techniek geheel overeen te stemmen met de Monte Carlo oplossing van de geadjungeerde neutronen transportvergelijking.

Het programma MCTRANS is ontworpen om de schijfvormige monsters te kunnen doorrekenen.

Hoofdstuk 5, tenslotte, geeft de resultaten van een serie  $UO_2$  en  $ThO_2$  metingen met de grafiëbol detektor, gevolgd door een foutendiskussie. De overeenstemming tussen metingen en berekeningen voor  $UO_2$  ligt voor bijna alle waarnemingen binnen de foutenmarge. De Doppler berekeningen voor de dunste  $UO_2$  monsters in de harde

neutronenspektra en alle  $\text{ThO}_2$  Doppler berekeningen door het programma RICM voorspellen een te gering Doppler effect. Door het zeer beperkte reaktorvermogen (4 kW) van de ATHENE reaktor enerzijds en door een geforceerd tijdschema voor de metingen anderzijds zijn de foutenmarges van de uitgevoerde metingen, vooral bij het hardste neutronenspektrum, veel groter uitgevallen dan als karakteristiek voor deze meetmethode beschouwd mag worden. De foutenmarge in de integrale neutronenabsorptie van de  $\text{UO}_2$  monsters, die nu lag tussen 4 en 29% (relatief), kan stellig worden teruggebracht tot het gebied tussen 2 en 11%. De foutenmarge in het Doppler effect van de  $\text{UO}_2$  monsters, die nu tussen 14 en 45% lag, kan zeker worden teruggebracht tot de grenzen 10 en 13%.

Met deze lagere foutenmarges komt de meetnauwkeurigheid in dezelfde orde te liggen als bijvoorbeeld het geval is bij de Doppler metingen door middel van aktiveringsanalyse, terwijl de interpretatie van de metingen relatief eenvoudig en betrouwbaar genoemd kan worden.

## ACKNOWLEDGEMENTS

In the design of the experiments and the performance of the measurements I have had much support from Mr. M. van Hout, with whom I always found a willing ear and lots of common sense at the right moment. I am very grateful to Messrs. H. Theelen, K. Koekkoek, W. van der Ven and H. van der Looy for a great deal of skillful mechanical and electronic assistance and for the many nightly hours spent on the Doppop. I am also very obliged to Mr. G. Vayssier, without whose mathematical penetration the happy ending of the "backward Monte Carlo" adventure would, to say the least, have been doubtful.

I thank Mr. M. Sluiter for his assistance and technical advice in many computing and programming problems.

I feel obliged to the whole ATHENE crew, under the inspiring command of Mr. A. Brouwers, who always guarded the right atmosphere even in very difficult situations.

Furthermore, I acknowledge Mr. F. de Kruijf for his contribution to the calculations, and finally I feel indebted to Linda Dornseiffer for the many hours devoted to the typing of this book.

## S T E L L I N G E N

1. Uit het feit dat bij de in de literatuur voorkomende Doppler experimenten met behulp van aktiveringsanalyse uitsluitend folies of althans zeer dunne monsters worden bestudeerd mag niet worden gekonkludeerd dat hieruit ook alle relevante informatie over het nucleaire Doppler-effekt kan worden verkregen.
2. De toepassing van neutronen absorberende konstruktie-materialen op welke plaats dan ook in een  $\text{BF}_3$  neutronendetektor heeft een nadelige invloed op de kwaliteit van de detektor en dient door de fabrikant expliciet te worden vermeld.
3. De invloed van spleten en gaten op de neutronenhuishouding in een verstrooiend medium is aanzienlijk groter dan verwacht zou kunnen worden op grond van oppervlak of volume hiervan.
4. Voor de bepaling van integrale absorptie werkzame doorsneden van splijttingsprodukten in snelle reaktoren bestaat minstens één methode die veel goedkoper is dan de bouw van een compleet kritisch reaktorensemble.
5. Een "backtron", hetgeen beschouwd kan worden als de fysische interpretatie van een geadjungeerd neutron, is het deeltje met de eigenschap dat het de mogelijke voorgeschiedenissen van een waargenomen neutron op de juiste wijze beschrijft. De kansdichtheid voor de overgang van een backtron van fasepunt B naar fasepunt A in de plaats-energie ruimte is gelijk aan de kansdichtheid voor de tegenovergestelde overgang van een neutron.
6. Het verdient aanbeveling om de overeenkomst tussen de toepassing van de regel van Bayes op de neutronentransportvergelijking en het adjungeren daarvan aan een nader onderzoek te onderwerpen.

7. Om op uitsluitend economische gronden te kunnen beoordelen of de invoering op grote schaal van een nieuw energiesysteem wenselijk is of niet, dient bij de schatting van de energieprijs die bij dit systeem behoort deze prijs reeds verwerkt te zijn in de investeringskosten.  
Verscheidene auteurs gaan hieraan lichtvaardig voorbij.

Ir. P. van Staveren, "Windkrachtcentrales op de Noordzee",  
Rapport van de Werkgroep Windenergie van de IRO, 1974.

8. Bij ruime beschikbaarheid van gratis komputertijd is het minimaliseren van de duur van de rekenprogramma's ongewenst.
9. De vroegtijdige beëindiging van het bedrijf van de ATHENE reaktor van de Technische Hogeschool Eindhoven is financieel en wetenschappelijk gezien betreurenswaardig.
10. Science fiction lektuur heeft voor toekomstdenkers de meeste waarde, wanneer het naast fiktieve science vooral ook de invloed van deze fictie op de mensen analyseert.
11. Artikel 67 van het wedstrijdreglement van de International Yacht Racing Union kan worden beschouwd als een ondermijning van de verantwoordelijkheid van de schipper en heeft ook zeker geen positieve invloed op de sportieve sfeer die een zeilwedstrijd behoort te hebben.
12. Het door stoplichten beveiligde stedelijke fietsverkeer is op veel plaatsen zodanig overgeregeld dat het maatschappelijke ongedisciplineerdheid in de hand werkt.